New Constraints on Fault-Zone Structure from Seismic Guided Waves

Jiedi Wu

Dissertation submitted to the faculty of the Virginia Polytechnic Institute and State University in partial fulfillment of the requirements for the degree of

Doctor of Philosophy
in
Geosciences

Committee
John A. Hole, Chair
J. Arthur Snoke
Ying Zhou
Martin C. Chapman
James A. Spotila

September, 1st, 2008
Blacksburg, Virginia

Keywords: fault zones, guided waves, low-velocity zone, wave propagation, finite difference, velocity structure, dispersion curve, earthquakes, and refraction.

New Constraints on Fault Zone Structure from Seismic Guided Waves

Jiedi Wu

ABSTRACT

The structure of fault zones (FZs) plays an important role in understanding fault mechanics, earthquake rupture and seismic hazards. Fault zone seismic guided waves (GW) carry important information about internal structure of the low-velocity fault damage zone. Numerical modeling of observed FZGWs has been used to construct models of FZ structure. However, the depth extent of the waveguide and the uniqueness of deep structure in the models have been debated. Elastic finite-difference synthetic seismograms were generated for FZ models that include an increase in seismic velocity with depth both inside and outside the FZ. Strong GWs were created from sources both in and out of the waveguide, in contrast with previous homogenous-FZ studies that required an in-fault source to create GW. This is because the frequency-dependent trapping efficiency of the waveguide changes with depth. The near-surface fault structure efficiently guides waves at lower frequencies than the deeper fault. Fault structure at seismogenic depth requires the analysis of data at higher frequencies than the GWs that dominate at the surface. Adapting a two-station technique from surface wave studies, dispersive differential group arrival times between two earthquakes can be used to solve for FZ structures between the earthquakes. This method was tested with synthetic data and shallow events recorded in the SAFOD borehole in the San Andreas Fault. A pair of deep earthquakes recorded in the SAFOD borehole indicate a ~150 m wide San Andreas Fault waveguide with >20% velocity contrast at 10-12 km depth. With additional earthquakes, the full FZ structure at seismogenic depth could be imaged. Subsurface FZ structure can also be derived from a surface source and receiver array analogous to a body-wave refraction survey. Synthetic seismograms for such source-receiver geometry were generated and verified that FZGWs are refracted by the increase in velocity with depth. Synthetic data from a surface array were successfully inverted to derive FZ structure in the subsurface. The new methods presented in this dissertation extend the potential of FZGWs to image deeper FZ structure than has been uniquely constrained in the past.

ACKNOWLEDGEMENTS

First I would like to thank my advisor, Dr. John Hole, who led me into such an interesting field of guided waves for my Ph.D. study. Dr. Hole was very helpful sharing his knowledge and ideas with me. His high standards in science benefited me with great skills in researching, writing, and presenting. Dr. Hole is also a good friend. Working with him has a lot of fun. I would also like to thank Dr. Arthur Snoke, a great teacher, who helped me learn the basis of the guided waves. He and Dr. Hole both contributed so much to my thesis work with many significant comments. My other committee members, Dr. James Spotila, Dr. Martin Chapman and Dr. Ying Zhou, provided additional support about their respective fields. Special thanks to Dr. Matthias Imhof, who left the university to Houston. Without his sharing of the finite-difference codes, I couldn't even have started my project. Dr. Imhof also gave me many constructive suggestions, which were very important for my research.

I would also like to thank Dr. John K. Costain. Although he might not know me, I was partially supported by his Graduate Geophysical Scholarship for my research. Special thanks to the Advanced Research Computing (ARC) at Virginia Tech. All of the numerical computing was done there.

Many thanks to my colleagues and friends in the department, those who already left or will be here for a while. Thank you Connie! I am gonna miss you. I also want to thank my parents for their love, understanding, and support for such a long time. Thank my sister, who takes care of my parents while I am out of my country. Finally, I must thank my husband (Hongbo Bi), who were always there supporting me without any complains. Living in two different cities is difficult for us. Without his continuous love and support, this dissertation would not have been possible.

ATTRIBUTIONS

The content and scope of this dissertation was prepared by J. Wu, and was edited and critiqued by my doctoral committee: Dr. John A. Hole (Chair), Dr. J. Arthur Snoke, Dr. Ying Zhou, Dr Martin C. Chapman and Dr. James A. Spotila. Each of the committee members is a faulty of Department of Geosciences, Virginia Tech. Funding was secured by the Department of Geosciences, Virginia Tech.

Chapter one was published on *Geophysical Journal International* 'Wu, J., Hole, J. A., Snoke, J. A. & Imhof, M. G., 2008; Depth extent of the fault-zone seismic waveguide: effects of increasing velocity with depth'. All authors contributed to this work. M. G. Imhof developed elastic three-dimensional finite-difference program. J. Wu tested the program, generated synthetic seismograms, analyzed the seismograms and wrote the manuscript. J. A. Hole predicted the existence of guided waves from off-fault seismic source, provided scientific support and critique and made subsidiary contributions to the writing. J. A. Snoke provided programs to measure dispersion curve from seismogram and edited the paper. J. Wu and J. A. Snoke developed the algorithms of calculating analytic dispersion curve.

Chapter two will be submitted to *Geophysical Journal International* 'Wu, J., Hole, J. A., & Snoke, J. A., 2008; Structure of the San Andreas Fault zone at depth from differential dispersion of seismic guided waves'. J. Wu prepared the synthetic seismograms, downloaded earthquake data recorded in SAFOD borehole, analyzed the data, created figures and tables. J. A. Hole developed the hypothesis to be tested. Manuscript was written by J. Wu with great contributions by J. A. Hole. J. A. Snoke provided scientific support and edited the paper.

Chapter three will be submitted to *Bulletin of the Seismological Society of America* 'Wu, J., Hole, J. A., 2008; Refraction of fault-zone guided seismic waves'. J. A. Hole designed the seismic survey to be tested. J. Wu prepared the synthetic seismograms, analyzed the seismograms and created figures under instructions of J. A. Hole. Writing was done by J. Wu and edited by J. A. Hole.

TABLE OF CONTENTS

LIST OF FIGURES

Chapter 1

Chapter 2

Chapter 3

LIST OF TABLES

Chapter 1

Depth Extent of the Fault-Zone Seismic Waveguide: Effects of Increasing Velocity with Depth *

Summary

The damage zone of a major fault can act as a low-velocity seismic waveguide. The fault-zone guided waves provide a potential method to constrain the *in situ* physical properties of the fault zone at depth. Recently, there has been debate over the depth extent of observed fault waveguides and whether fault properties at seismogenic depth can be constrained by guided waves. To address these questions, elastic finite-difference synthetic seismograms were generated for fault-zone models that include an increase in seismic velocity with depth both inside and outside the fault zone. Previous synthetic studies for a homogeneous fault showed that earthquakes off of the fault do not generate guided waves unless the waveguide is restricted to a few kilometres depth. In contrast, earthquakes both inside and outside of a depth-varying fault waveguide generate strong guided waves within the near-surface portion of the fault zone. This is because the frequency-dependent trapping efficiency of the waveguide changes with depth. The near-surface fault structure efficiently guides waves at lower frequencies than the deeper fault zone. The low frequency waves that are guided at the surface are not efficiently guided at greater depth and therefore travel as body waves. Fault structure at seismogenic depth requires the analysis of data at higher frequencies than the guided waves that dominate at the surface and have been the subject of most previous investigations.

Keywords: fault zones, guided waves, low-velocity zone, wave propagation, finite-difference.

*Published on *Geophysical Journal International*. Wu, J., Hole, J. A., Snoke, J. A. & Imhof, M. G., 2008. Depth extent of the fault-zone seismic waveguide: effects of increasing velocity with depth. Geophys. J. Int., 173, 611-622.

1.1 Introduction

Major fault zones accommodating plate motion form a deformation zone with low seismic velocities, which extends tens of meters to a few hundred meters wide (Healy & Peake 1975; Li & Leary 1990; Ben-Zion & Aki 1990; Li *et al.* 1994; Ben-Zion 1998; Ben-Zion & Sammis 2003). The low velocity zone (LVZ) is caused by fault gouge, fracturing, remineralization, and pore-fluid saturation. The LVZ acts as a waveguide, allowing the creation of fault zone trapped or guided waves (FZGW). FZGW are characterized by relatively high-amplitude, dispersive energy arriving later than the shear body waves. Seismic arrays across the fault provide a good way to identify FZGW because guided waves (GWs) are observed in and very close to the fault zone (FZ) but not at stations far from the FZ.

Several studies have suggested that the FZ waveguide extends to seismogenic depths of >10 km (Li *et al.* 1997; 2000; 2004; Li & Vernon 2001; Korneev *et al.* 2003; Mizuno *et al.* 2004; Mizuno & Nishigami 2006). Based on both earthquake- and explosion-generated FZGW, Li and co-workers have used a systematic model-parameter searching procedure with three-dimensional (3-D) finite-difference (FD) simulation to obtain depth-dependent FZ structures (Li *et al.* 1997; 2000; 2003; 2004; Li & Vernon 2001). Their results indicate, for example, that the San Andreas Fault at Parkfield acts as a ~150-m wide waveguide extending to at least 5-km depth with shear velocity reduced by 30-40% from the host rock velocities (Li *et al.* 2004). Such constraints on FZ structure can help to understand earthquake mechanisms at seismically active FZs.

Both 2-D and 3-D numerical studies have been carried out to investigate the GW trapping efficiency in terms of fault width, velocity contrast, source location, source-receiver distance and changes of fault geometry (Li & Vidale 1996; Igel *et al.* 1997; 2002; Ben-Zion 1998; Jahnke *et al.* 2002; Fohrmann *et al.* 2004). Moderate variation of FZ properties does not prevent GWs from propagating along the fault, but significant discontinuities do, such as an offset larger than the width of the waveguide (Igel *et al.* 2002; Jahnke *et al.* 2002; Fohrmann *et al.* 2004). GWs can only be generated from sources within or very close to a continuous fault (Li & Vidale 1996; Igel *et al.* 2002; Jahnke *et al.* 2002;

Fohrmann *et al.* 2004). However, a shallow FZ is capable of trapping seismic energy from sources that are far away from the fault as long as the source is located in a broad wedge below the bottom or beyond the edge of the waveguide (Igel *et al.* 2002; Jahnke *et al.* 2002; Fohrmann *et al.* 2004).

Recently, observations from earthquakes in the rupture zone of the 1992 Landers earthquake revealed that a large number of earthquakes far from the fault generated significant GWs (Peng *et al.* 2003). In addition, the time difference between the S-wave and GW did not grow with increasing source-receiver distance. These observations were cited as evidence that the waveguide at Landers extends continuously to no greater than 2-4 km depth. This is in direct contrast with earlier work that indicated a waveguide to seismogenic depth (Li *et al.* 2000). Using similar observations of GWs generated by earthquakes off the fault and a constant delay time for increasing distance, Lewis et al. (2005) concluded that the San Jacinto fault waveguide extends to only 3-5 km depth, in contrast with the deep San Jacinto waveguide of Li and Vernon (2001). Similar observations were used to indicate a shallow waveguide in Turkey (Ben-Zion *et al.* 2003) and Italy (Rovelli *et al.* 2002).

However, to show that GWs cannot be generated from sources off a deep fault, previous synthetic studies used a homogenous FZ with properties that were constant with depth (Li & Vidale 1996; Igel *et al.* 2002; Jahnke *et al.* 2002; Fohrmann *et al.* 2004). In reality, the pressure-induced closing of pores and fractures causes the seismic velocity of the crust, including FZs, to increase with depth. We use a 3-D finite-difference algorithm to generate synthetic seismograms for a more realistic model that contains an increase in velocity with depth. We investigate the effects of this velocity variation and the source location on generating trapped waves. The goal is to provide better constraints on the depth extent of the waveguide.

1.2 Method and Model

The synthetic 3-D velocity model (Figure 1.1, Table 1.1) consists of a linear velocity gradient with depth. A 200-m wide vertical FZ with reduced velocity is embedded in the model. The P and S-wave velocities are modified from the results of Li *et al*., (2004)

for the San Andreas Fault at Parkfield. Density is assumed to be linearly related to the P-wave velocity (Gardner *et al.* 1974). Two fault models were tested, one with the fault waveguide extending to the base of the model and the other with the waveguide extending to only 3 km depth.

A seismic source was placed at 6-km depth within the fault (Figure 1.1), but slightly off center to avoid destructive interference due to symmetry. A second source was placed 800 meters outside of the fault (Figure 1.1). Both sources have a strike-slip dislocation mechanism with $M_{xy} = M_{yx} = M_0$ as the non-zero moment tensor components. Therefore, the predominant GWs being generated at receivers above the source have particle motion in the fault-parallel direction (y-component, out of the plane of Figure 1.1), and only y-component synthetic seismograms will be discussed. A line of receivers is arranged perpendicular to the fault at the surface (Figure 1.1) with spacing of 40 m to simulate the arrays usually used to study FZGW. Additional receiver lines (Figure 1.1) are arranged parallel to the fault along the direction of wave propagation with spacing of 80 m and across the fault at 4-km depth at 40-m spacing. Such subsurface receiver arrays are unrealistic but will provide physical insights.

Synthetic seismograms were computed using a 3-D elastic finite-difference algorithm (Kelly *et al.* 1976) and the parameters in Table 1.1. An absorbing boundary condition (the Perfect Matched Layer of Chew & Liu 1996) was used to reduce reflections from the model surfaces. The source wavelet (Figure 1.1d) is band-limited from 0 to 15 Hz to avoid numerical aliasing.

1.3 Dispersion of Guided Waves

FZGWs are strongly dispersive. High-frequency waves with wavelengths much shorter than the fault width can be trapped by post-critical reflection or refraction at the boundaries of the relatively thick low-velocity layer. Waves with low frequencies are not guided if the FZ is much thinner than the wavelengths. Waves with intermediate frequencies and wavelengths similar to the fault width are more complexly trapped and travel at intermediate velocities. Waves at lower frequencies thus travel faster than at higher

frequencies. The phase velocity, c, of S-waves with fault-parallel particle motion for a homogeneous low-velocity FZ layer embedded in half spaces (HS) can be derived from (Ben-Zion & Aki 1990):

$$\tan[W 2\pi f(\beta_{FZ}^{-2} - c^{-2})^{1/2}] = \frac{2\mu_{FZ}(\beta_{FZ}^{-2} - c^{-2})^{1/2}\,\mu_{HS}(c^{-2} - \beta_{HS}^{-2})^{1/2}}{\mu_{FZ}^{2}(\beta_{FZ}^{-2} - c^{-2}) - \mu_{HS}^{2}(c^{-2} - \beta_{HS}^{-2})}, \qquad (1.1)$$

where W is the FZ width, f is the frequency, μ is the shear modulus and β is the shear-wave velocity. This analytic formula can be solved numerically to compute the dispersion curve. GW phase velocities are between the fault S-wave velocity and the host-rock S-wave velocity. The group velocity, U, which is related to the propagation of wave energy, can be computed from the derivative of the phase velocity c with respect to wavenumber k:

$$U = c + k\frac{dc}{dk} \qquad (1.2)$$

(Ben-Menahem & Singh 1981). The group velocity is slightly slower than the corresponding phase velocity and has a local minimum that is slower than the fault's S-wave velocity. Seismic waves with frequencies near the minimum in group velocity arrive at the same time in the seismogram, producing a strong arrival called the Airy phase (Ben-Menahem & Singh 1981). After propagating some distance, the waves at these frequencies have spread temporally the least and become dominant in the seismogram. These dominant frequencies correspond to wavelengths close to the width of the fault.

Group-velocity dispersion of the synthetic GWs was computed using the method of Snoke & James (1997). This method uses the multiple filter technique of Dziewonski *et al*. (1969) with the instantaneous frequency and enhanced display-equalized filter of Nyman & Landisman (1977). The GWs were analysed from the seismic trace of an off-center receiver within the FZ. Narrow band-pass filtering was applied using a zero-phase Gaussian filter, and envelopes were computed. The maximum of the envelope indicates the group arrival time of the GW at the center frequency of the filter. The arrival time was picked automatically and errors were estimated from the points on the envelope that were 1 dB

below the maximum. The average group velocity for the entire path from source to receiver was computed by dividing the source-receiver distance by the group arrival time.

1.4 Homogeneous Fault

To test the finite-difference algorithm and subsequent data analysis procedures, tests were first performed for two different homogeneous fault models. These models are similar to Figure 1.1a, but each consists of a constant-velocity fault in a homogenous host rock. One model used the slow surface velocities of Figure 1.1a, and the second model used the fast velocities from 6-km depth (Figure 1.1a, Table 1.1). Synthetic seismograms were recorded in an across-fault array at the surface.

Data in the fast homogeneous model from a source at 6-km depth in the fault are shown in Figure 1.2a. In addition to the direct S arrivals, there are later signals with amplitudes larger than the direct S waves. The amplitude of these signals rapidly decreases with distance from the fault, indicating FZGWs. This observation of high-amplitude ground shaking inside and low amplitude outside the FZ is used in real data to identify GWs. The finite-difference synthetic seismograms were consistent with synthetic seismograms generated using a wavenumber integration method (Herrmann 2002; Wang & Herrmann 1980). Figures 1.2b and 1.2c show the measured dispersion for the fast and slow homogeneous-fault data, calculated as described in the previous section. The contours indicate that the maximum amplitudes occur over a range of frequencies near the minimum in group velocity. The dispersion results show a good match between the synthetic data and the analytic solution of equations 1.1 and 1.2. The inhomogeneous fault model of Figure 1.1 is expected to create GWs with properties between those of the homogeneous-fault fast and slow end-member models.

Figure 1.2d shows the seismic profile for a source outside of the fast homogeneous fault. Consistent with previous studies (Li & Vidale 1996; Igel *et al.* 2002; Jahnke *et al.* 2002; Fohrmann *et al.* 2004), no GWs are observed.

1.5 Fault with Velocity that Increases with Depth

Y-component synthetic seismic sections for a surface array crossing the FZ models of Figure 1.1 are displayed in Figure 1.3. Figure 1.3a shows strong GWs for a source within the deep fault waveguide. Figure 1.3g shows strong GWs for the shallow fault waveguide for a source that is not on or directly below the fault. This confirms the results of previous workers (Igel *et al.* 2002; Jahnke *et al.* 2002; Fohrmann *et al.* 2004) that waves can enter a waveguide from below and become trapped. Figure 1.3d shows the results for a source that is outside of the deep fault waveguide. Previous studies showed that this geometry does not produce GWs for a homogeneous waveguide (Figure 1.2d) (Li & Vidale 1996; Igel *et al.* 2002; Jahnke *et al.* 2002; Fohrmann *et al.* 2004). However, Figure 1.3d shows clear GWs for the deep waveguide in which velocity increases with depth. Bandpass-filtered results show that the source in the waveguide produces GWs at a broad range of frequencies (Figures 1.3b, 1.3c). Sources off the fault produce GWs at relatively low frequency (Figures 1.3e, 1.3h) but minimal GWs at higher frequency (Figures 1.3f, 1.3i) for both shallow and deep waveguides.

Figure 1.4 shows an unrealistic across-fault array at a depth of 4 km. The source in the deep waveguide (Figures 1.4a-c) generates GWs at high frequency but not at low frequency as compared to the surface data. GWs are not observed for an off-fault source for either the deep or shallow waveguides (Figures 1.4d-i). The lower-frequency GWs that are observed at the surface for all three models (Figures 1.3b,e,h) are not generated below 4-km depth. This is obvious for the shallow waveguide, but not obvious for the waveguide that extends continuously to depth.

Figure 1.5 shows synthetic seismic sections for subsurface arrays that are parallel to the fault along the direction of wave propagation. Figures 1.5a and 1.5b are both from the deep waveguide model with the source in the fault. In Figure 1.5a, the receivers are located outside of the fault and only the S-wave appears. The non-linearly increase in arrival time with depth indicates the velocity variation with depth. Figure 1.5b is the profile with receivers located within the fault. GWs appear with large amplitude and later than the direct S-waves of Figure 1.5a. Direct S-waves are still visible, although the amplitudes are much

smaller than the GWs. Like the direct wave, the GW times increase non-linearly with depth due to the increase of velocity with depth.

The receiver array in the fault records different arrivals when the source is outside of the waveguide (Figures 1.5c, d). In Figure 1.5c, which has a shallow waveguide, only direct S-waves exist at depth. The curvature of the arrival times changes near 3-km depth at the bottom of the shallow waveguide. Significant wave energy enters the bottom of the fault and forms a GW, which dominates at shallower depth. Similarly, in Figure 1.5d which has a deep waveguide, GWs appear only at shallower depth. Figures 1.2d, 1.4d-f, and 1.5d all indicate that GWs cannot be generated in the portion of the fault that is adjacent to a source off the fault. However, the change in fault properties with depth allows waves from the source off the fault to enter the fault at shallower depth. The difference between Figures 1.5d and 1.5c is that the conversion from S-wave to GW in the continuous fault occurs gradually over a range of depth, rather than at a discrete discontinuity.

1.6 Dispersion in the Depth-Dependent Fault

The velocity model of Figure 1.1 varies slowly relative to the scale of the 200-m width of the FZ and the corresponding dominant trapped wavelengths. Thus it can be considered to be approximately homogeneous locally, and a theoretical dispersion curve can be calculated at each point in depth from Equations 1.1 and 1.2. The GW group velocity dispersion curves at each depth of the model of Figure 1.1a are shown in Figure 1.6a. Figure 1.6b re-plots the group velocity as a function of both depth and frequency. In these plots, the group velocity gradually increases with depth. At each depth, the group velocity first declines strongly with increasing frequency, then increases slightly. The minimum in group velocity indicates the high-amplitude Airy phase and the dominant trapped frequency (dash-dotted curves on Figure 1.6). The dominant frequency increases from ~3 Hz at the surface to ~12 Hz at 6-km depth, a change of two octaves.

The group velocity at different frequencies is plotted as a function of depth in Figure 1.6c. Low frequency waves (<4 Hz) travel at speeds close to the host-rock S-wave velocity below 3-km depth. A 4-Hz wave becomes an Airy phase with velocity less than the

fault's body-wave velocity only above 3-km depth. At 8-16 Hz, waves are optimally guided below 3-km depth but become body waves with the fault S-velocity at shallower depth.

The group velocity for the shallow waveguide model of Figure 1.1b is the same as Figure 1.6b from the surface to 3-km depth. Below 3-km depth, the velocity in the shallow waveguide model is the body-wave velocity, and is not dispersive.

Figure 1.6 explains the features of the GWs observed in the data of Figures 1.3-1.5. For the seismic source within the deep waveguide, seismograms recorded at the surface have GWs of both high (>10 Hz) and low (<6 Hz) frequencies (Figures 1.3a-c) because the waves have been trapped in both the deep and shallow parts of the fault. If the source is placed outside of a deep waveguide or below a shallow waveguide, waves cannot be trapped in the deep part of the fault (Figures 1.4d-i) and hence high-frequency GWs are not observed at the surface (Figures 1.3f, 1.3i).

Waves can enter the shallow waveguide from below, producing low-frequency FZGW at the surface (Figures 1.3g-h). The portion of the deep waveguide that is capable of trapping low frequencies is restricted to shallow depth, similar to the shallow waveguide. Hence low-frequency waves from the deep off-fault source can become trapped in the shallow part of the deep waveguide, generating low frequency GWs at the surface (Figures 1.3d-e). Figures 1.3-1.5 are similar to each other at low frequencies because the low-frequency portion of both the shallow and deep waveguides extends to similar shallow depths. For all cases, waves with frequencies <6 Hz travel mostly as body waves below ~3-km depth, even for the source within the deep waveguide (Figures 1.4b, 1.4e, 1.4h, 1.6c).

Figure 1.7 shows the group velocity as a function of frequency for the seismic traces highlighted in Figure 1.3, computed using the method described above. Unlike Figure 1.2, the total distance divided by the arrival time produces an average group velocity that is not indicative of any specific point in the fault. The group arrival time can be derived from the analytic local group velocity of Figure 1.6 by integration of the inverse of local velocity along the path from source to receiver. The analytic average group velocity derived from

the integrated local velocity is shown in Figure 1.7. The observed and analytic dispersion curves match well for the source in the deep waveguide (Figure 1.7a).

For the off-fault sources (Figures 1.7b,c), the path of the GW is not obvious. The integration was computed using an approximate path consisting of a straight line from the source to the fault at 3-km depth, then a vertical line to the surface. Two analytic group dispersion curves are displayed in Figures 1.7b and 1.7c. One is the same as that in Figure 1.7a for a deep fault (dashed lines). The other integrates local velocity below 3-km depth using the S body-wave velocity outside the fault (solid lines). The measured average group velocity for the source outside the deep and shallow waveguides matches the analytic velocity of the corresponding fault model (Figures 1.7b,c). The exception is above 5 Hz for the deep waveguide, where the measured velocity corresponds to the weaker third mode rather than the fundamental mode. For the shallow waveguide (Figure 1.7c), waves with frequency above ~7 Hz are delayed by the fault's body-wave velocity, but are weak and non-dispersive.

Amplitude spectra for the three models are displayed in Figure 1.7d. At frequencies <5 Hz, they are similar. At frequencies >7 Hz, the amplitude decays for the source off the deep fault and for the shallow fault. The maximum amplitude is at ~4 Hz for the shallow fault and the source off the deep fault, but at ~9 Hz for the source inside the deep fault. Significant high frequency GWs are missing for off-fault and below-fault sources.

Dispersion analysis was also performed for the data across the fault at 4-km depth (Figure 1.4). As expected, dispersion was observed at higher frequencies (>8 Hz) for the source in the deep waveguide. No dispersion was found for the off-fault and below-fault sources, indicating no GWs.

1.7 Deep versus Shallow Fault Waveguide

Recent studies have cited the observation of strong GWs from earthquakes off the fault as evidence that the fault waveguide cannot extend deeper than 2 to 5 km depth (Peng *et al*., 2003; Ben-Zion *et al*., 2003; Lewis *et al*., 2005). These conclusions were based on synthetic studies using a homogenous fault model. Figures 1.3-1.5 show that a more

realistic fault waveguide that increases in velocity with depth can produce strong GWs from earthquakes off the fault. This allows the existence of a deep fault waveguide for the faults in those studies.

To help understand the mechanism of generating the GWs from an off-fault source, Figure 1.8 shows the envelope of narrow-band-pass filtered seismograms from the along-fault array. Analytic travel times in Figure 1.8 are computed by integration through the local body-wave velocity of Figure 1.1 and GW group velocity of Figure 1.6. At 2 Hz, the trace envelopes are indistinguishable for the shallow and deep faults and for the on-fault and off-fault sources (Figures 1.8a, d, g). The time picks of the envelope match the analytic travel times. The 2-Hz GW gradually diverges from the body-wave travel-time curve between ~2.5 and ~1-km depth, consistent with Figure 1.6c. At 4 Hz in the deep-fault model (Figures 1.8b, e), the GW gradually emerges from the body wave between ~4.5 and ~3-km depth. These depths are above the source, allowing the off-fault source to generate GWs that look very similar to those for the source within the fault. The shallow fault is only subtly different at 4 Hz (Figure 1.8h), with GWs initiating more sharply at 3-km depth.

At 8 Hz, the GW is generated only for the source within the deep fault and initiates close to the source (Figure 1.8c). The 8-Hz wave can enter the shallow fault, but it travels at the fault's body-wave velocity and is not a dispersive GW (Figures 1.6, 1.7c, 1.8i). The analytic GW travel times and trace envelope differ at 8 Hz for the source off the deep fault (Figure 1.8f). The off-fault source does not create a fundamental-mode 8-Hz GW in the deep fault. Instead, a higher order mode is observed (Figure 1.7b).

At any given frequency, the continuous low-velocity FZ of Figure 1.1 acts as a waveguide only over a finite range of depth. If the source lies in a broad wedge beneath that depth range, such as the off-fault source for waves at <6 Hz, then body waves at that frequency can enter the waveguide and produce GWs. The S body wave is gradually converted into GWs over a transition zone in depth. This is different from the shallow fault, where conversion occurs at the discrete bottom of the fault. At low (<4 Hz) frequency, the shallow and deep FZs of Figure 1.1 are indistinguishable. At higher (>8 Hz) frequency, the source outside the FZ is adjacent to that frequency's waveguide and, analogous to the

homogeneous fault (Figure 1.2d), GWs are not produced.

Peng *et al*. (2003) estimated the time delay between the S-wave and the trapped wave group from earthquakes in the rupture zone of the 1992 Landers, California earthquake and found the delays did not grow systematically with increasing distance of the earthquake from the station. They concluded that the GW has an approximately constant propagation length in the FZ waveguide for different source distances, which indicated a shallow waveguide close to the station. Ben Zion et al. (2003) and Lewis et al. (2005) made similar observations and conclusions for the San Jacinto fault, California, and North Anatolian fault, Turkey.

GWs are highly dispersive; therefore the time delays between the non-dispersive S-wave and GW are frequency dependent. Mizuno et al. (2004) and Mizuno & Nishigami (2006) found that GW travel-time delays increase with frequency on the Mozumi-Sukenobu and Nojima faults in Japan.

For a fault with properties that vary with depth, the velocity contrast between the body wave and GW is both depth and frequency dependent. Figure 1.9a shows time delays as a function of frequency for the deep fault model for sources at different depths and a receiver at the surface. Analytic delay times (lines) are computed by integration of the local group velocity of Figure 1.6. Symbols indicate the measured group delay times for the data of Figure 1.3 (and Figures 1.10a, 1.10e), and for a source 1 km deeper than that in Figure 1.1, at 7 km depth (Figure 1.10b). The measured group delay times generally follow the appropriate analytic curves, but are noisy because picking the broad peak of the trace envelope is not precise. The source at 7-km depth has measured delays greater than those of the source at 6-km depth, but the scatter of data points is larger than the differences between the two depths. The measured data for the shallow fault follow the curve for a source at the bottom of the fault (3-km depth) even though the source is deeper. Figure 1.9b plots the time delays as a function of source-to-receiver distance, mimicking the plots used by previous workers. As observed in those studies, the time delay does not increase linearly. In addition, it is strongly dependent upon frequency.

The time delay for the deep-fault GW (solid lines) is compared in Figure 1.9b with that for a 3-km shallow fault (dashed lines) at different frequencies. At frequencies ≤2 Hz, the time delay increases only weakly with increasing source depth beyond 2-3 km. This is because the velocity of a 2 Hz FZ wave below a few kilometres depth is almost identical to the body wave (Figure 1.6). The 2 Hz time delays for the shallow and deep faults differ by less than 0.1 second. Error bars in the measured delay times in Figure 1.9b were derived from the errors in Figure 1.7, and indicate that the difference between the shallow and deep faults is not detectable at 2 Hz. Figure 1.10 shows the data from across-fault arrays for the deep and shallow fault models for sources at 6 and 7-km depth, filtered to <4 Hz. All five plots look very similar, and the GW for the deeper source in the deep fault is not delayed noticeably more than the shallower source or the shallow fault. At these frequencies, the data do not distinguish the deep fault from the shallow fault. These frequencies dominate the GW observed at the surface. Time delays are larger at higher frequency (Figure 1.9). The difference between shallow and deep fault delays grows and becomes detectable at ~4 Hz. Higher frequency waves are more sensitive to the deeper fault structure.

1.8 Discussion

Previous studies indicated that FZGW are generated only when the source is located within or very close to the FZ (Li & Vidale 1996; Igel *et al.* 2002; Jahnke *et al.* 2002). Alternatively, energy can enter the waveguide from the bottom of the fault or at a discontinuity in the fault (Igel *et al.* 2002; Jahnke *et al.* 2002; Fohrmann *et al.* 2004). These observations are true when the FZ is homogenous. However, pressure closes pores and fractures, which causes seismic velocity both outside and inside of faults to increase substantially with depth in the upper crust. Fault thickness may also change with depth (Rovelli *et al.* 2002). A waveguide will optimally trap waves with frequencies corresponding to wavelengths close to the FZ width. The corresponding dominant Airy phase frequency will increase with increasing velocity or with decreasing FZ thickness. Therefore, GWs with different dominant frequencies will be trapped at different depths.

In this study, a FZ model with velocity that increases with depth was used to generate synthetic seismograms. Unlike the homogeneous fault, GWs were produced for

both in-fault and off-fault sources. The GWs from the source off the deep fault had low frequency and travel time delays very similar to the shallow fault. These observations are due to the fact that low frequencies are not guided in the deeper waveguide. The wavelength at low frequency is sufficiently large that the waves act as body waves at depth even in the presence of the deep fault LVZ. These waves can then enter the waveguide and become guided at shallower depth. These low frequencies dominate the surface-based recordings because they are actively being guided close to the station and because they are less attenuated in the low-Q FZ.

Assuming fault-property variation along the plane of the fault is smooth relative to the thickness of the fault, the local fault structure can be used to compute a local dispersion curve. Group arrival time at each frequency can be integrated along the path that the energy travels to produce a group average-velocity dispersion curve. In this study, only the guided shear wave that is polarized parallel to the fault (Love-type wave) was modeled. A coupled P-SV phase (Rayleigh-like wave) can also be generated in FZ waveguides. It has similar velocity and dispersion properties and will therefore behave in a similar manner to the Love-type wave (Ben-Menahem & Singh 1981).

This study contradicts previous investigations that used a homogeneous-fault model to indicate that FZ waveguides are shallow (Peng *et al.* 2003; Fohrmann *et al.* 2004; Lewis *et al.* 2005). The synthetic data for a fault in which velocity increases with depth reproduce the observations of GWs for off-fault earthquakes, including travel time delays that do not increase with earthquake distance. A broad fault damage zone (brecciation, remineralization, and/or fracturing) may extend through the seismogenic zone for these faults. However, the results of this study agree with the previous studies that a *low-frequency* waveguide does not extend to depth. If a deeper FZ exists, it guides higher frequency waves. The seismic velocity of the upper crust typically increases substantially (by a factor of 1.5 to 3) in the upper 3-10 km of the crust, except where unweathered crystalline rocks are encountered at the surface. The higher fracture density in FZs will close faster with depth than that outside of FZs, and thus velocity will increase faster in FZs, reducing the velocity contrast. The data of previous workers (Peng *et al.* 2003; Fohrmann *et al.* 2004; Lewis *et al.* 2005) indicate that the low-frequency waveguide does not extend beyond 3-5 km depth. This

means that the low-velocity fault damage zone does not widen proportional to the velocity increase (e.g., by a factor of 2 or greater) to maintain a uniform fault-zone wavelength.

To constrain fault properties at seismogenic depths, trapped waves at higher frequency are needed. In the model of Figure 1.1, frequencies >4 Hz are required to constrain the waveguide below 3-km depth. The velocity model in Figure 1.1c is modified from a study on the San Andreas Fault at Parkfield (Li *et al.* 2004). However the fault was widened to 200 meters in order to save computational effort. Li *et al.* (2004) suggest that the waveguide at Parkfield narrows from 150 m at the surface to 100 m at depth. This thinner fault would produce GWs at higher frequencies than the fault of Figure 1.1. Waves with frequencies >8 Hz, and perhaps much greater, are required to measure fault-zone properties at seismogenic depths at Parkfield. Other faults may have different depth-varying velocity or thickness, and thus GW analysis at different frequencies would be required for those faults.

Some previous studies (Peng *et al.* 2003; Li *et al.* 2000; Mizuno *et al.* 2004; Mizuno & Nishigami 2006) have investigated the frequency-dependent properties (group velocity, travel time delay) of observed GWs. In the future, such information may provide unique constraints on fault-zone properties at seismogenic depths. One issue, however, is that the high attenuation observed in FZs, particularly near the surface, may make the recording of higher frequencies difficult or impossible. High-frequency data recorded in boreholes (Mizuno *et al.* 2004; Mizuno & Nishigami 2006; Li *et al.* 2006) can provide important contributions.

Acknowledgements

We thank Ying Zhou and Martin Chapman for constructive comments. Two anonymous reviews greatly improved the manuscript. Synthetic seismograms were computed using the Terascale Computing Facility at Virginia Tech. JW received partial support from the John K. Costain Graduate Scholarship.

References

Ben-Menahem, A. & Singh, S. J., 1981. Seismic Waves and Sources. Springer-Verlag New York Heidelberg Berlin,

Ben-Zion, Y. & Aki, K., 1990. Seismic Radiation from an Sh Line Source in a Laterally Heterogeneous Planar Fault Zone. Bulletin of the Seismological Society of America, 80, 971-994.

Ben-Zion, Y., 1998. Properties of seismic fault zone waves and their utility for imaging low-velocity structures. Journal of Geophysical Research-Solid Earth, 103, 12567-12585.

Ben-Zion, Y., Peng, Z. G., Okaya, D., Seeber, L., Armbruster, J. G., Ozer, N., Michael, A. J., Baris, S., Aktar, M., Kuwahara, Y. & Ito, H., 2003. A shallow fault-zone structure illuminated by trapped waves in the Karadere-Duzce branch of the North Anatolian Fault, western Turkey. Geophysical Journal International, 152, 699-717.

Ben-Zion, Y. & Sammis, C. G., 2003. Characterization of fault zones. Pure and Applied Geophysics, 160, 677-715.

Chew, W. C. & Liu, Q. H., 1996. Perfectly matched layers for elastodynamics: A new absorbing boundary condition. Journal of Computational Acoustics, 4, 341-359.

Dziewonski, A., Bloch, S. & Landisman, M., 1969. A technique for the analysis of Transient seismic signals. Bulletin of the Seismological Society of America, 59, 427-444.

Fohrmann, M., Igel, H., Jahnke, G. & Ben-Zion, Y., 2004. Guided waves from sources outside faults: An indication for shallow fault zone structure? Pure and Applied Geophysics, 161, 2125-2137.

Gardner, G. H. F., Gardner, L. W. & Gregory, A. R., 1974. Formation Velocity and Density - Diagnostic Basics for Stratigraphic Traps. Geophysics, 39, 770-780.

Healy, J. H. & Peake, L. G., 1975. Seismic Velocity Structure Along a Section of San Andreas Fault near Bear-Valley, California. Bulletin of the Seismological Society of America, 65, 1177-1197.

Herrmann, R. B., 2002. Computer programs in seismology, an overview of synthetic seismogram computation. Saint Louis University, http://www.eas.slu.edu/People/RBHerrmann/ComputerPrograms.html,

Igel, H., Ben-Zion, Y. & Leary, P. C., 1997. Simulation of SH- and P-SV-wave propagation in fault zones. Geophysical Journal International, 128, 533-546.

Igel, H., Jahnke, G. & Ben-Zion, Y., 2002. Numerical simulation of fault zone guided waves: Accuracy and 3-D effects. Pure and Applied Geophysics, 159, 2067-2083.

Jahnke, G., Igel, H. & Ben-Zion, Y., 2002. Three-dimensional calculations of fault-zone-guided waves in various irregular structures. Geophysical Journal International, 151, 416-426.

Kelly, K. R., Ward, R. W., Treitel, S. & Alford, R. M., 1976. Synthetic Seismograms - Finite-Difference Approach. Geophysics, 41, 2-27.

Korneev, V. A., Nadeau, R. M. & McEvilly, T. V., 2003. Seismological studies at Parkfield IX: Fault-zone imaging using guided wave attenuation. Bulletin of the Seismological Society of America, 93, 1415-1426.

Lewis, M. A., Peng, Z., Ben-Zion, Y. & Vernon, F. L., 2005. Shallow seismic trapping structure in the San Jacinto fault zone near Anza, California. Geophysical Journal International, 162, 867-881.

Li, Y. G. & Leary, P. C., 1990. Fault Zone Trapped Seismic-Waves. Bulletin of the Seismological Society of America, 80, 1245-1271.

Li, Y. G., Vidale, J. E., Aki, K., Marone, C. J. & Lee, W. H. K., 1994. Fine-Structure of the Landers Fault Zone - Segmentation and the Rupture Process. Science, 265, 367-370.

Li, Y. G. & Vidale, J. E., 1996. Low-velocity fault-zone guided waves: Numerical investigations of trapping efficiency. Bulletin of the Seismological Society of America, 86, 371-378.

Li, Y. G., Ellsworth, W. L., Thurber, C. H., Malin, P. E. & Aki, K., 1997. Fault-zone guided waves from explosions in the San Andreas fault at Parkfield and Cienega Valley, California. Bulletin of the Seismological Society of America, 87, 210-221.

Li, Y. G., Vidale, J. E., Aki, K. & Xu, F., 2000. Depth-dependent structure of the Landers fault zone from trapped waves generated by aftershocks. Journal of Geophysical Research-Solid Earth, 105, 6237-6254.

Li, Y. G. & Vernon, F. L., 2001. Characterization of the San Jacinto fault zone near Anza, California, by fault zone trapped waves. Journal of Geophysical Research-Solid Earth, 106, 30671-30688.

Li, Y. G., Vidale, J. E., Oglesby, D. D., Day, S. M. & Cochran, E., 2003. Multiple-fault rupture of the M7.1 Hector Mine, California, earthquake from fault zone trapped waves. Journal of Geophysical Research-Solid Earth, 108, L12S06, doi:10.1029/2003GL019044.

Li, Y. G., Vidale, J. E. & Cochran, E. S., 2004. Low-velocity damaged structure of the San Andreas Fault at Parkfield from fault zone trapped waves. Geophysical Research Letters, 31, 2165, doi:10.1029/2001JB001456.

Li, Y. G., Vidale, J. E. & Malin, P., 2006. Parkfield Fault-Zone Guided Waves:

High-Resolution Delineation of the Low-Velocity Damage Zone on the San Andreas at Depth near SAFOD Site. The Prcodeeding of ICDP-IODP Fault-Zone Drilling, pp 1-4.

Mizuno, T., Nishigami, K., Ito, H. & Kuwahara, Y., 2004. Deep structure of the Mozumi-Sukenobu fault, central Japan, estimated from the subsurface array observation of fault zone trapped waves. Geophysical Journal International, 159, 622-642.

Mizuno, T. & Nishigami, K., 2006. Deep structure of the Nojima Fault, southwest Japan, estimated from borehole observations of fault-zone trapped waves. Tectonophysics, 417, 231-247.

Nyman, D. C. & Landisman, M., 1977. Display-Equalized Filter for Frequency-Time Analysis. Bulletin of the Seismological Society of America, 67, 393-404.

Peng, Z. G., Ben-Zion, Y., Michael, A. J. & Zhu, L. P., 2003. Quantitative analysis of seismic fault zone waves in the rupture zone of the 1992 Landers, California, earthquake: evidence for a shallow trapping structure. Geophysical Journal International, 155, 1021-1041.

Rovelli, A., Caserta, A., Marra, F. & Ruggiero, V., 2002. Can seismic waves be trapped inside an inactive fault zone? The case study of Nocera Umbra, Central Italy. Bulletin of the Seismological Society of America, 92, 2217-2232.

Snoke, J. A. & James, D. E., 1997. Lithospheric structure of the Chaco and Parana Basins of South America from surface-wave inversion. Journal of Geophysical Research-Solid Earth, 102, 2939-2951.

Wang, C. Y. & Herrmann, R. B., 1980. A Numerical Study of P-Wave, Sv-Wave, and Sh-Wave Generation in a Plane Layered Medium. Bulletin of the Seismological Society of America, 70, 1015-1036.

Table 1.1: Parameters for 3-D finite-difference simulations

Model Size		1400 m × 2000 m × 7400 m	
Grid Spacing		8 m	
Time Step		0.5 ms	
Source Type		$M_{xy} = M_{yx} = M_0$	
Frequency filter		high cut starting at 15 Hz	
Fault Zone Width		200 m	
Parameters 0 - 6 km depth	P-wave Velocity (km/s)	S-wave Velocity (km/s)	Density (g/cm^3)
Host rock	2.4 - 6.1	1.0 - 2.8	2.54 - 2.74
Fault Zone	1.5 - 4.5	0.65 - 2.2	1.96 - 2.17

Figure 1.1: Three-dimensional seismic velocity model.

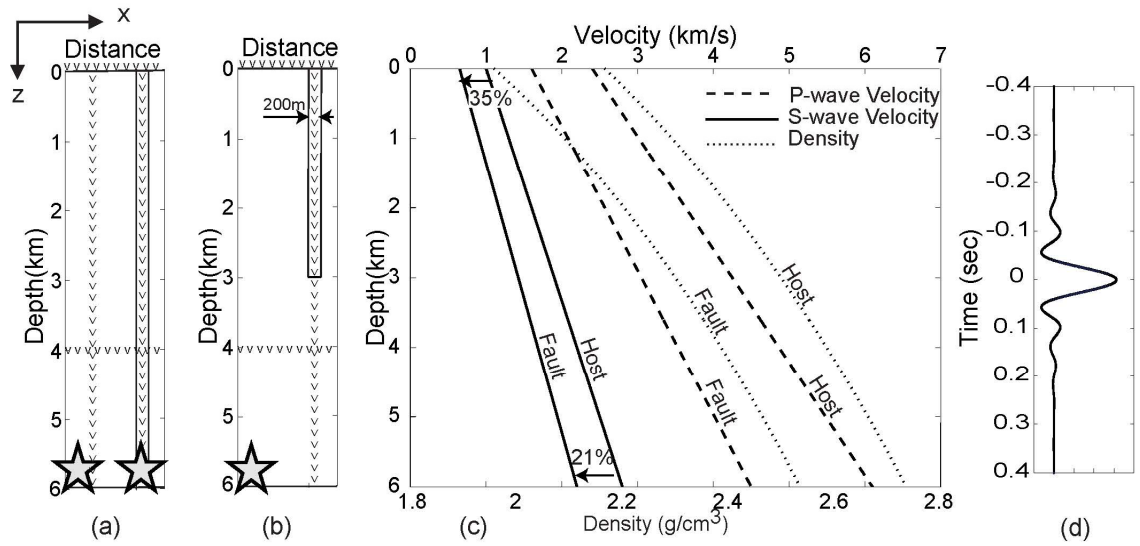

Three-dimensional seismic velocity models used to compute synthetic seismic data. (a) Vertical section across the deep fault model. The fault-zone waveguide is 200-m wide. The model extends uniformly in the out-of-plane (y) direction. V's denote receiver arrays. Receivers on horizontal arrays are spaced 40 m and receivers on vertical arrays are spaced 80 m. Stars are seismic sources. (b) Shallow waveguide model that is otherwise identical to (a). (c) One-dimensional P-wave velocity (dashed lines), S-wave velocity (solid lines), and density (dotted lines) profiles through the models' crust and fault. The S wave velocity of the fault is reduced from the host rock by 35% at the surface and 21% at 6-km depth. (d) Source wavelet used in the finite-difference synthetic calculation.

Figure 1.2: Seismic data and dispersion curves for a vertically homogenous fault.

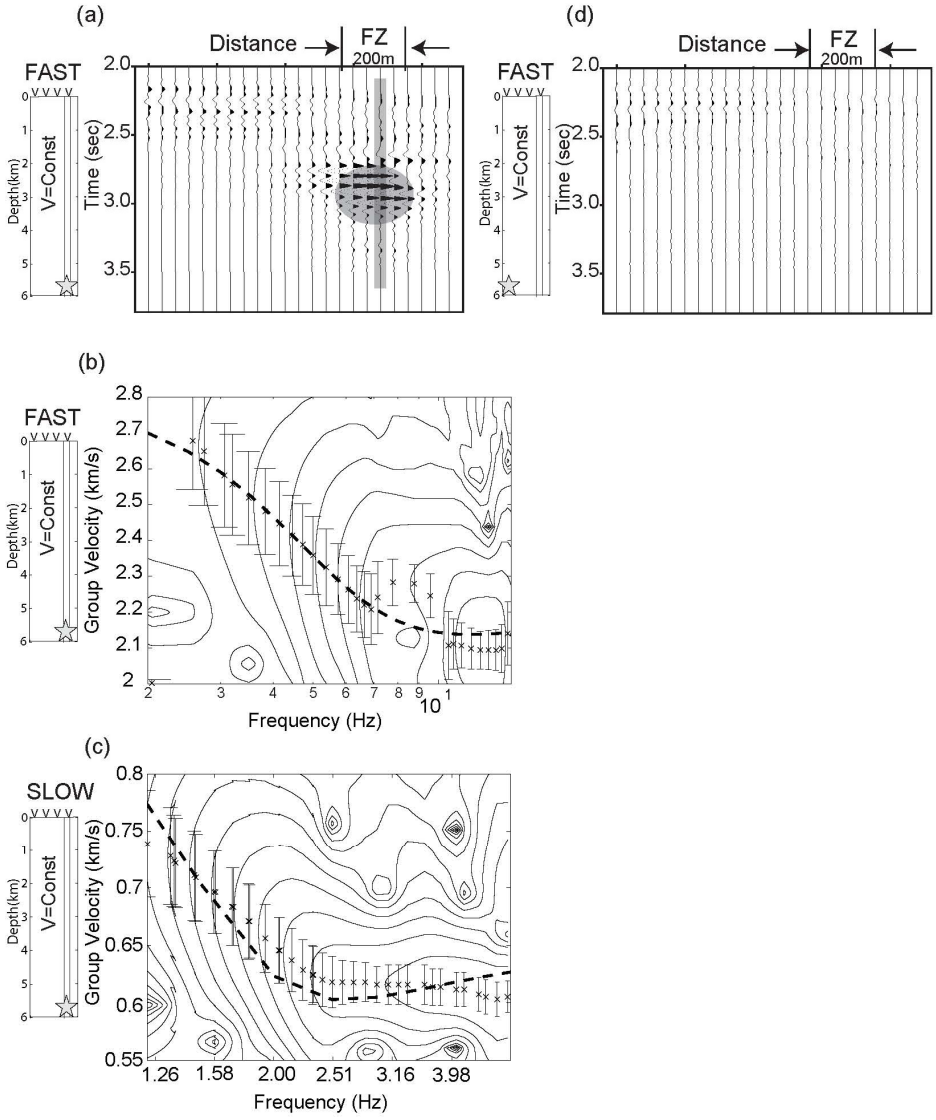

The small panels at left show the source and receiver geometry. (a) Fault-parallel (y component) seismograms for a 200-m wide homogeneous fault with an S-wave velocity of 2.2 km/s, surrounded by a constant 2.8 km/s crust. A strong guided wave (grey ellipse) is observed on receivers within but not outside of the fault zone. (b) Group velocity dispersion curve (symbols with error bars) for the trace window highlighted in grey in (a), derived using the method of Snoke & James (1997). Analytic dispersion (Equations 1.1 and 1.2) is shown as a dashed line. Contours represent the amplitude of the narrow-band trace envelope at each frequency. (c) Analytic and synthetic data dispersion for a 200-m wide

homogeneous fault with an S-wave velocity of 0.65 km/s, surrounded by a 1.0 km/s crust. The synthetic seismic profile is not shown here; it is similar to (a). Note that both the velocity and frequency scales of (b) and (c) are different. (d) Seismic profile for the same model as (a) but with the source outside of the waveguide. Guided waves are absent.

Figure 1.3: Across-fault seismic sections at the surface.

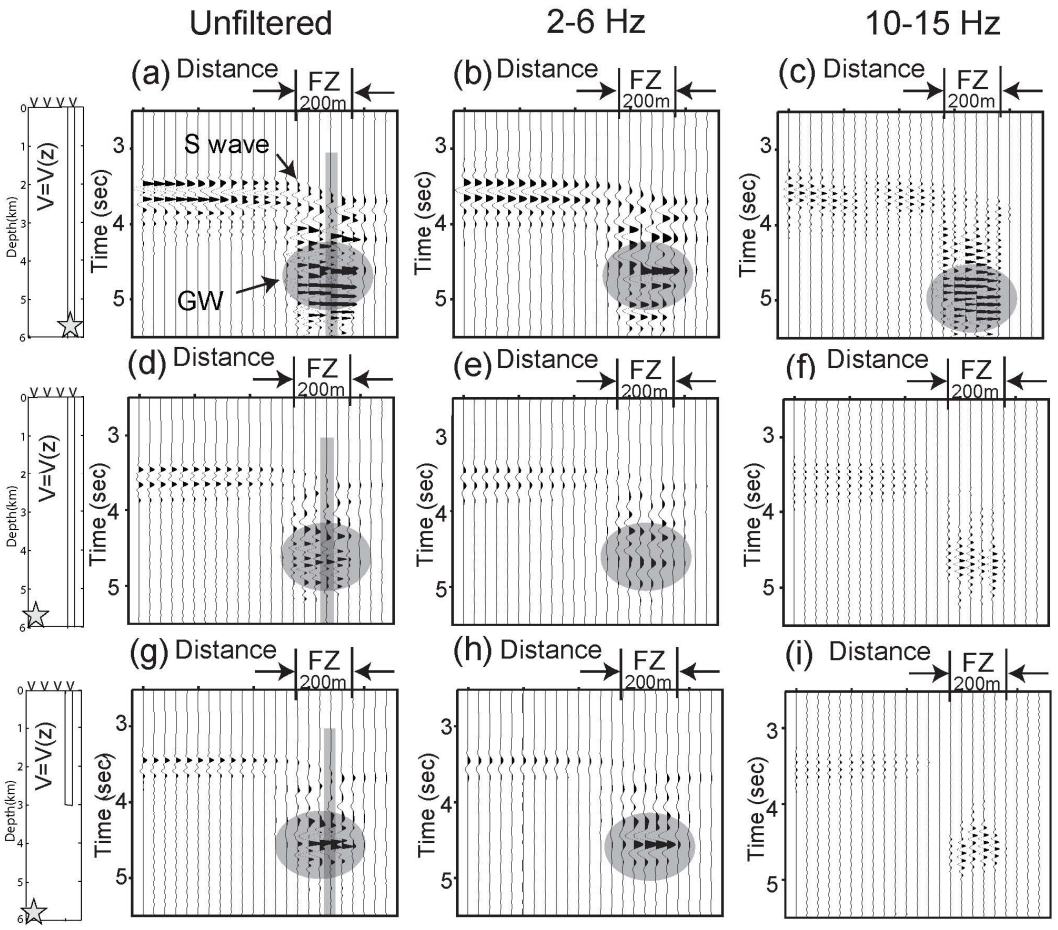

Across-fault seismic sections at the surface for the models of Figure 1.1. The left column indicates the fault geometry and positions of source and receivers for each row. The second through fourth columns show the unfiltered, low frequency bandpass (2-6 Hz), and high-frequency bandpass (10-15 Hz) filtered seismograms. All of the plots are scaled with the same absolute amplitudes. The off-fault source was a little too close to the left wall of the model volume, resulting in smaller body-wave amplitudes. Guided waves are highlighted with grey ellipses. The source in the deep fault creates guided waves over a broad frequency range. The off-fault source creates guided waves only at low frequency for both the deep and the shallow fault. The trace windows highlighted in grey in the unfiltered sections were used for the dispersion analysis of Figure 1.7.

Figure 1.4: Across-fault seismic sections at 4-km depth.

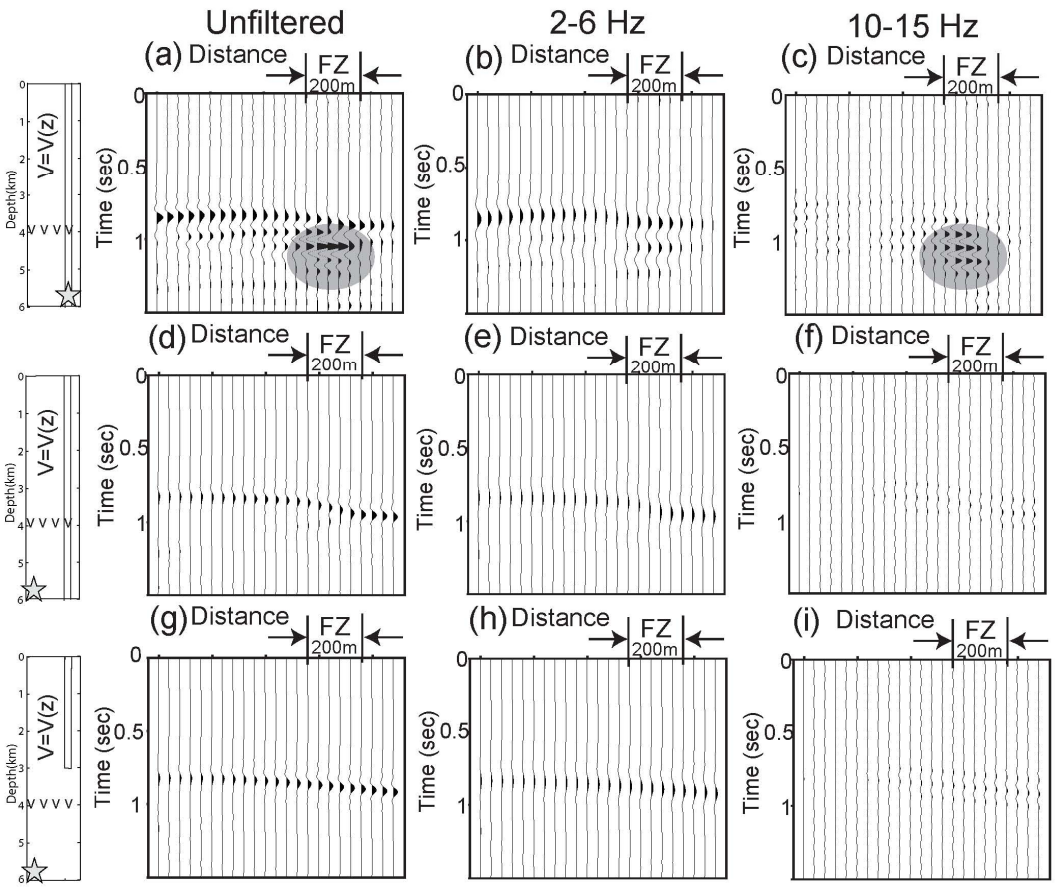

Same as Figure 1.3, but for across-fault seismic sections at 4-km depth. Only the source inside the fault creates guided waves, which are at higher frequency than those observed at the surface (Figure 1.3).

Figure 1.5: Fault-parallel seismic sections.

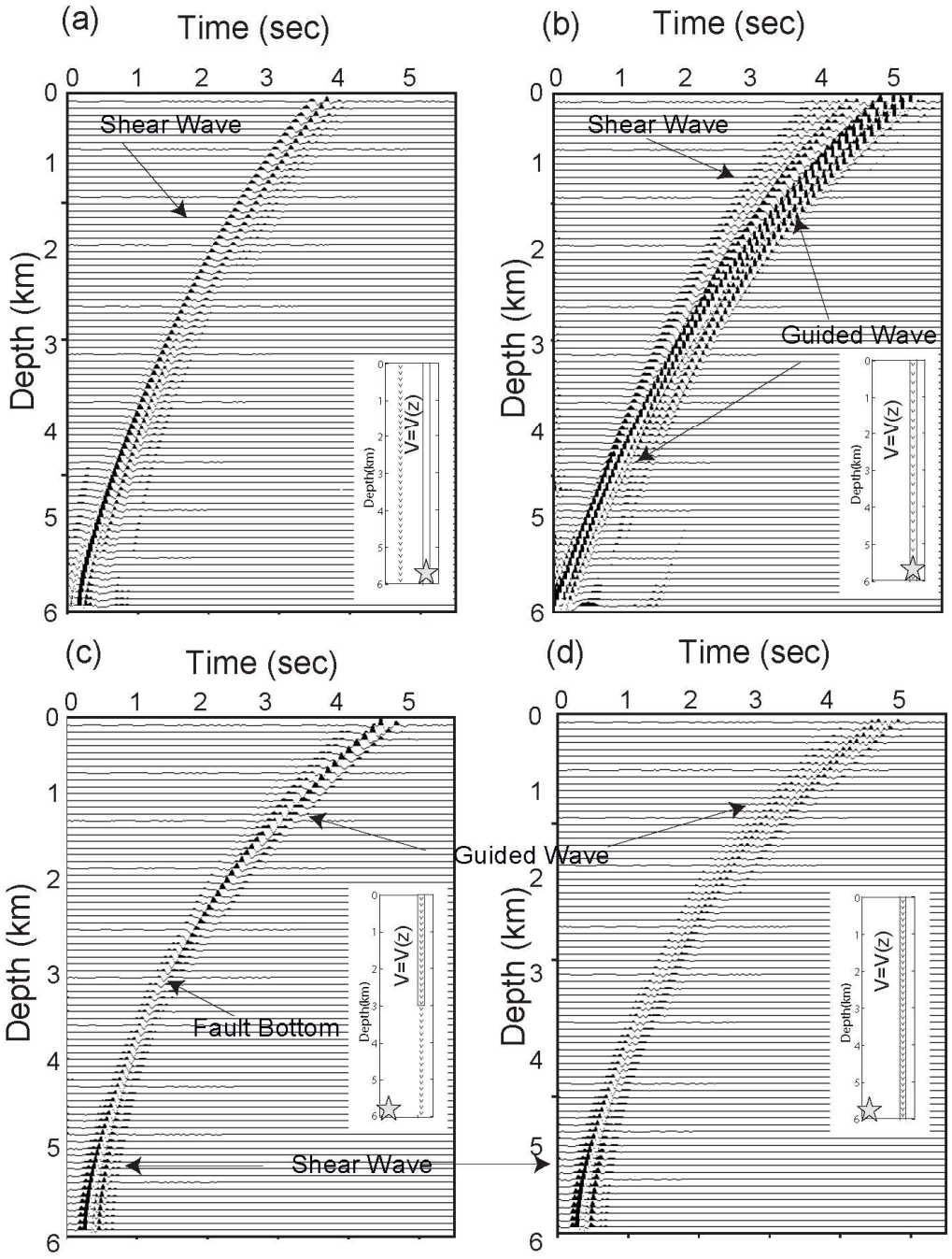

Fault-parallel seismic sections for the velocity models of Figure 1.1. The index in the bottom corner of each panel denotes the fault geometry and source-receiver positions. (a) For receivers off the fault, only direct S-waves exist. (b) For a source and receivers inside the fault, trapped waves dominate. (c) For the shallow fault model, guided waves are

initiated at the bottom of the fault. (d) For the source outside the deep fault, direct S-waves dominate at depth and guided waves become more prominent towards the surface. The slope (apparent velocity) of the arrivals changes with depth in all of the sections.

Figure 1.6: Analytic group velocity dispersion.

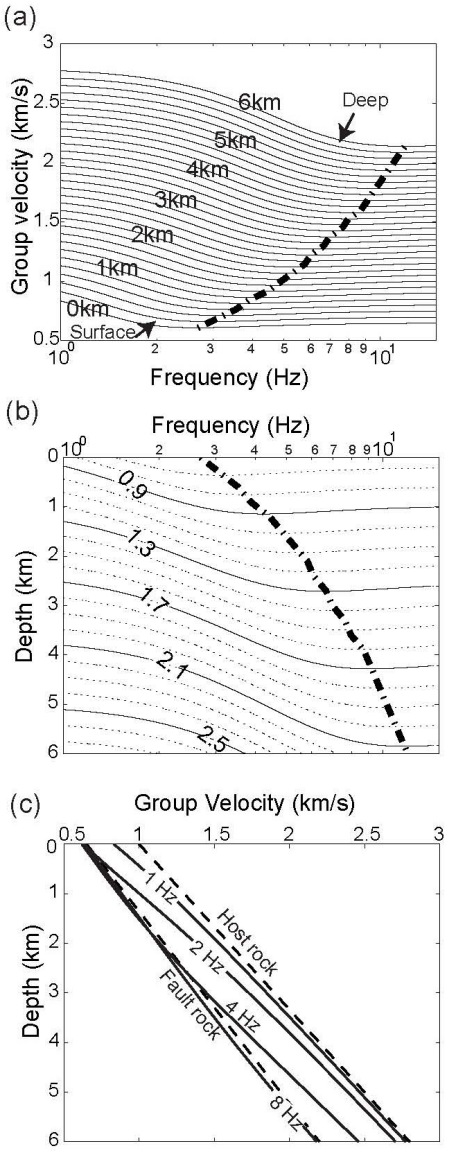

(a) Analytic guided wave group velocity dispersion curves for the model of Figure 1.1a computed at different depths. The dash-dotted line intersects the minimum in group velocity at each depth. Waves with frequency near the minimum are the optimally trapped Airy phase. The dominant frequency increases with depth. (b) GW group velocity (in km/s) as a function of both depth and frequency. Horizontal slices through this image correspond to the lines in (a). The dash-dotted line is the same as in (a). (c) GW group velocity as a function of depth at 1, 2, 4 and 8 Hz (solid lines). The two dashed lines indicate the S

body-wave velocities for the host and fault rocks. The 16-Hz curve is not shown for clarity; it is slightly slower than the fault-rock velocity at the bottom of the model, but is equal to the fault-rock velocity above 3-km depth.

Figure 1.7: Group velocity dispersions calculated from synthetic seismograms.

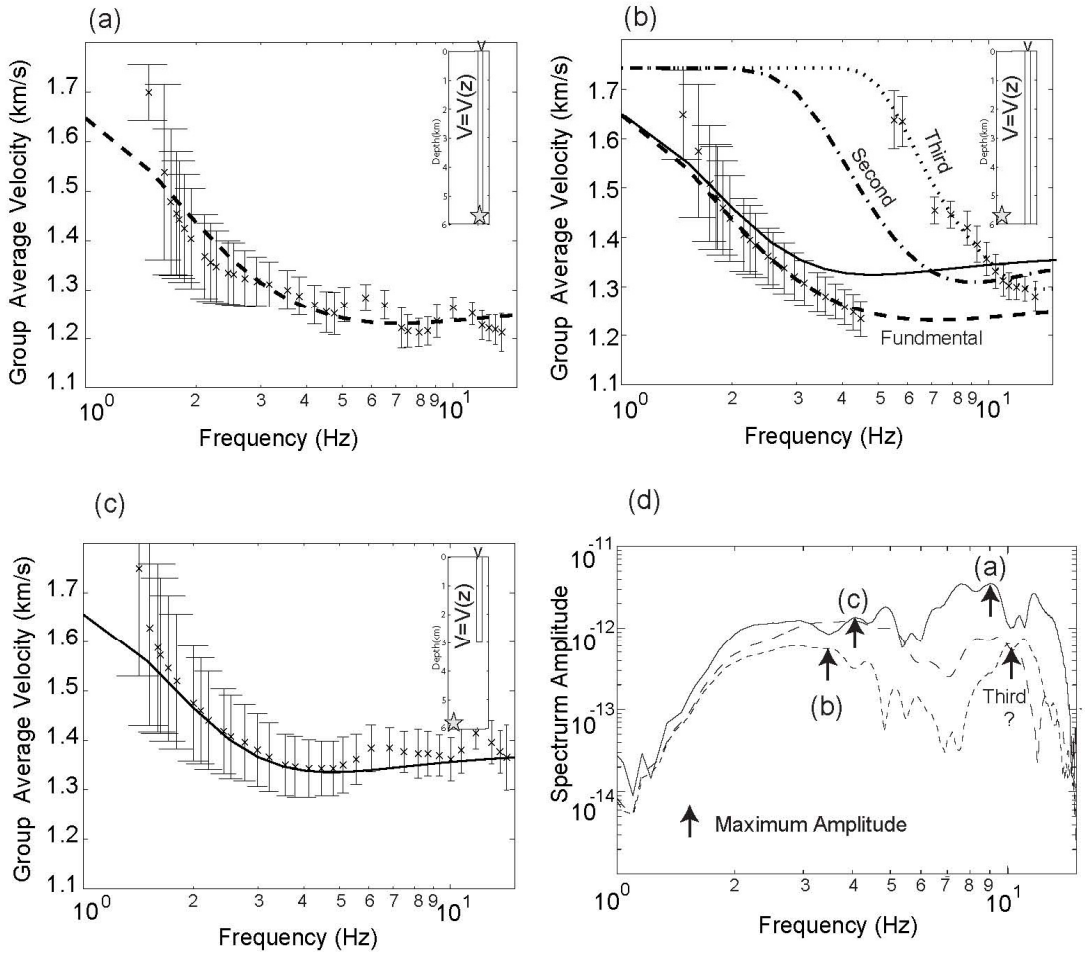

(a-c) Group dispersion curves (symbols with error bars) for traces highlighted in Figure 1.3, computed using the method of Snoke & James (1997). Fault geometry and source-receiver positions are displayed in the corner of each image. Analytic dispersion curves (dashed lines) were computed by integration of travel time from the source to the receiver using the local group velocity of Figure 1.6. The solid lines are the analytic dispersion curves computed using the velocity of Figure 1.6 above 3-km depth and the S-wave velocity below 3 km. Higher order modes are also shown in (b). (d) Amplitude spectra for the seismic traces analyzed in (a)-(c). The maximum amplitude for each spectrum is labeled.

Figure 1.8: Trace envelopes for the fault parallel seismic sections.

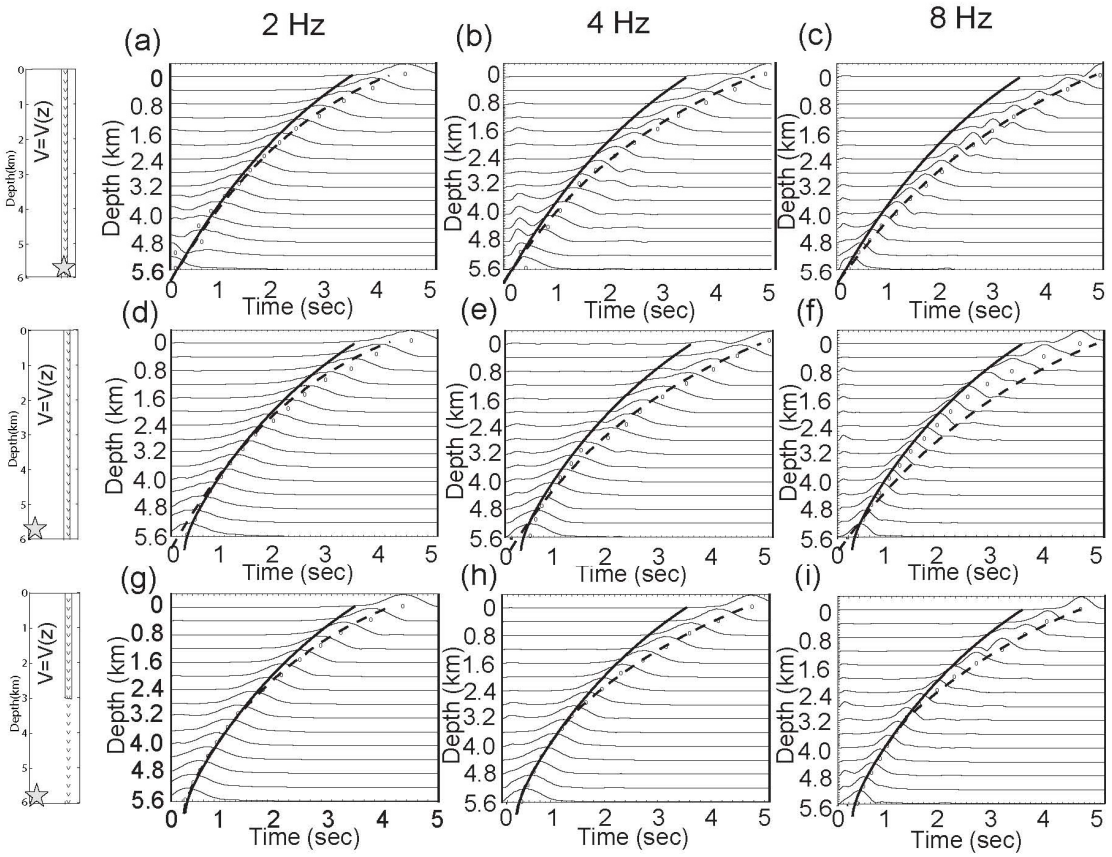

Trace envelopes for the fault-parallel seismic sections of Figures 1.5b-d. The index figures at left indicate the geometry of the fault, source and receivers for each row. In each column, the data have been narrow-band filtered at the indicated frequency prior to computing the trace envelope. Each envelope trace is individually scaled. Circles indicate the travel time picks at the maximum of each envelope trace. Lines indicate travel times computed by integration from the source to the receiver using the host-rock local velocity (solid lines) or the GW local velocity of Figure 1.6 (dashed lines). The solid lines properly account for the source position, while the dashed lines assume a vertical ray path. For the shallow fault (panels g-i), the dashed lines start at the bottom of the fault. The deep and shallow-fault data are indistinguishable at 2 Hz and only subtly different at 4 Hz. Only for the deep fault at 8 Hz (panel f) does the observed travel time differ significantly from the FZGW time, indicating the absence of a fundamental-mode GW.

Figure 1.9: Group travel-time delays of the GW relative to the S-wave.

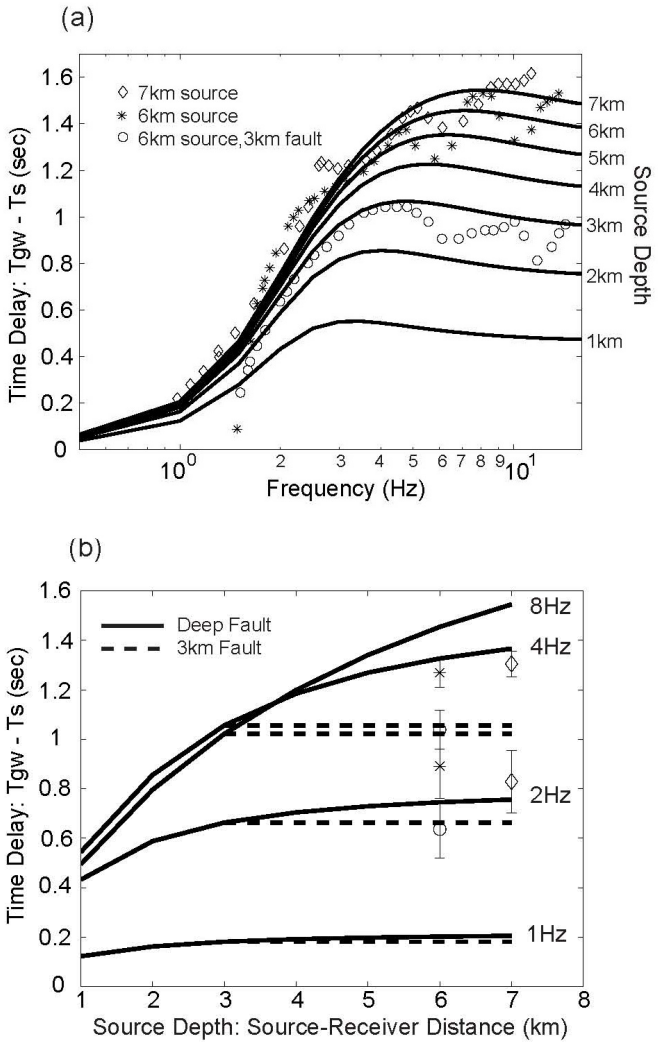

(a) Time delays as a function of frequency for sources at different depths in the fault and a receiver at the surface. Solid lines are integrated from the local group velocity of Figure 1.6. Symbols are measured from the synthetic data of Figures 1.3 and 1.10. (b) Time delays as a function of source depth for the deep fault (solid lines) and the shallow fault (dashed lines) at different frequencies. Measured time delays from (a) for 2 and 4 Hz are displayed as symbols with error bars.

Figure 1.10: 6-km fault versus 7-km fault.

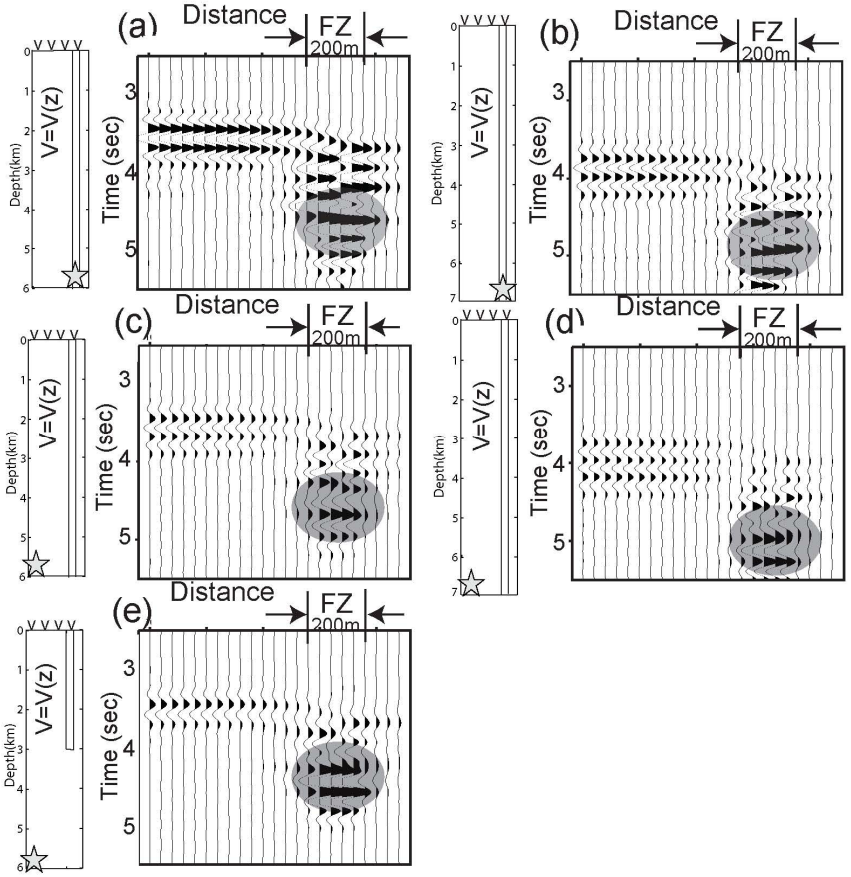

Across-fault seismic sections at the surface for sources at 6-km (left column) and 7-km depth (right column). The source and fault geometry is indicated to the left of each panel. The velocity below 6-km depth is linearly extrapolated from Figure 1.1c. The sections are band-pass filtered from 2 to 4 Hz. At these low frequencies, the guided waves look similar in all of the sections and have nearly identical delay from the body waves.

Chapter 2

Structure of the San Andreas Fault Zone at Depth from Differential Dispersion of Seismic Guided Waves

Summary

Fault-zone guided wave (FZGW) dispersion can be used to image the fault zone (FZ) structure at seismogenic depth. A two-station differential group velocity technique previously used for surface waves was adapted to solve for the local FZ structure between two stations. This method was extended to solve for FZ structure between two earthquakes using arrivals at a single station. The method was tested with finite-difference synthetic data for an inhomogeneous fault, as well as with a pair of shallow earthquakes recorded in the SAFOD borehole. Results from a pair of deep earthquakes recorded in SAFOD borehole indicate that the low-velocity waveguide of the San Andreas Fault extends to >10 km depth. The FZ waveguide at 10-12 km depth is about 150 m wide and the velocity contrast at the fault boundary is >20%, similar to the values in the shallow subsurface. With multiple earthquakes and receivers, FZ structure at seismogenic depth may be derived as a function of fault strike and dip.

Keywords: fault zone, guided waves, dispersion, San Andreas Fault, velocity structure.

2.1 Introduction

Characterizing the internal structure of fault zones (FZs) plays an important role in understanding the faulting mechanisms and earthquake processes on those faults. At major FZs, gouge, fracturing, remineralization and pore-fluid saturation form a zone of low seismic velocity that is tens of meters to a few hundred meters wide (Li *et al.* 2001; Ben-Zion & Sammis 2003; Gettemy *et al.* 2004), comparable in scale to the damage zone observed in exhumed faults (Chester & Logan 1986; Chester *et al.* 1993; Schulz & Evans 2000; Scholz 2002). The constructive interference of critically reflected and refracted seismic waves within this low velocity waveguide can allow the generation and

propagation of FZ guided waves (GWs) (Ben-Zion & Aki 1990; Igel *et al.* 2002). In the past two decades, GWs have been observed and used to characterize the internal structure of several major continental faults (e.g., Li *et al.* 1994; 1997; Michael & Ben-Zion 1998; Li *et al.* 2000; Ben-Zion *et al.* 2003; Li *et al.* 2004; Mizuno & Nishigami 2006).

A number of numerical studies have investigated the dependence of FZGWs upon fault width, velocity and velocity contrast, Q attenuation, and changes of fault geometry (Li & Vidale 1996; Igel *et al.* 2002; Jahnke *et al.* 2002; Fohrmann *et al.* 2004). Most modeling and field studies involve a single source recorded at a single station or at a local station array crossing the fault at a single point. For this geometry, the modeling of GWs in a fault is associated with strong trade-offs among the key fault parameters. While numerous studies have produced FZ models that vary with depth throughout the seismogenic depth range (Li *et al.* 2000; 2001; 2002; 2004), the uniqueness of some of these models has been debated (Peng *et al.* 2003; Fohrmann *et al.* 2004; Lewis *et al.* 2005). Wu *et al.* (2008) showed that the ubiquitous increase in velocity with depth in the crust causes the deeper fault zone to efficiently guide waves at higher frequencies than in the near-surface fault. Fault structure at seismogenic depth requires the analysis of data at higher frequencies than the GWs that dominate observations at the surface. FZGW analyses to date have focused on the dominant signal and thus provide few constraints at seismogenic depth. In this paper, we present a new method that uses GWs to provide better constraints upon deep FZ structures.

Similar to FZGWs, surface waves are dispersive waves that are trapped in Earth's near-surface low-velocity layers. A pair or array of stations distributed on Earth's surface, parallel to the waveguide, is commonly used to invert surface waves for the local velocity structure of the crust and upper mantle between the stations (Woods & Okal 1996; Snoke & James 1997; Forsyth *et al.* 1998; Friederich 1998; Pollitz 1999; Priestley & Tilmann 1999; Li *et al.* 2003; Larson *et al.* 2006). These methods measure the relative arrival times or phase as a function of frequency and compute the dispersive phase or group velocity between stations. Velocity dispersion is then inverted to derive local depth-dependent velocity structure. This method can be extended to find 3-dimensional velocity structure using several station arrays (e.g. Warren *et al.* 2008).

We propose a similar method for the analysis of FZGWs. The new method measures the differential arrival times of FZGWs at a pair of stations for a single earthquake or for a pair of earthquakes at a single station within the FZ to compute the local velocity dispersion and FZ properties between the stations/events. The method is first demonstrated with numerical data from a spatially varying fault. It is then applied to data from the SAFOD borehole through the San Andreas Fault.

2.2 Method

2.2.1 Analytic dispersion

The same wave equations used to describe surface wave dispersion can be used to describe FZGW dispersion. The differences are the boundary conditions; instead of a free surface, high-velocity material bounds both sides of the fault. A guided shear wave exists that is analogous to surface Love (SH) waves, and a guided coupled P-S wave exists analogous to Rayleigh (P-SV) waves. However for dipping faults, the Love-type and Rayleigh-type waves are not horizontally and vertically polarized, but have fault-parallel and fault-perpendicular motion respectively. The Love-type GW for a homogeneous low-velocity FZ layer embedded in two half-spaces obeys the following dispersion equation (Ben-Zion & Aki 1990):

$$\tan[W 2\pi f(\beta_{FZ}^{-2} - c^{-2})^{1/2}] = \frac{2\mu_{FZ}(\beta_{FZ}^{-2} - c^{-2})^{1/2}\,\mu_{HS}(c^{-2} - \beta_{HS}^{-2})^{1/2}}{\mu_{FZ}^{2}(\beta_{FZ}^{-2} - c^{-2}) - \mu_{HS}^{2}(c^{-2} - \beta_{HS}^{-2})} \qquad (2.1)$$

where c is the phase velocity, W is the FZ width, f is the frequency, μ is the shear modulus, β is the shear-wave velocity, and HS refers to the half-spaces on both sides of the fault. Using a similar derivation, Rayleigh-type GW dispersion equations for a homogeneous FZ are given by Lou *et al.* (1997) and in the Appendix. The relationship between the phase velocity c and the frequency from the above equations can be solved numerically. Group velocity, U, the speed of the maximum energy at that frequency, is the derivative of the phase velocity c with respect to wavenumber k:

$$U = \frac{d\omega}{dk} = c + k\frac{dc}{dk} \tag{2.2}$$

where $c=\omega/k$.

The solution of equations (2.1) and (2.2) for the Love-type wave's group velocity in a homogenous FZ model is shown in Figure 2.1 (bottom, solid line). Low-frequency waves with longer wavelengths arrive earlier than high-frequency waves because they sample rocks outside the fault zone. The group velocities of low and high-frequency waves approach the rock velocities outside and inside the fault rock, respectively. The waves with frequencies near the local minimum in group velocity arrive at the same time, producing a strong arrival (called the Airy phase) that dominates the seismogram (pg. 332, Ben-Menahem & Singh 1981). The wavelengths of the Airy phase are on the order of the width of the fault.

2.2.2 Measured dispersion

The determination of group velocities from seismic traces uses the frequency-time analysis of Snoke and James (1997). GWs are passed through a narrow-band-pass, zero-phase, Gaussian filter at a set of center frequencies, and then the envelope for each frequency is computed. The maximum of the envelope trace is automatically picked and plotted as an x for each frequency, and the amplitudes are contoured. The maximum amplitude corresponds to the group arrival time of the GWs at that frequency. The vertical lines span +/-1 dB decrease from the maximum for that frequency, and we interpret those spans as error estimates. This error estimate is relative and does not represent a well-defined statistical error. Other local maxima on the envelope trace may indicate other phases or higher order modes. The path-averaged group velocity is computed by dividing the source-receiver distance by the group arrival time.

Figure 2.1 (top) shows a synthetic seismogram generated using wave-number integration (Herrmann 2002) for a low-velocity layer (fault) embedded in two half-spaces. The group velocity dispersion curve (symbols with error bars in Figure 2.1, bottom) was measured using the above method. The observed and analytic dispersion curves are

consistent except at low frequencies. Even there, the deviations are within the estimated errors.

2.2.3 Two-station technique

A two-station group or phase -velocity technique has been commonly used in surface wave studies (Woods et al 1991; Snoke & James 1997; Forsyth *et al.* 1998; Friederich 1998; Pollitz 1999; Priestley & Tilmann 1999; Li *et al.* 2003; Larson *et al.* 2006). Two stations aligned along the surface wave propagation path (a great circle for surface waves) can be used to determine the structure between the stations by analyzing the differences between the observed surface waves. Because the waves share a common propagating path to the first station, the difference in arrival time is caused solely by the structure between the two stations. The group arrival times at each frequency, *t(f)* , are measured for each seismogram using the method described above. The interstation group velocities *V(f)* are computed by dividing the distance between the stations, Δd , by the difference in arrival times:

$$V(f) = \frac{\Delta d}{t_2(f) - t_1(f)} \tag{2.3}$$

If the two stations are not perfectly aligned along the propagation path, the distance Δd should be replaced by the distance between wavefronts at the two stations or the difference in distances from the earthquake. Then the interstation group velocity dispersion curve can be inverted for depth-dependent velocity structure perpendicular to the waveguide.

The same method can be applied to FZGWs with two stations that are aligned with an earthquake. Local across-fault properties between the two stations can be derived, such as the FZ thickness and S-wave velocities, from the GW differential group arrival times.

For surface waves, one can easily deploy seismometers along anticipated propagation paths. For FZGWs, however, seismometers would need to be deployed within the fault

plane. Deployments along the surface trace of the fault would provide information primarily about shallow fault structure, which is not as interesting as structure at seismogenic depth. We therefore propose using traveltime reciprocity to replace the two-station method with a single station and two earthquakes, deriving FZ structure between the earthquakes.

Two earthquakes that have different source signatures (slip direction, fault orientation, finite fault-plane slip) will result in quite different waveforms even if they occur at the same spot. Generally the dependence of group velocity on focal mechanism is negligible. It is assumed that the earthquakes are sufficiently small that they can be considered temporally impulsive point sources. Any group time delay caused by finite fault-plane slip is thus much smaller than the travel time between the sources.

2.3 Synthetic Data Tests

Since the applications of the two-station and two-earthquake methods are new for FZGWs, they were systematically tested using synthetic seismic data.

2.3.1 Model

Synthetic data were computed in a three-dimensional (3-D) velocity model that consists of a linear velocity gradient with depth (Figure 2.2). The P and S wave velocities (Figure 2.2b, Table 2.1) are modified from the model of Li *et al*. (2004) for the San Andreas Fault at Parkfield. Such an increase with depth is the norm in the crust due to the effects of pressure closing pores and fractures (Wu *et al.* 2008). The waveguide is 200-m wide and extends to 6-km depth. A double-couple source ($M_{xy} = M_{yx} = M_0$) with strike-slip dislocation mechanism in the y direction (parallel the fault strike) is placed at 6-km depth slightly off center within the fault. A line of seismometers is placed across the fault at the surface directly above the source, with a spacing of 40 meters (Figure 2.2a). A second vertical line of seismometers is placed within the FZ waveguide at 80-m spacing to record data along the path of wave propagation (Figure 2.2a). The predominant GWs from this source and source-receiver geometry will be Love-type waves with

fault-parallel particle motions in the y-direction. Only the y-component seismograms will be discussed here, however a similar analysis was also performed with an explosive source for x-component across-fault recordings of Rayleigh-type GWs.

Assuming the velocity model is locally homogenous, the analytic group velocity dispersion can be calculated at each depth using equations (2.1-2.2) (Figure 2.3). The group velocity gradually increases with depth at each frequency. The dominant frequency also increases with depth, with low frequency waves being more efficiently trapped at shallow depth and high frequency waves more efficiently trapped at deep depth (Wu *et al.* 2008).

Synthetic seismograms were computed using a 3-D elastic finite-difference (FD) algorithm (Kelly *et al.* 1976) with the parameters in Table 2.1. An absorbing boundary condition (the Perfect Matched Layer of Chew & Liu, 1996) was used to reduce reflections from the model surfaces. The source wavelet (Figure 2.2c) is band-limited to 0-15 Hz to avoid numerical aliasing. The algorithm was tested by comparing results for a homogeneous fault model to results for the same model from wave-number integration (Herrmann 2002).

2.3.2 Synthetic seismograms

Figure 2.4a shows the synthetic data for the surface array across the fault. The GWs are clearly visible, stronger and later than the shear-wave energy and decaying rapidly outside the waveguide. Figure 2.4b shows the synthetic seismograms from the array that is parallel to and within the waveguide (Figure 2.2a), illustrating the GWs propagating up the fault. The curvature of the GWs in this plot demonstrates the waveguide velocity decreasing towards the surface. Dispersion is indicated by the phase velocity (aligned peaks) that is faster than group velocity (trend of the energy packet) and by elongation of the wave train as it propagates upward.

2.3.3 Two-station group velocities

The dispersive group travel times, whole-path velocity, and interstation velocity were

measured for the traces in Figure 2.4b using the method described in Section 2.2. Traces within 2 km of the source were not used because the body and guided waves overlap at low frequencies.

Figure 2.5a displays the source-to-receiver group velocity dispersion for stations at 0.0 and 0.4 km depth (dashed lines) and the interstation group velocity between them (symbols with error bars). The observed interstation velocity closely matches the analytic group velocity at 0.2 km depth (Figure 2.3a, solid line in Figure 2.5a) and does not match the whole-path group velocity.

Figure 2.6a shows the measured travel times for every trace in Figure 2.4b. Analytic travel times at each frequency can be computed from the integral of the inverse of the local group velocity (Figure 2.3b) from the source to receiver. These analytic travel times (Figure 2.6b) closely match the calculated times, confirming that GW propagation is sensitive only to the local FZ properties.

The group arrival times (Figure 2.6a) were used to compute the local group velocities between pairs of stations at all depths. The calculated interstation group velocity for every pair of stations 80-m apart (Figure 2.6c) is noisy, but has the same depth-frequency pattern as the analytic local group velocity (Figure 2.6f). Although the measured travel times (Figure 2.6a) are similar to the analytic times (Figure 2.6b), the finite-difference derivatives of the times accentuate the measurement errors. The interstation velocity plot is improved by using pairs of stations 400-m apart (Figure 2.6d). Better statistics can be achieved by smoothing, averaging, or curve-fitting the arrival times in both space and frequency. Figure 2.6e shows local group velocity after applying a 5×5-point (400 m in depth and 1.4 dB in frequency) moving average filter to Figure 2.6a prior to differentiation. Velocity near the surface is better constrained than at depth because the slower velocity allows more accurate determination of the larger interval travel time.

2.3.4 Two-event group velocities

Figures 2.5a and 2.6 show that the two-station method obtains the group velocity dispersion between the stations. Similar to the two-station technique, a station recording

two events that are aligned along the GW propagation path would obtain the group velocity dispersion between the two events.

To test the two-event method, a set of synthetic seismograms was computed using the same model (Figure 2.2) and a source at 5.2 km depth in the waveguide. The group velocities were calculated from the surface seismogram for both sources (dashed lines, Figure 2.5b). The same analysis as for the two-station method was applied to obtain the inter-event group velocity dispersion curve (symbols with error bars, Figure 2.5b). This differential dispersion matches the analytic group velocities at 5.6 km depth (solid line, Figure 2.5b) and does not match the whole-path group velocity. The two-event technique is more applicable than the two-station technique because it can use a single seismometer deployed at the Earth surface to map out FZ structure at seismogenic depth.

A double-couple source with strike-slip motion in the plane of the fault was used to generate synthetic seismograms used in the above tests. To test the effect of different focal mechanisms on the two-earthquake method, synthetic seismograms were computed in the same velocity model (Figure 2.2), with an obliquely oriented focal mechanism ($M_{xy} = M_{yx} = 3M_0$, $M_{xz} = M_{zx} = M_0$, $M_{yz} = M_{zy} = 2M_0$) at 6 km depth. The waveforms of the two surface traces are very different (Figure 2.5c). However, the calculated whole-path group velocities for the two traces are identical (Figure 2.5d), suggesting a negligible dependence upon focal mechanism for point sources.

A nodal plane of the source radiation pattern might prevent the generation of GWs. For example, a strike-slip source centered directly underneath a shallow fault would result in a vanishing or weak trapped wave (Fohrmann *et al.* 2004). Motion on a large slip fault plane could cause a group time delay at the source.

2.4 Application to SAFOD Borehole Data

The San Andreas Fault Observatory at Depth (SAFOD) is a deep borehole observatory that allows direct measurement of the physical conditions within the San Andreas Fault (SAF) through the earthquake cycle (Hickman *et al.* 2004; Hickman *et al.*

2007, http://www.earthscope.org/observatories/SAFOD/). Beginning in January 2006, two 3-component 15-Hz seismometers were placed in the SAFOD main hole at a depth of ~3 km within the fault damage zone (Ellsworth *et al.* 2007). Technical problems were encountered, and the instruments were removed and redeployed several times at similar (but not identical) locations. A total of 106 days of data were recorded before removal of the instruments in March 2007. Data from these down-hole seismometers have very low noise compared to surface data, and the signal contains higher frequencies that have not been attenuated by near-surface geology. The seismic data were downloaded from the Northern California Earthquake Data Center (NCEDC) (http://www.ncedc.org/).

About 250 events in the 30×30 km area centered at SAFOD were recorded by the down-hole SAFOD station. The instrument response was removed and the three-component data were transformed to vertical, fault-parallel (45^0 NW) and fault-perpendicular (45^0 NE) components. Dispersion analysis was performed for each event. About 50 events produced clear GWs with dispersive group velocities. . Almost all the events lie on the SAF trace (Figure 2.7). Most of the events northwest of SAFOD are shallow (2-5 km depth) with magnitudes smaller than 2. Southeast of SAFOD, there are a few shallow micro-earthquakes (magnitude <1) and a few earthquakes at >10 km depth.

2.4.1 Dispersion of Shallow SAF events

Figure 2.8a shows vertical component seismograms of two events (#162 & #183 in Figure 2.7) at similar depth as but different distances from the borehole seismometer. The late, strong arrivals interpreted as FZGWs cannot be surface waves because surface waves at these frequencies have wavelengths and depth sensitivity much smaller than the depth of the SAFOD borehole seismometer. The source-receiver geometry indicates an almost horizontal wave propagation path, so the fault-parallel vertical component should be dominated by the Love-type wave. Most of the events in Figure 2.7 have similar strong FZGWs. If the FZ is assumed to be uniform along strike over the 5 km distance between the events and the station, the whole-path group velocity dispersion curves for the two events and the inter-event group velocity will be the same and will be consistent with the SAFOD borehole sonic log. These assumptions are tested to verify the two-event

method with real data.

The measurement of velocity between two earthquakes requires accurate relative hypocenters and earthquake origin times. Double-difference or similar relative earthquake relocation methods utilizing differential arrival times can improve relative earthquake hypocenters and times by at least an order of magnitude (Nadeau *et al.* 2004). Unfortunately, accurate relative locations are not yet available for the events recorded downhole at SAFOD. Instead, the well log sonic velocities (Figure 2.8c) were used to re-locate the relative distance of the two earthquakes from the SAFOD station. The P- and S-wave first arrival times were picked at the SAFOD station and inverted using the well-log velocities from the fast (southwest) side of the SAF (P-wave, 5.4 km/s; S-wave, 3.0 km/s). This is essentially a 1-D double-difference inversion for relative distance from the borehole. The relocation uses independent arrivals but very similar wave paths to the FZGWs. The original hypocenters were 2.26 and 4.7 km from SAFOD, but they were significantly relocated to 2.63 and 5.0 km from SAFOD, respectively.

Using these distances and related adjustments to the event times, the whole-path group velocity dispersion curves (dashed lines, Figure 2.8b) and inter-event dispersion (symbols with error bars, Figure 2.8b) were computed. The arrival times are hard to pick for frequency above 20 Hz because signals are weak. The two single-station whole-path dispersion and the two-station dispersion curves are all similar. This is consistent with the SAF having little variation along strike over this distance at this depth and suggests that the two-event method works.

The seismic velocities from the SAFOD well logs (Figure 8c, Hickman *et al.* 2007), adjusted for oblique penetration of an assumed vertical fault, indicate a 180-m wide low-velocity FZ containing a 30-m wide highly-damaged fault core with even lower velocity. A velocity model consisting of eleven homogenous vertical layers bounded by two half-spaces (solid lines, Figure 2.8c) was created to model the observed FZGWs. Sources were placed within the core zone and the broader low-velocity zone (stars, Figure 2.8c). Synthetic seismograms were computed using wave-number integration (Herrmann 2002) for a receiver array across the FZ at 3 km from the source. If and only if

both the source and receiver are in the core zone, strong GWs with frequency up to 100 Hz are created. For all the other cases, such as the seismogram in Figure 2.8a (bottom), the dominant frequency of the GWs is about 17 Hz, corresponding to the width of the wider less-damaged FZ. Since the SAFOD receivers were not deployed within the core zone (Figure 2.8c), high frequency GWs are not expected. GWs were observed only below ~20 Hz. The dispersion curve for the synthetic seismic data (solid line, Figure 2.8c) has the same shape but is a little faster than the dispersion for the real data. This may be due to systematic bias in the real-data measurements or to scaling between ultrasonic and seismic frequencies in a highly layered medium. However, it appears to validate the method for obtaining FZ information at seismogenic depth.

2.4.2 Dispersion of Deep SAF events

A few deep events were located to the southeast of the SAFOD station but pairs of deep events approximately collinear with the station are rare. The seismograms of Events #197 and #98 show strong FZGWs (Figure 2.9). These two events are below and southeast of SAFOD at 10.6 and 12.6 km depth (8.34 and 11.28 km straight-line distance) and event #197 lies close to the wave propagation path of event #98. For this geometry, the horizontal fault-parallel seismic component in Figure 2.9a is dominated by Love-type GWs, and the other two components are Rayleigh-type GWs.

Like the shallow events, relative relocation was performed for the two deep events. Rather than using a constant velocity, a 1-D velocity model (Table 2.2) was adapted from the southwest fast side of the SAFOD velocity model of Custodio *et al.* (2005), which was modified from the 3-D velocity models of Eberhart-Phillips and Michael (1993) and Thurber *et al.* (2003). The re-located relative distance from the station to the hypocenters is 3.38 km, 0.44 km farther than the catalog locations.

The whole-path group velocities for the horizontal fault-parallel component (dashed black lines. Figure 2.9b) are dispersive over a broad frequency range. Group arrival time picks were difficult to make at some frequencies, so they were interpolated with a low-order polynomial prior to computing the inter-event times. The inter-event group

velocity (symbols with error bars, Figure 2.9b) is strongly dispersive from 4 to >20 Hz. Below 4 Hz, picking inaccuracy is suggested by the inconsistent shapes of the whole-path dispersion curves, resulting in a slow inter-event velocity that is probably erroneous. At 4 Hz, the inter-event velocity approaches the S-wave velocity of 3.6 km/s at the depth of the events (Table 2.2). Dispersion to lower velocity at higher frequency indicates a low-velocity SAF waveguide that extends to at least 12 km depth. If the waveguide were restricted to a shallow depth, inter-event velocity would not be dispersive and would equal the S-wave velocity.

Modeling of FZGWs to derive fault structure is highly non-unique. However, velocity dispersion is primarily sensitive to the S-wave velocity and the thickness of the FZ. As a simple approximation, analytic dispersion curves were computed in a homogeneous layer bounded by two half-spaces and compared to the observed inter-event dispersion curve. S-wave velocities of 3.6 and 3.8 km/s were adapted from Custodio *et al*. (2005) for the southwest and northeast sides, respectively, of the SAF at ~12 km depth. Analytic dispersion for Love-type waves was computed for FZ S-wave velocities of 2.7, 2.75, and 2.8 km/s (green lines, Figure 2.9b) and waveguide thicknesses of 120, 150 and 180 m (red lines, Figure 2.9b). The observed deep dispersion curve is best matched by a 150-m wide waveguide with a velocity of 2.75 km/s. The 150-m modeled FZ waveguide thickness at 11-12 km depth is only a little thinner than the 180-m thickness at the depth of the SAFOD borehole. The strong modeled velocity reduction of ~26% is also comparable to the ~25% contrast at SAFOD.

Whole-path and inter-event dispersion curves were also derived for the Rayleigh-type GWs in the horizontal fault-perpendicular component (Figure 2.9d). Dispersion is observed from 2 to 16 Hz, but the group arrival time was difficult to pick at higher frequency. Analytic Rayleigh-type wave dispersion was computed in the same fault models used for the fault-parallel component (red lines, Figure 2.9d). The shape and velocity range of the inter-event dispersion curve is consistent with the model, but the lack of high-frequency picks makes it difficult to confirm the model. The vertical component seismograms (Figure 2.9e) are also dominated by Rayleigh-type GWs, however their dispersion curves are very noisy.

2.5 Discussion and Conclusions

Knowledge of the physical conditions inside FZs is crucial to understanding the earthquake process. This paper presents a new method that uses FZGWs to map fault structure at seismogenic depth. The method adapts the two-station method that is well established for studying dispersive surface waves and is used to solve for local waveguide properties between the stations. Since seismometers cannot be deployed in arrays in the subsurface parts of the fault, the method was extended to use pairs of earthquakes, deriving FZ properties at depth. The technique was thoroughly tested with synthetic data for an inhomogeneous FZ (Figures 2.5, 2.6). In these synthetic tests, a double-couple source was employed and Love-type GWs were analyzed. Synthetic tests were also performed with an explosive source for Rayleigh-type GWs, with similar success.

The method was calibrated with real data by analysis of shallow earthquakes recorded in the SAFOD borehole at a similar depth. The results are internally consistent with a roughly homogeneous fault at a constant depth for several km along strike. While the results did not match the sonic log velocities exactly, the shape and frequency range of the dispersion curve was successfully reproduced.

Figure 2.6 illustrates the use of an array to derive 1-D fault structure and improve the statistics beyond those of a pair of stations. The example used a 1-D array of receivers and a single source, but a similar analysis can be applied to many earthquakes distributed on the fault plane to derive a 2-D map of FZ structure. With multiple sources and receivers, it can be extended to full FZ tomography, analogous to established surface-wave array methods (e.g., Forsyth *et al.* 1998; Friederich 1998; Pollitz 1999; Li *et al.* 2003).

The local group or phase velocity dispersion curve for surface waves is used to invert for seismic velocity as a function of depth, perpendicular the waveguide (e.g., Woods & Okal 1996; Snoke & James 1997; Priestley & Tilmann 1999; Larson *et al.* 2006). In a similar manner, the local FZ dispersion curve may be inverted for the layered waveguide structure perpendicular to the fault. Inversion is probably more non-unique than for

surface waves due to the two-sided nature of the FZ waveguide. Full inversion is beyond the scope of this work, but a single-layer waveguide model for the deep SAF was derived by systematic parameter search.

The two earthquakes at 10-12 km depth recorded at SAFOD show inter-event FZGW dispersion, suggesting a low-velocity FZ waveguide between the earthquakes. The time duration of the GWs for the four selected earthquakes increases with source-receiver distance (Figures 2.8a, 2.9a), indicating a relatively continuous low velocity zone connecting the SAFOD station and these events. A deep SAF waveguide is consistent with previous FZGW models at SAFOD and nearby Parkfield (Li *et al.* 1998; 2006; Li & Malin 2008). Although this is a single data point on a single fault and therefore requires confirmation, it contradicts the argument (Ben-Zion *et al.* 2003; Ben-Zion & Sammis 2003; Peng *et al.* 2003; Fohrmann *et al.* 2004; Lewis *et al.* 2005) that the FZ waveguide is usually restricted to shallow (<5 km) depth.

Host-rock and FZ velocities increase with depth, causing the dispersive group velocities to increase with depth (Wu *et al.* 2008). The measured inter-event group velocities between 10-12 km depth (symbols, Figure 2.9b,d) are faster than the whole-path group velocities from ~11 to 3 km depth (dashed dark lines, Figure 2.9b,d), which in turn are faster than the group velocities at ~3 km depth (Figure 2.8b). In each case, the observed maximum velocity at low frequency is comparable to the host rock velocity from body wave tomography. A velocity increase with depth also causes the GW dominant frequency to increase with depth (Wu *et al*. 2008; Figure 2.3). While the difference is difficult to measure, the dispersion curve of Figure 2.9b is shifted to higher frequency by an amount consistent with the ~30% increase in velocity. This suggests that the low-velocity FZ waveguide does not get much narrower at >10 km depth, in contrast to previous models at SAFOD and Parkfield (Li *et al.* 2004; Li & Malin 2008). Modeling of the inter-event dispersion at 10-12 km depth (red and green lines, Figure 2.9b) confirms that the FZ waveguide is about 150 m wide, not much narrower than the 180-m wide FZ at the depth of the SAFOD borehole.

Wu *et al.* (2008) showed that determination of fault structure at seismogenic depth

requires the analysis of data at higher frequency than the GWs that dominant at the surface. Surface observations of FZGWs at SAFOD indicate a surface waveguide with a width of ~200 m, similar to the width in this study, but a much slower surface FZ velocity of 0.6-0.8 km/s and correspondingly much lower dominant frequencies of <5 Hz (Li *et al.* 1997; 2004). The damage zone of faults has been modeled as having a very high attenuation, especially near the surface (Li *et al.* 2004; Li & Malin 2008). Borehole observations such as those in SAFOD avoid the highly attenuating near-surface layer, preserving signals at higher frequency than surface stations. In addition, a deep borehole station like SAFOD can be too deep to record surface waves at the frequencies relevant to FZGWs, removing a potentially interfering signal.

This study provides the first direct determination of internal FZ structure at seismogenic depth. However due to the limited deployment to date of SAFOD seismometers within the FZ and the small percentage of deep events, the number of data points is sparse. In order to measure continuous fault structure as a function of depth and strike, more data are required. Accurate relative earthquake locations are also necessary. The good news is that both redeployment of the SAFOD borehole seismometer and double-difference relocation of the Parkfield catalog are planned for the near future. The new methods described here can be applied to other faults, illuminating deep FZ structure in three dimensions.

Acknowledgements

We thank the Advanced Research Computing (ARC) at Virginia Tech for providing us with computational facilities. JW received partial support from a Chevron Geophysics Fellowship.

References

Ben-Menahem, A. & Singh, S. J., 1981. Seismic Waves and Sources. Springer-Verlag New York Heidelberg Berlin, 1108 pp.

Ben-Zion, Y. & Aki, K., 1990. Seismic Radiation from an Sh Line Source in a Laterally Heterogeneous Planar Fault Zone. Bulletin of the Seismological Society of America, 80,

971-994.

Ben-Zion, Y., Peng, Z. G., Okaya, D., Seeber, L., Armbruster, J. G., Ozer, N., Michael, A. J., Baris, S., Aktar, M., Kuwahara, Y. & Ito, H., 2003. A shallow fault-zone structure illuminated by trapped waves in the Karadere-Duzce branch of the North Anatolian Fault, western Turkey. Geophysical Journal International, 152, 699-717.

Ben-Zion, Y. & Sammis, C. G., 2003. Characterization of fault zones. Pure and Applied Geophysics, 160, 677-715.

Chester, F. M. & Logan, J. M., 1986. Implications for Mechanical-Properties of Brittle Faults from Observations of the Punchbowl Fault Zone, California. Pure and Applied Geophysics, 124, 79-106.

Chester, F. M., Evans, J. P. & Biegel, R. L., 1993. Internal Structure and Weakening Mechanisms of the San-Andreas Fault. Journal of Geophysical Research-Solid Earth, 98, 771-786.

Chew, W. C. & Liu, Q. H., 1996. Perfectly matched layers for elastodynamics: A new absorbing boundary condition. Journal of Computational Acoustics, 4, 341-359.

Custodio, S., Liu, P. & Archuleta, R. J., 2005. The 2004 M(w)6.0 Parkfield, California,earthquake: Inversion of near-source ground motion using multiple data sets. Geophysical Research Letters, 32 dio: 10.1029/2005GL024417.

Eberhart-Phillips, D. & Michael, A. J., 1993. Three-dimensional velocity structure, seismicity, and fault structure in the Parkfield Region, central California. Journal of Geophysical Research-Solid Earth, 98, 15737-15758.

Ellsworth, W., Malin, P., Imanishi, K., Roecker, S., Nadeau, R. M., Oye, V., Thurber, C. H., Waldhauser, F., Boness, N. L., Hickman, S. & Zoback, M., 2007. Seismology inside the Fault Zone: Applications to Fault-Zone Properties and Rupture Dynamics. Scientific Drilling, 1, 84-87.

Fohrmann, M., Igel, H., Jahnke, G. & Ben-Zion, Y., 2004. Guided waves from sources outside faults: An indication for shallow fault zone structure? Pure and Applied Geophysics, 161, 2125-2137.

Forsyth, D. W., Webb, S. C., Dorman, L. M. & Shen, Y., 1998. Phase velocities of Rayleigh waves in the MELT experiment on the East Pacific Rise. Science, 280, 1235-1238.

Friederich, W., 1998. Wave-theoretical inversion of teleseismic surface waves in a regional network: phase-velocity maps and a three-dimensional upper-mantle shear-wave-velocity model for southern Germany. Geophysical Journal International, 132, 203-225.

Gettemy, G. L., Tobin, H. J., Hole, J. A. & Sayed, A. Y., 2004. Multi-scale compressional wave velocity structure of the San Gregorio Fault zone. Geophysical Research Letters, 31, doi:10.1029/2003GL018826.

Herrmann, R. B., 2002. Computer programs in seismology, an overview of synthetic seismogram computation. Saint Louis University, http://www.eas.slu.edu/People/RBHerrmann/ComputerPrograms.html.

Hickman, S., Zoback, M. & Ellsworth, W., 2004. Introduction to special section: Preparing for the San Andreas Fault Observatory at Depth. Geophysical Research Letters, 31, doi:10.1029/2004GL020688.

Hickman, S., Zoback, M., Ellsworth, W., Boness, N., Malin, P., Roecker, S. & Thurber, C., 2007. Structure and Properties of the San Andreas Fault in Central California: Recent Results from the SAFOD Experiment. Scientific Drilling, 1, 29-32.

Igel, H., Jahnke, G. & Ben-Zion, Y., 2002. Numerical simulation of fault zone guided waves: Accuracy and 3-D effects. Pure and Applied Geophysics, 159, 2067-2083.

Jahnke, G., Igel, H. & Ben-Zion, Y., 2002. Three-dimensional calculations of fault-zone-guided waves in various irregular structures. Geophysical Journal International, 151, 416-426.

Kelly, K. R., Ward, R. W., Treitel, S. & Alford, R. M., 1976. Synthetic Seismograms - Finite-Difference Approach. Geophysics, 41, 2-27.

Larson, A. M., Snoke, J. A. & James, D. E., 2006. S-wave velocity structure, mantle xenoliths and the upper mantle beneath the Kaapvaal craton. Geophysical Journal International, 167, 171-186.

Lewis, M. A., Peng, Z., Ben-Zion, Y. & Vernon, F. L., 2005. Shallow seismic trapping structure in the San Jacinto fault zone near Anza, California. Geophysical Journal International, 162, 867-881.

Li, A. B., Forsyth, D. W. & Fischer, K. M., 2003. Shear velocity structure and azimuthal anisotropy beneath eastern North America from Rayleigh wave inversion. Journal of Geophysical Research-Solid Earth, 108, doi:10.1029/2002JB002259.

Li, Y. G., Vidale, J. E., Aki, K., Marone, C. J. & Lee, W. H. K., 1994. Fine-Structure of the Landers Fault Zone - Segmentation and the Rupture Process. Science, 265, 367-370.

Li, Y. G. & Vidale, J. E., 1996. Low-velocity fault-zone guided waves: Numerical investigations of trapping efficiency. Bulletin of the Seismological Society of America, 86, 371-378.

Li, Y. G., Ellsworth, W. L., Thurber, C. H., Malin, P. E. & Aki, K., 1997. Fault-zone

guided waves from explosions in the San Andreas fault at Parkfield and Cienega Valley, California. Bulletin of the Seismological Society of America, 87, 210-221.

Li, Y. G., Aki, K., Vidale, J. E. & Alvarez, M. G., 1998. A delineation of the Nojima fault ruptured in the M7.2 Kobe, Japan, earthquake of 1995 using fault zone trapped waves. Journal of Geophysical Research-Solid Earth, 103, 7247-7263.

Li, Y. G., Vidale, J. E., Aki, K. & Xu, F., 2000. Depth-dependent structure of the Landers fault zone from trapped waves generated by aftershocks. Journal of Geophysical Research-Solid Earth, 105, 6237-6254.

Li, Y. G., Chester, F. M. & Vidale, J. E., 2001. Shallow seismic profiling of the exhumed Punchbowl fault zone, southern California. Bulletin of the Seismological Society of America, 91, 1820-1830.

Li, Y. G. & Vernon, F. L., 2001. Characterization of the San Jacinto fault zone near Anza, California, by fault zone trapped waves. Journal of Geophysical Research-Solid Earth, 106, 30671-30688.

Li, Y. G., Vidale, J. E., Day, S. A., Oglesby, D. D. & Team, S. F. W., 2002. Study of the 1999 M 7.1 Hector Mine, California, earthquake fault plane by trapped waves. Bulletin of the Seismological Society of America, 92, 1318-1332.

Li, Y. G., Vidale, J. E. & Cochran, E. S., 2004. Low-velocity damaged structure of the San Andreas Fault at Parkfield from fault zone trapped waves. Geophysical Research Letters, 31, 2165, doi:10.1029/2001JB001456.

Li, Y. G., Vidale, J. E. & Malin, P. E. 2006.Low-velocity damage zone on the San Andreas Fault at Depth near SAFOD site at Parkfield delineated by fault-zone trapped waves. Proceedings, IODP-ICDP Workshop on fault zone drilling, Miyazaki, Japan,May 23-25.

Li, Y. G. & Malin, P. E., 2008. San Andreas Fault damage at SAFOD viewed with fault-guided waves. Geophysical Research Letters, 35, doi:10.1029/2007GL032924.

Lou, M., Rial, J. A. & Malin, P. E., 1997. Modeling fault-zone guided waves of microearthquakes in a geothermal reservoir. Geophysics, 62, 1278-1284.

Michael, A. J. & Ben-Zion, Y., 1998. Inverting fault zone head trapped waves with genetic algorithm. EOS, Trans. Am. Geophys. Un., 81, F1145.

Mizuno, T. & Nishigami, K., 2006. Deep structure of the Nojima Fault, southwest Japan, estimated from borehole observations of fault-zone trapped waves. Tectonophysics, 417, 231-247.

Nadeau, R. M., Michelini, A., Uhrhammer, R. A., Dolenc, D. & McEvilly, T. V., 2004. Detailed kinematics, structure and recurrence of micro-seismicity in the SAFOD target

region. Geophysical Research Letters, 31, doi:10.1029/2003GL019409.

Peng, Z. G., Ben-Zion, Y., Michael, A. J. & Zhu, L. P., 2003. Quantitative analysis of seismic fault zone waves in the rupture zone of the 1992 Landers, California, earthquake: evidence for a shallow trapping structure. Geophysical Journal International, 155, 1021-1041.

Pollitz, F. F., 1999. Regional velocity structure in northern California from inversion of scattered seismic surface waves. Journal of Geophysical Research-Solid Earth, 104, 15043-15072.

Priestley, K. & Tilmann, F., 1999. Shear-wave structure of the lithosphere above the Hawaiian hot spot from two-station Rayleigh wave phase velocity measurements. Geophysical Research Letters, 26, 1493-1496.

Scholz, C. H., 2002. The mechanics of earthquakes and faulting Cambridge University Press, Cambridge, United Kingdom (GBR); http://www.cambridge.org.

Schulz, S. E. & Evans, J. P., 2000. Mesoscopic structure of the Punchbowl Fault, Southern California and the geologic and geophysical structure of active strike-slip faults. Journal of Structural Geology, 22, 913-930.

Snoke, J. A. & James, D. E., 1997. Lithospheric structure of the Chaco and Parana Basins of South America from surface-wave inversion. Journal of Geophysical Research-Solid Earth, 102, 2939-2951.

Thurber, C., Roecker, S., Roberts, K., Gold, M., Powell, L. & Rittger, K., 2003. Earthquake locations and three-dimensional fault zone structure along the creeping section of the San Andreas fault near Parkfield, CA: Preparing for SAFOD. Geophysical Research Letters, 30, dio:10.1029/2002GL016004.

Warren, L. M., Snoke, J. A. & James, D. E., 2008. S-wave velocity structure beneath the High Lava Plains,Oregon, from Rayleigh-wave dispersion inversion. Earth and Planetary Science Letters, doi: 10.1016/j.epsl.2008.07.014.

Woods, M. T., Leveque, J. J., Okal, E. A. & Cara, M., 1991. 2-Station Measurements of Rayleigh-Wave Group-Velocity Along the Hawaiian Swell. Geophysical Research Letters, 18, 105-108.

Woods, M. T. & Okal, E. A., 1996. Rayleigh-wave dispersion along the Hawaiian Swell: A test of lithospheric thinning by thermal rejuvenation at a hotspot. Geophysical Journal International, 125, 325-339.

Wu, J., Hole, J. A., Snoke, J. A. & Imhof, M. G., 2008. Depth extent of the fault-zone seismic waveguide: effects of increasing velocity with depth. Geophys. J. Int., 173, 611-622.

Table 2.1: Parameters for 3-D finite-difference simulations

Model Size		1000 m × 2000 m × 6000 m	
Grid Spacing		8 m	
Time Step		0.5 ms	
Source Type		$M_{xy} = M_{yx} = M_0$	
Frequency filter		high cut starting at 15 Hz	
Fault Zone Width		200 m	
Parameters 0 - 6 km depth	P-wave Velocity (km/s)	S-wave Velocity (km/s)	Density (g/cm^3)
Host rock	2.4 – 6.1	1.0 - 2.8	2.54 - 2.74
Fault Zone	1.5 - 4.5	0.65 – 2.2	1.96 - 2.17

Table 2.2: 1-D velocity model of southwest side of SAFOD

Depth (km)	Vs (km/s)	Vp (km/s)	Density (g/cm^3)
0.0	1.1	2.0	2.0
1.0	2.0	3.5	2.3
2.0	2.5	4.5	2.3
3.0	3.0	5.2	2.5
3.5	3.2	5.7	2.7
5.8	3.6	6.2	2.7
14.1	3.6	6.8	2.8
17.1	4.3	6.8	2.8
20.4	4.3	7.3	2.8

Figure 2.1: A homogenous fault zone and the dispersion curve.

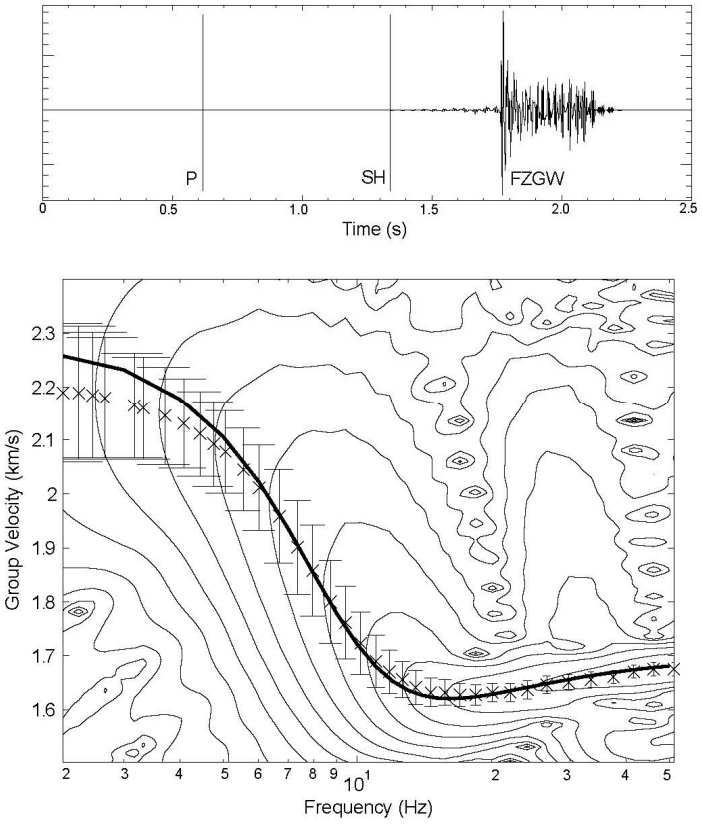

Synthetic seismogram (top) and group velocity dispersion curve (bottom) for a homogenous fault model. S-wave velocity is 1.7 km/s inside the 100-m wide fault and 2.3 km/s outside. The double-couple fault-parallel source generates Love-type GWs without P waves in the component that is parallel to the fault, and perpendicular to the GW propagation path. The dispersion curve (solid line) is the solution of equations (2.1) and (2.2). Symbols with error bars are dispersion determined from the seismogram using the technique described in the text. Contours represent the amplitude of the narrowband trace envelope at each frequency.

Figure 2.2: Three-dimensional seismic velocity model.

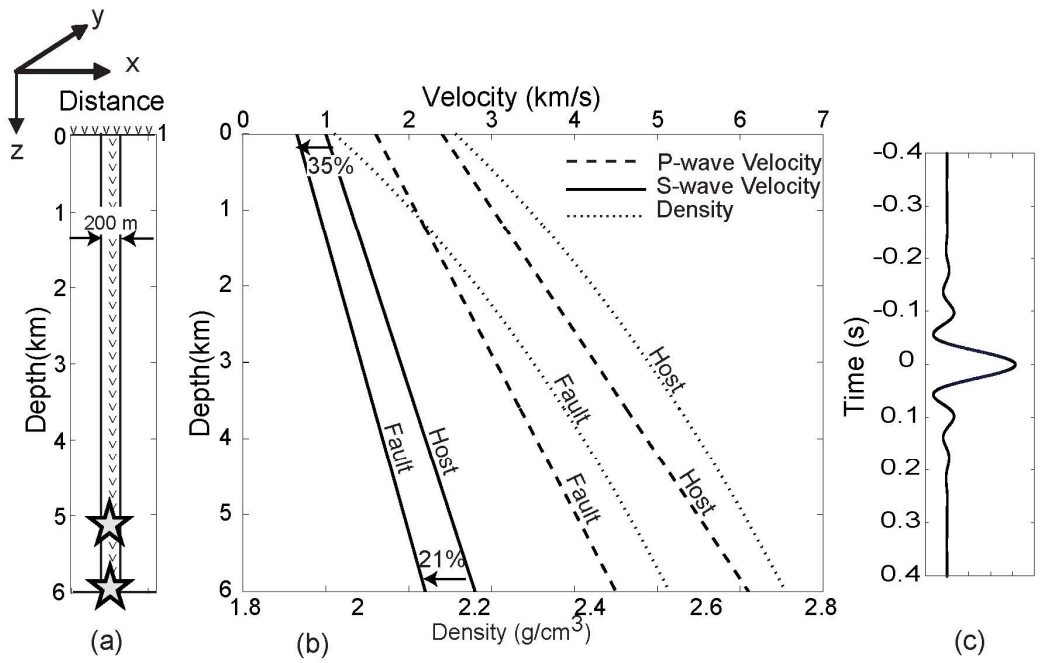

Three-dimensional seismic velocity model used to compute synthetic seismic data. (a) Vertical section across the fault model. The fault model is 2 km wide and homogeneous in the out-of-plane (y) direction. v's denote stations in the receiver arrays. Stars are seismic sources. (b) 1-D S-wave velocity (solid lines), P-wave velocity (dashed lines), and density (dotted lines) profiles in the host rock and fault. The S-wave velocity of the fault is reduced from the host rock by 35% at the surface and 21% at 6-km depth. (c) Source wavelet.

Figure 2.3: Analytic group velocity dispersion.

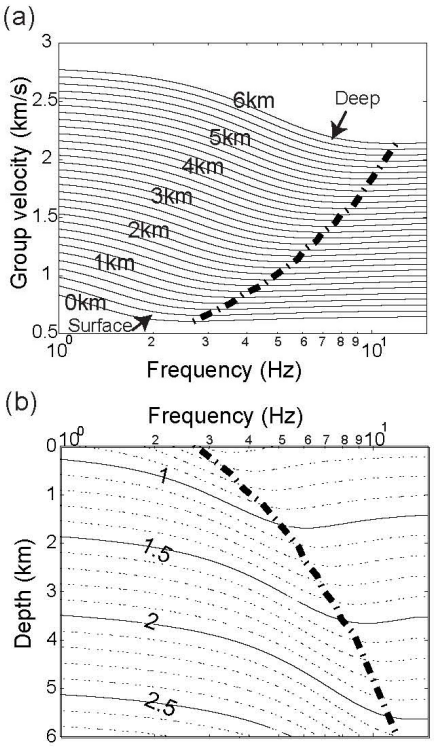

Adapted from Wu *et al*. (2008). (a) Analytic GW group velocity dispersion curves for the model of Figure 2.2 computed at different depths. (b) GW group velocity (in km/s) as a function of both depth and frequency. Horizontal slices through this image correspond to the lines in (a). The dash-dotted line in both (a) and (b) is drawn through the minimum in group velocity at each depth, indicating the dominant Airy-phase frequency.

Figure 2.4: y-component synthetic seismograms from the receiver arrays indicated in Figure 2.2a for a source at 6-km depth.

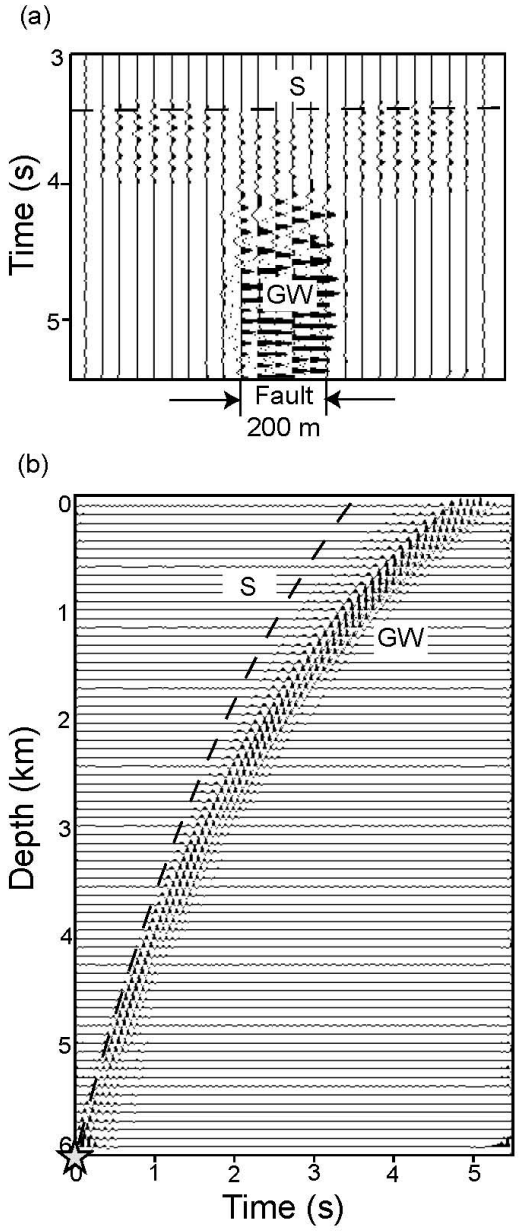

(a) Across-fault array at the surface. GWs are clearly visible. (b) Array within the waveguide along the direction of wave propagation. Analytic S-wave arrival times are displayed (dashed line) in both plots. Star denotes the seismic source.

Figure 2.5: Whole-path and interstation/earthquake velocity dispersion curves.

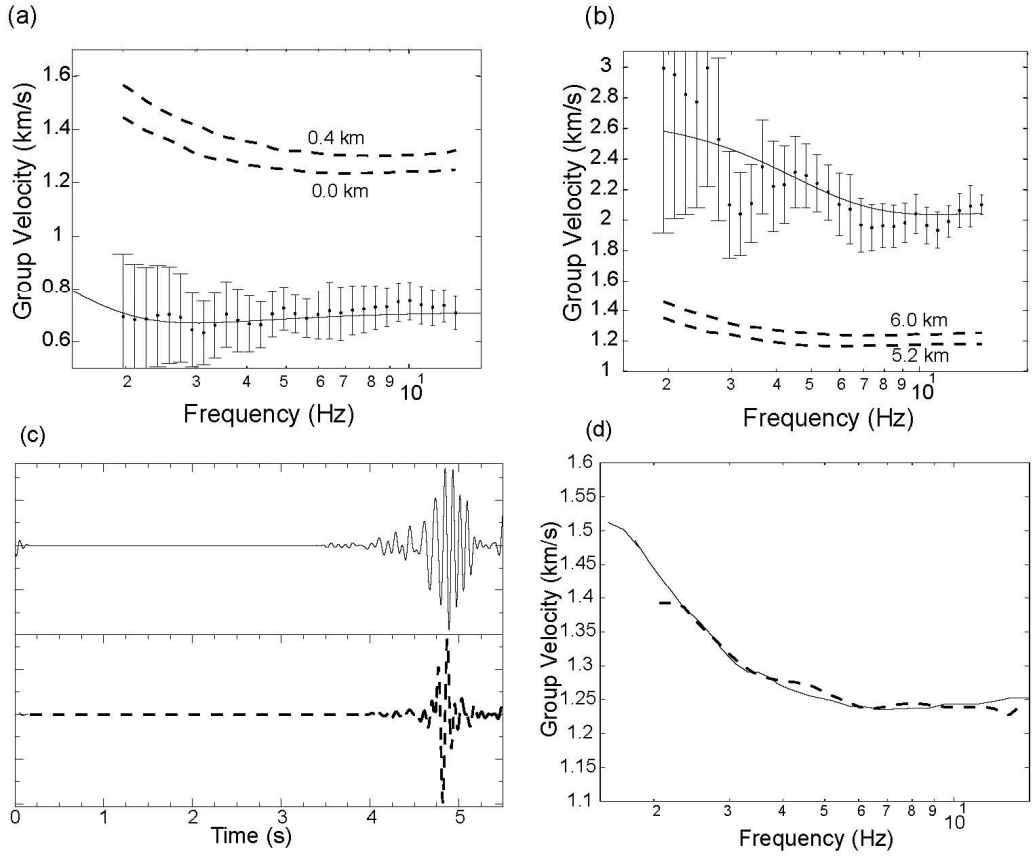

(a) Whole-path (dashed lines) and interstation (symbols with error bars) group velocity dispersion curves for receivers at 0 and 0.4-km depth and a source at 6 km depth (Figure 2.4b). Errors are estimated from the +/- 1dB ranges calculated for the two whole-path group velocities. The interstation velocity is consistent with the analytic group velocity at 0.2 km depth (solid line). (b) Whole-path and inter-earthquake dispersion curves for a station at 0.0 km depth and earthquakes at 5.2 and 6.0 km depth, plotted as in (a). The measured dispersion curve between the earthquakes is consistent with the analytic group velocity dispersion at 5.6 km depth. (c) Synthetic seismograms at the surface for a fault-parallel strike-slip double-couple source (top) and an obliquely orientated focal mechanism (bottom) at 6-km depth. (d) Dispersion curves for the seismograms in (c), suggesting negligible dependence upon focal mechanism for point sources.

Figure 2.6: Group travel times and interstation velocities.

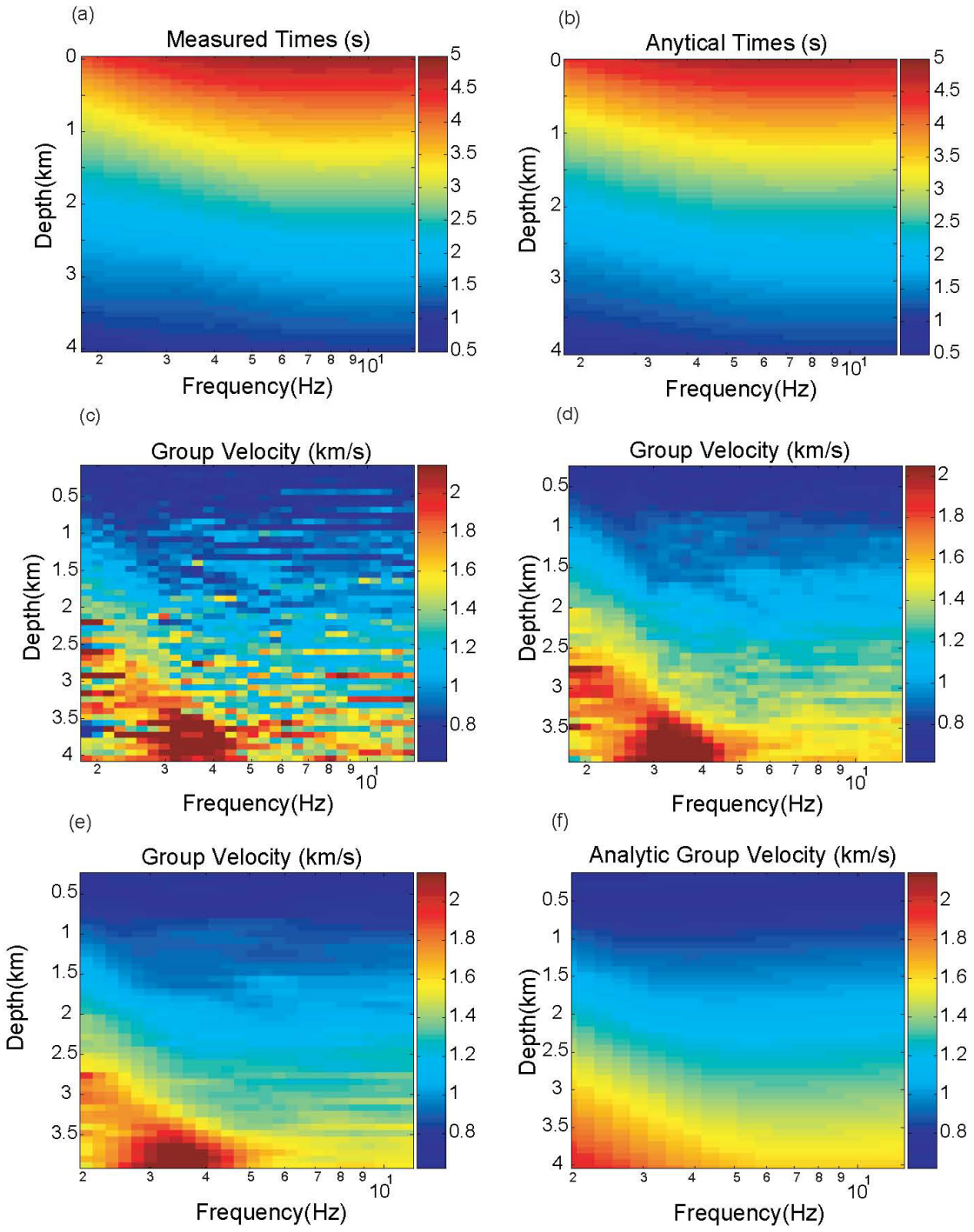

(a) Measured group arrival times for the seismograms of Figure 2.4b. (b) Analytic group travel times calculated by integrating from source to receiver using the group velocities in

Figure 2.3b. (c) Interval group velocities between every two stations 80-m apart, the vertical derivative of Figure 2.5a. (d) Interval group velocities between pairs of stations 400-m apart. (e) Group velocities determined by applying a 5×5-point (400 m by 1.4 dB) moving average filter to Figure 2.5a, then differentiating. (f) Analytic group velocities; color version of Figure 2.3b.

Figure 2.7: Map view and fault-plane cross-section of earthquakes recorded in the SAFOD borehole with clear GWs and group velocity dispersion.

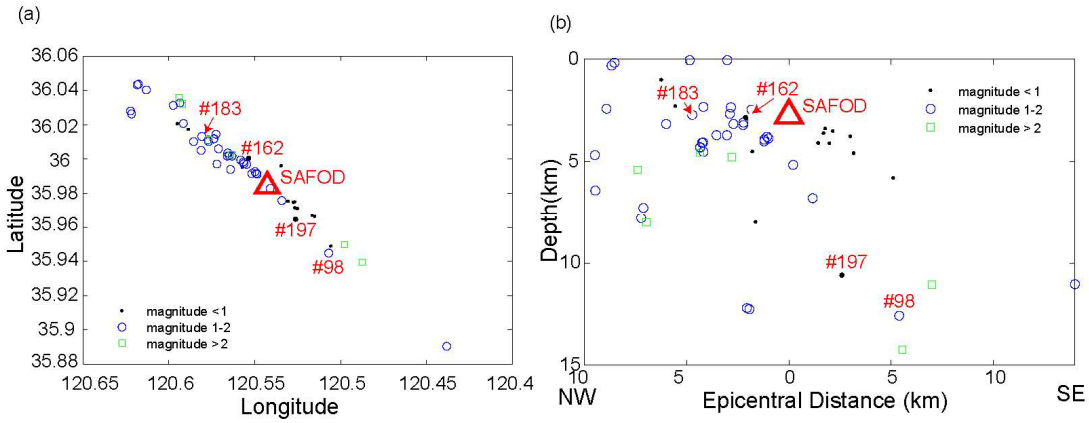

The SAFOD down-hole seismic station is the red triangle. Four events that will be discussed are labeled with event numbers.

Figure 2.8: Analysis of shallow SAFOD events.

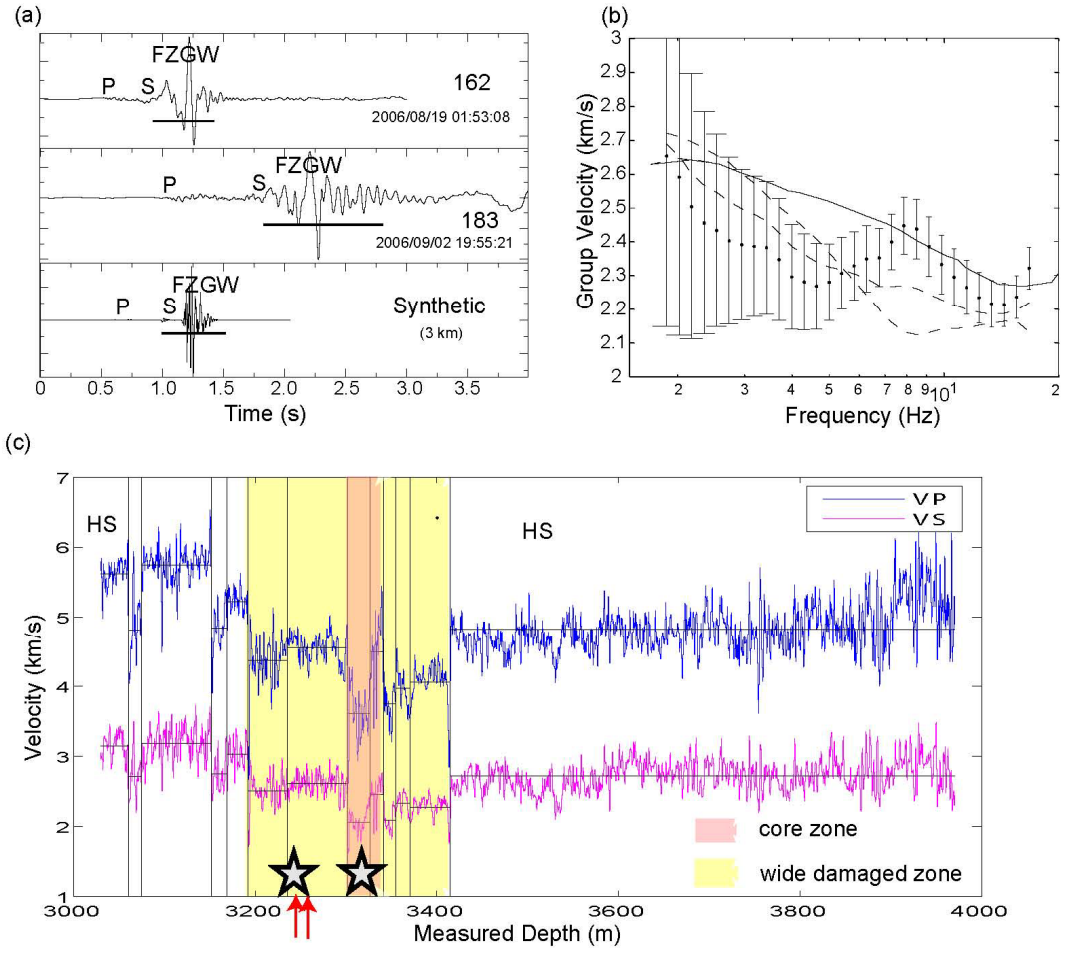

(a) Vertical-component seismograms for events #162 and #183 (Figure 2.7) and synthetic data based on the well log. (b) Dispersion curves for the two earthquakes (dashed lines), the inter-event dispersion (symbols with error bars), and synthetic seismic trace (solid line). (c) Seismic velocity well logs from SAFOD (Hickman *et al.* 2007). "Measured depth" is at a 540-600 angle from vertical and therefore oblique to an assumed vertical fault. A highly damaged core zone and a relatively less damaged low velocity zone are highlighted. A 13-layer simplification of the well logs (solid lines) is used to compute synthetic seismograms. Stars indicate synthetic earthquake locations and arrows indicate the real seismometer locations.

Figure 2.9: Analysis of deep SAFOD events.

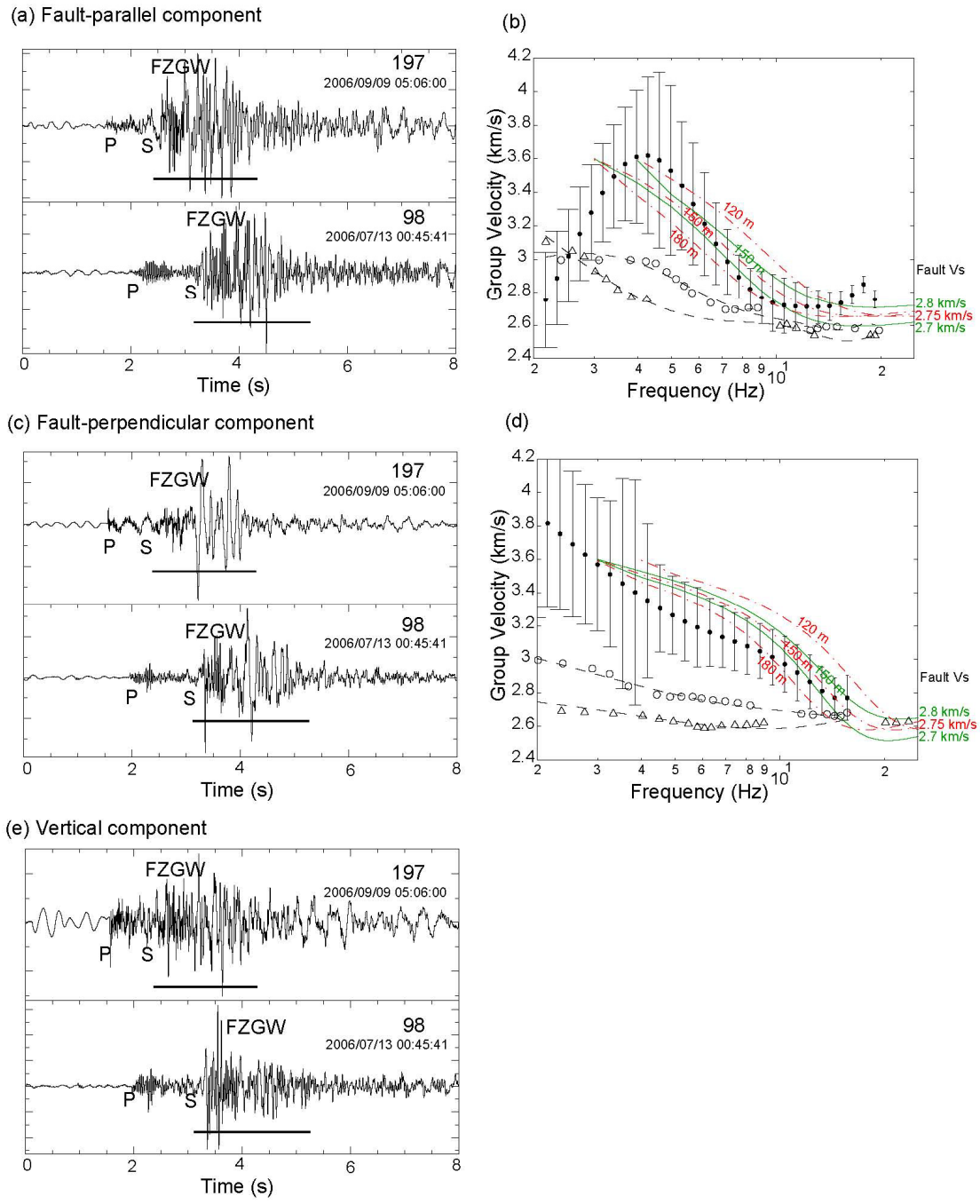

(a) Fault-parallel horizontal-component seismograms for events #197 and #98 (Figure 2.7). (b) Dispersive group velocity picks for the two earthquakes (triangle #197, circle #98), the low-order polynomial curve fit to these picks (dashed lines) and the inter-event

dispersion (symbols with error bars). Red lines are analytic **Love**-type wave dispersion curves for 120-m, 150-m and 180-m wide waveguide models with FZ S-wave velocity of 2.75 km/s. Green lines are analytic dispersion curves for a 150-m thick FZ waveguide with S-wave velocity of 2.8 and 2.7 km/s. (c) Fault-perpendicular horizontal-component seismograms for events #197 and #98. (d) Similar to (b). Colored lines are analytic **Rayliegh**-type wave dispersion curves for the same fault models as (b). (e) Vertical component seismograms for the same events.

Appendix: Fault-Zone Guided Wave Dispersion

Fault-Zone Model

The dispersion of guided waves (GW) in multilayered coal seams has been calculated by Rader *et al.* (1985) and Buchanan (1987). Using a similar method, we derived the guided wave dispersion in a homogeneous fault zone (FZ). The simple fault model contains one homogeneous low-velocity layer (FZ) bounded by two homogenous half spaces (Figure a1). The fault thickness is 2h. The subscript 1 refers to the fault and subscripts 2, 3 to the half spaces. Wave propagation is chosen to be in the x-z plane, with guided-wave propagation in the +z direction.

Pseudo-Love Wave

A pseudo-Love wave results from the interaction of S waves that have particle motion in the y direction. The displacement for a wave traveling in the +z direction in the fault is expressed as the sum of left-going (x-) and right-going (x+) waves:

$$u_{1y} = B_{1a} e^{i(\omega t - kz - k\eta_{\beta_1} x)} + B_{1b} e^{i(\omega t - kz + k\eta_{\beta_1} x)} \qquad \text{(a1)}$$

where $$\eta_{\beta_1} = \sqrt{c^2 / \beta_1^2 - 1}\,. \qquad \text{(a2)}$$

Here k denotes the wavenumber in the z direction, which is the FZGW propagation direction. The GW phase velocity c along the fault equals ω/k. The wavenumbers in the x direction are expressed as $k\eta_{\beta_1}$.

For each half space there is only one term for the evanescent wave outside the fault:

$$u_{2y} = B_2 e^{i(\omega t - kz - k\eta_{\beta_2} x)}$$

$$u_{3y} = B_3 e^{i(\omega t - kz + k\eta_{\beta_3} x)} \qquad \text{(a3)}$$

The solution must ensure that the GW energy does not propagate away from the fault; energy is post-critically reflected within the FZ. In the half space, the exponential terms $e^{-ik\eta_{\beta_2} x}$ and $e^{ik\eta_{\beta_3} x}$ must have negative real exponentials to ensure the displacement decays

as $x \rightarrow \pm\infty$. This condition occurs if the GW phase velocity c obeys $\beta_1 < c < \min(\beta_2, \beta_3)$, so

$$\eta_{\beta_2} = \sqrt{c^2/\beta_2^2 - 1} = -i\sqrt{1 - c^2/\beta_2^2} = -i\gamma_{\beta_2},$$

$$\eta_{\beta_3} = \sqrt{c^2/\beta_3^2 - 1} = -i\sqrt{1 - c^2/\beta_3^2} = -i\gamma_{\beta 3}. \quad \text{(a4)}$$

Here γ_{β_2} , γ_{β_3} terms are real numbers that are introduced to simplify the following expressions.

Both displacement and stress must be continuous along the boundary. Imposing these boundary conditions:

1) at $x = h$, $u_1 = u_2$ and $\tau_{yx}(u_1) = \tau_{yx}(u_2)$

$$B_{1a}e^{-ik\eta_{\beta_1}h} + B_{1b}e^{+ik\eta_{\beta_1}h} = B_2 e^{-ik\eta_{\beta_2}h} \quad \text{(a5)}$$

$$-ik\eta_{\beta_1}\mu_1(B_{1a}e^{-ik\eta_{\beta_1}h} - B_{1b}e^{+ik\eta_{\beta_1}h}) = -ik\eta_{\beta_2}\mu_2 B_2 e^{-ik\eta_{\beta_2}h} \quad \text{(a6)}$$

2) at $x = -h$, $u_1 = u_3$ and $\tau_{yx}(u_1) = \tau_{yx}(u_3)$

$$B_{1a}e^{+ik\eta_{\beta_1}h} + B_{1b}e^{-ik\eta_{\beta_1}h} = B_3 e^{-ik\eta_{\beta_3}h} \quad \text{(a7)}$$

$$-ik\eta_{\beta_1}\mu_1(B_{1a}e^{+ik\eta_{\beta_1}h} - B_{1b}e^{-ik\eta_{\beta_1}h}) = ik\eta_{\beta_3}\mu_3 B_3 e^{-ik\eta_{\beta_3}h} \quad \text{(a8)}$$

Linear equations a5 to a8 can be rewritten in the form:

$$\begin{bmatrix} \theta_{11} & \theta_{12} & \theta_{13} & 0 \\ \theta_{21} & \theta_{22} & \theta_{23} & 0 \\ \theta_{31} & \theta_{32} & 0 & \theta_{34} \\ \theta_{41} & \theta_{42} & 0 & \theta_{44} \end{bmatrix} \begin{bmatrix} B_{1a} \\ B_{1b} \\ B_2 \\ B_3 \end{bmatrix} = 0 \quad \text{(a9)}$$

In order to have nontrivial solutions for this system of equations, the determinant of the coefficient (θ_{ij}) matrix must equal zero. This gives the phase dispersion equation:

$$\begin{aligned} &e^{4ik\eta_{\beta_1}h}[\mu_1^2\eta_{\beta_1}^2 - i\mu_1\eta_{\beta_1}(\mu_2\gamma_{\beta_2} + \mu_3\gamma_{\beta_3}) - \mu_2\mu_3\gamma_{\beta_2}\gamma_{\beta_3}] \\ &= [\mu_1^2\eta_{\beta_1}^2 + i\mu_1\eta_{\beta_1}(\mu_2\gamma_{\beta_2} + \mu_3\gamma_{\beta_3}) - \mu_2\mu_3\gamma_{\beta_2}\gamma_{\beta_3}] \end{aligned} \quad \text{(a10)}$$

Equation (a10) can be simplified as:

$$\tan(\frac{2\pi f}{c}\eta_{\beta_1} 2h) = \frac{\mu_1\eta_{\beta_1}(\mu_2\gamma_{\beta_2} + \mu_3\gamma_{\beta_3})}{\mu_1^2\eta_{\beta_1}^2 - \mu_2\mu_3\gamma_{\beta_2}\gamma_{\beta_3}} \tag{a11}$$

This is the same result as Ben-Zion & Aki, (1990). If the two half spaces are the same materials, equation (a11) becomes equation (2.1).

Pseudo-Rayleigh Wave

The second type of GW is a pseudo-Rayleigh wave. It is a coupled P and S wave with particle displacements in the x and z directions. Lou *el at.* (1997) presented derivations of this wave dispersion in a three-layer waveguide model. We re-derive the dispersion and write the equations more completely.

The displacements in the three media (Figure a1) are (pg 105, Ben-Menahem & Singh 1981):

$$u_{1x} = [A_{1a}\eta_{\alpha_1}e^{-ik\eta_{\alpha_1}x} - A_{1b}\eta_{\alpha_1}e^{ik\eta_{\alpha_1}x} + B_{1a}e^{-ik\eta_{\beta_1}x} + B_{1b}e^{ik\eta_{\beta_1}x}]e^{i(\omega t-kz)}$$

$$u_{1z} = [A_{1a}e^{-ik\eta_{\alpha_1}x} + A_{1b}e^{ik\eta_{\alpha_1}x} - B_{1a}\eta_{\beta_1}e^{-ik\eta_{\beta_1}x} + B_{1b}\eta_{\beta_1}e^{ik\eta_{\beta_1}x}]e^{i(\omega t-kz)} \tag{a12}$$

$$u_{2x} = [-A_2 i\gamma_{\alpha_2}e^{-k\gamma_{\alpha_2}x} + B_2 e^{-k\gamma_{\beta_2}x}]e^{i(\omega t-kz)}$$

$$u_{2z} = [A_2 e^{-k\gamma_{\alpha_2}x} + B_2 i\gamma_{\beta_2}e^{-k\gamma_{\beta_2}x}]e^{i(\omega t-kz)} \tag{a13}$$

$$u_{3x} = [A_3 i\gamma_{\alpha_3}e^{k\gamma_{\alpha_3}x} + B_3 e^{k\gamma_{\beta_3}x}]e^{i(\omega t-kz)}$$

$$u_{3z} = [A_3 e^{k\gamma_{\alpha_3}x} - B_3 i\gamma_{\beta_3}e^{k\gamma_{\beta_3}x}]e^{i(\omega t-kz)} \tag{a14}$$

where, P-wave terms are defined similar to those for S waves:

$$\eta_\alpha = \sqrt{(c^2/\alpha^2 - 1)}\,, \qquad \gamma_\alpha = \sqrt{(1 - c^2/\alpha^2)} \tag{a15}$$

Boundary conditions are imposed as before:

1) at $x = h$, $u_1 = u_2$, $\tau_{zx}(u_1) = \tau_{zx}(u_2)$ and $\tau_{xx}(u_1) = \tau_{xx}(u_2)$

$$e^{-ik\eta_{\alpha_1}h}A_{1a} + e^{ik\eta_{\alpha_1}h}A_{1b} - \eta_{\beta_1}e^{-ik\eta_{\beta_1}h}B_{1a} + \eta_{\beta_1}e^{ik\eta_{\beta_1}h}B_{1b} = e^{-k\gamma_{\alpha_2}h}A_2 + i\gamma_{\beta_2}e^{-k\gamma_{\beta_2}h}B_2 \tag{a16}$$

$$\eta_{\alpha_1}e^{-ik\eta_{\alpha_1}h}A_{1a} - \eta_{\alpha_1}e^{ik\eta_{\alpha_1}h}A_{1b} + e^{-ik\eta_{\beta_1}h}B_{1a} + e^{ik\eta_{\beta_1}h}B_{1b} = -i\gamma_{\alpha_2}e^{-k\gamma_{\alpha_2}h}A_2 + e^{-k\gamma_{\beta_2}h}B_2 \tag{a17}$$

$$\mu_1[-2ik\eta_{\alpha_1}e^{-ik\eta_{\alpha_1}h}A_{1a}+2ik\eta_{\alpha_1}e^{ik\eta_{\alpha_1}h}A_{1b}+ik(\eta_{\beta_1}^2-1)e^{-ik\eta_{\beta_1}h}B_{1a}+ik(\eta_{\beta_1}^2-1)e^{ik\eta_{\beta_1}h}B_{1b}]$$
$$=\mu_2[-2k\gamma_{\alpha_2}e^{-k\gamma_{\alpha_2}h}A_2-ik(\gamma_{\beta_2}^2+1)e^{-k\gamma_{\beta_2}h}B_2] \quad \text{(a18)}$$

$$-ik[\lambda_1(1+\eta_{\alpha_1}^2)+2\mu_1\eta_{\alpha_1}^2]e^{-ik\eta_{\alpha_1}h}A_{1a}-ik[\lambda_1(1+\eta_{\alpha_1}^2)+2\mu_1\eta_{\alpha_1}^2]e^{ik\eta_{\alpha_1}h}A_{1b}-2ik\mu_1\eta_{\beta_1}e^{-ik\eta_{\beta_1}h}B_{1a}$$
$$+2ik\mu_1\eta_{\beta_1}e^{ik\eta_{\beta_1}h}B_{1b}=ik[(\gamma_{\alpha_2}^2-1)\lambda_2+2\mu_2\gamma_{\alpha_2}^2]e^{-k\gamma_{\alpha_2}h}A_2-2\mu_2\gamma_{\beta_2}ke^{-k\gamma_{\beta_2}h}B_2 \quad \text{(a19)}$$

2) at $x = -h$, $u_1=u_3$, $\tau_{zx}(u_1)=\tau_{zx}(u_3)$ and $\tau_{xx}(u_1)=\tau_{xx}(u_3)$

$$e^{ik\eta_{\alpha_1}h}A_{1a}+e^{-ik\eta_{\alpha_1}h}A_{1b}-\eta_{\beta_1}e^{ik\eta_{\beta_1}h}B_{1a}+\eta_{\beta_1}e^{-ik\eta_{\beta_1}h}B_{1b}=e^{-k\gamma_{\alpha_3}h}A_3-i\gamma_{\beta_3}e^{-k\gamma_{\beta_3}h}B_3 \quad \text{(a20)}$$

$$\eta_{\alpha_1}e^{ik\eta_{\alpha_1}h}A_{1a}-\eta_{\alpha_1}e^{-ik\eta_{\alpha_1}h}A_{1b}+e^{ik\eta_{\beta_1}h}B_{1a}+e^{-ik\eta_{\beta_1}h}B_{1b}=i\gamma_{\alpha_3}e^{-k\gamma_{\alpha_3}h}A_3+e^{-k\gamma_{\beta_3}h}B_3 \quad \text{(a21)}$$

$$\mu_1[-2ik\eta_{\alpha_1}e^{ik\eta_{\alpha_1}h}A_{1a}+2ik\eta_{\alpha_1}e^{-ik\eta_{\alpha_1}h}A_{1b}+ik(\eta_{\beta_1}^2-1)e^{ik\eta_{\beta_1}h}B_{1a}+ik(\eta_{\beta_1}^2-1)e^{-ik\eta_{\beta_1}h}B_{1b}]$$
$$=\mu_3[2k\gamma_{\alpha_3}e^{-k\gamma_{\alpha_3}h}A_3-ik(\gamma_{\beta_3}^2+1)e^{-k\gamma_{\beta_3}h}B_3] \quad \text{(a22)}$$

$$-ik[\lambda_1(1+\eta_{\alpha_1}^2)+2\mu_1\eta_{\alpha_1}^2]e^{ik\eta_{\alpha_1}h}A_{1a}-ik[\lambda_1(1+\eta_{\alpha_1}^2)+2\mu_1\eta_{\alpha_1}^2]e^{-ik\eta_{\alpha_1}h}A_{1b}-2ik\mu_1\eta_{\beta_1}e^{ik\eta_{\beta_1}h}B_{1a}$$
$$+2ik\mu_1\eta_{\beta_1}e^{-ik\eta_{\beta_1}h}B_{1b}=ik[(\gamma_{\alpha_3}^2-1)\lambda_3+2\mu_3\gamma_{\alpha_3}^2]e^{-k\gamma_{\alpha_3}h}A_3+2\mu_3\gamma_{\beta_3}ke^{-k\gamma_{\beta_3}h}B_3 \quad \text{(a23)}$$

Equations (a16) to (a23) yield a set of 8 linear equations with 8 unknowns, $A_{1a}, A_{1b}, B_{1a}, B_{1b}, A_2, A_3, B_2,$ and B_3. For consistency of the system of equations similar to equation (a9), the determinant of the coefficient matrix equals zero. This leads to the phase dispersion equation. Numerical solutions for this dispersion equation can be easily determined.

References:

Ben-Menahem, A. & Singh, S. J., 1981. Seismic Waves and Sources. *Springer-Verlag New York Heidelberg Berlin,* 1108 pp.

Ben-Zion, Y. & Aki, K., 1990. Seismic Radiation from an Sh Line Source in a Laterally Heterogeneous Planar Fault Zone. *Bulletin of the Seismological Society of America,* **80,** 971-994.

Buchanan, D. J., 1987. Dispersion Calculations for Sh and P-Sv Waves in Multilayered Coal Seams. *Geophysical Prospecting,* **35,** 62-70.

Lou, M., Rial, J. A. & Malin, P. E., 1997. Modeling fault-zone guided waves of microearthquakes in a geothermal reservoir. *Geophysics,* **62,** 1278-1284.

Rader, D., Schott, W., Dresen, L. & Ruter, H., 1985. Calculation of Dispersion-Curves and Amplitude-Depth Distributions of Love Channel Waves in Horizontally-Layered Media. *Geophysical Prospecting,* **33,** 800-816.

Figure a1: A homogeneous fault zone model.

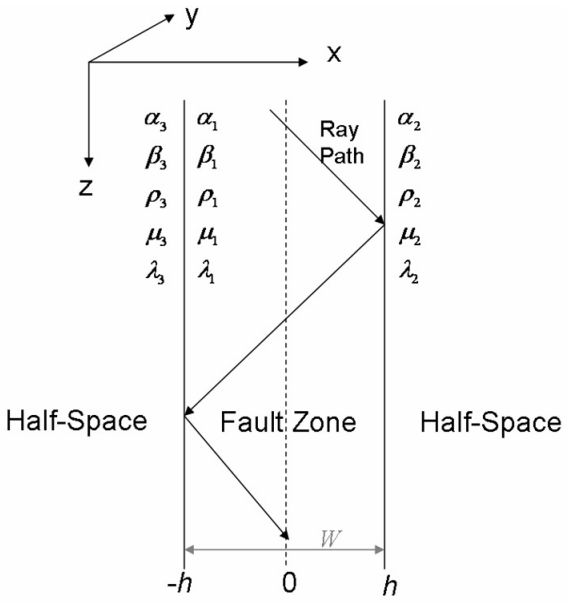

α, β and ρ are the P-, S-wave velocity and density respectively. μ is shear modulus and λ is the Lame coefficient. Lines with arrows are the S-wave ray paths that form the FZGW.

Chapter 3

Refraction of Fault-Zone Guided Seismic Waves

Summary

Finite-difference synthetic seismograms were computed for a receiver array along and within a low-velocity fault damage zone, analogous to a body-wave refraction survey. The synthetic data demonstrate that dispersive fault-zone guided waves are refracted by an increase in both fault-zone and crustal velocity with depth. Refraction of the guided waves allows the surface array to record waves that sample the deep fault zone. At each frequency, the observed group arrival times can be inverted for a 1-D or 2-D model of group velocity within the fault plane. The synthetic seismograms recorded at surface were successfully used to derive the fault zone properties in the subsurface. Using multiple sources and receivers, this method can be used to derive 3-D fault-zone structure to seismogenic depths, mapping variations both along strike and in depth.

Keywords: fault zone, guided waves, refraction, dispersion, velocity imaging.

3.1 Introduction

Knowledge of the internal structure and physical properties of fault zones (FZs) is essential to understand the mechanics of faulting and earthquakes. Fracturing, brecciation, re-mineralization, and fluids in FZs create a damage zone with low seismic velocity (Li *et al.* 2001; Ben-Zion & Sammis 2003; Gettemy *et al.* 2004). Fault-zone guided waves (FZGWs), seismic waves trapped in the FZ by internal reflection and refraction, provide a good method to measure FZ structure. FZGWs were originally observed by Aki and coworkers (Leary *et al.* 1985; Ben-Zion & Aki 1990; Li *et al.* 1990) in controlled-source surface to borehole studies and later in receivers near FZs from local earthquakes.

In the past two decades, both theoretical and experimental studies have reported observations of FZGWs and interpreted their characteristics in terms of FZ structure.

Guided wave (GW) properties depend upon the fault geometry, velocities and attenuation within the fault and the source location & mechanism (Li & Vidale 1996; Ben-Zion 1998; Igel *et al.* 2002; Jahnke *et al.* 2002; Fohrmann *et al.* 2004; Wu *et al.* 2008). Using numerical waveform modeling of FZGWs, the velocity structures of several major FZs have been mapped. These analyses are highly non-unique due to the number of trade-offs among the fault properties (Ben-Zion *et al.* 2003; Li *et al.* 2004; Lewis *et al.* 2005). This has resulted in some debate about the structure and even existence of a waveguide as a function of depth (Ben-Zion & Sammis 2003; Wu *et al.* 2008). The ability to determine FZ variation along the fault plane from FZGWs is limited by the survey recording geometry and the analysis methods used to date. We propose in this report a new survey design and analysis procedure.

Seismic velocity almost always increases with depth in the upper crust due to a combination of lithologic layering, the pressure-induced closure of pores and fractures, and metamorphism (Christensen & Mooney 1995). This increase in velocity is the basis of body-wave refraction exploration methods. Refracted energy paths include both critical refraction at discontinuities, also called “head waves”, and continuous refraction in a continuous velocity gradient, also called “turning rays”.

Seismic velocity within the low-velocity FZ, like the surrounding rocks, also increases with depth due to the closure of fractures and pores as well as metamorphism. Wu *et al.* (2008) show that this increase in velocity causes the dispersive GW phase velocity, group velocity, and trapped frequencies to increase with depth. As the GW propagates, it is sensitive only to the local FZ properties. The GW group travel time at each frequency can be computed by integration of the local group velocities along the energy path (Wu *et al.* 2008). If the FZ properties vary along the fault plane, the GWs should refract within the fault. The expected vertical velocity gradient allows the application of refraction methods to GWs to investigate FZ structure in the subsurface.

Most GW studies used a single station or a small local array to record a small number of isolated earthquakes or controlled sources. None of these studies have had sufficient data to allow a study of GW propagation paths and their potential to map out subsurface

structure. Korneev *et al.* (2003) performed GW 2-D amplitude tomography to derive attenuation variation in the plane of the San Andreas Fault. With only 2 stations, straight ray paths were used to assign the attenuation to the correct location. Vidale and Li (2003) include a figure with curved rays to illustrate that GWs from surface sources at different distances from the station array sample different depth within the FZ, but they could not quantify the depth structure. We are not aware of any other study using refraction or tomography of GWs that addresses variation of FZ structure within the plane of the fault.

Surface waves in Earth's low-velocity layers are another type of GW. One method to derive regional S-wave velocity structures is to deploy an array of stations to record surface waves from teleseismics. The relative phase or group arrival times for each earthquake are measured at each frequency, and then for each frequency data from multiple earthquakes are inverted for the phase or group velocity as a function of 2-D map position within the array (Forsyth *et al.* 1998; Friederich 1998; Pollitz 1999; Li *et al.* 2003). This is analogous to 2-D body wave tomography along the waveguide-parallel surface layer. The single-frequency 2-D tomography is repeated for each frequency, resulting in a series of group or phase velocity maps. Velocity dispersion at each map location is then inverted for S-wave velocity as a function of depth. While more recent surface-wave analyses utilize full 3-D inversion kernels (Zhou *et al.* 2004; Yoshizawa & Kennett 2005; Lebedev & van der Hilst 2008), useful images have been produced from single-frequency waveguide-parallel 2-D tomography followed by 1-D waveguide-perpendicular inversion of dispersion. We propose similar methods to study FZGWs.

In this paper, numerical modeling is used to generate synthetic GWs in a vertical FZ model that has velocity continuously increasing with depth. A refraction survey along the fault strike within the FZ is simulated. The results show that FZGWs are turned or refracted just like body waves. Refracted GW arrival times from the surface source and surface receiver array are used to obtain the subsurface FZ velocity structure. A method is described to invert for 3-D subsurface structure of the FZ from surface GW experiment.

3.2 Fault Model and Survey Design

Synthetic seismograms were computed in a three-dimensional (3-D) model consisting of a 200-m wide vertical FZ (Figure 3.1). Velocity increases linearly with depth both outside and inside the FZ, with the velocity in the fault 35% slower than the surrounding crust at the surface to 22% slower at 5km depth (Table 3.1). The model is homogeneous along fault strike. This model is modified from the results of Li *et al*. (2004) for the San Andreas Fault at Parkfield.

An explosive source was fired at the surface off-center within the FZ. Several receiver arrays were deployed across the fault at the surface, which is the geometry most commonly used in FZGW surveys. In addition, a surface receiver array is deployed parallel to and within the fault, extending away from the source. This is the geometry of a refraction survey.

Seismic waveforms were computed using a 3-D elastic finite-difference method (Kelly *et al.* 1976) with the parameters of Table 3.1. An absorbing boundary condition (the Perfect Matched Layer of Chew & Liu 1996) was used to reduce reflections from the model surfaces. An extrapolated buffer zone around the model and the absorbing boundary conditions prevent the simulation of surface waves. The impulsive source wavelet is band-limited to 0-15 Hz to avoid numerical aliasing. Numerical tests with homogeneous fault models were used to test the FD algorithm and parameters.

3.3 Synthetic Seismograms

The synthetic seismograms (Figure 3.2) contain strong ground shaking that arrives later than the S waves. In the across-fault arrays, these arrivals are strong within the FZ but decrease rapidly outside the FZ, indicating FZGWs. The FZGWs are dispersive, with low frequencies arriving earlier than higher frequencies. Dispersion is also indicated on the along-fault array by the higher apparent phase velocity (slope of the wavelet peak in the seismic section) than the apparent group velocity (slope of the energy packet).

The FZGWs are strongly curved in the seismic section for the along-fault array,

indicating an increase in apparent wave speed at longer offsets. The GWs are not traveling horizontally parallel to the surface at a constant velocity (dashed lines, Figure 3.2). Body waves in the crust outside the fault are refracted or turned by the increase in velocity with depth. Body-waves that travel further turn at greater depth and sample higher velocity, resulting in travel-time curves (black and grey lines, Figure 3.2) with a shape similar to the FZGWs. The GWs must also be refracted or turned due to the increase in velocity with depth.

FZ-guided P-waves are also observed in the synthetic data (Figure 3.2). This phase is dispersive and has a clear Airy phase that arrives between the P and S-arrivals. Guided P-waves have been observed in the SAFOD borehole station in the San Andeans Fault (Li & Malin 2008). A mathematical relationship between this phase and the FZ properties has not yet been derived, however it may provide insights into FZ structure in the future.

3.4 Guided Waves in an Inhomogeneous Fault

3.4.1 Waves and Particle Motions

Surface Rayleigh and Love waves in Earth's lower-velocity surface layers are also GWs. The wave equation for FZGWs is solved similar to the solution for surface waves, but with different boundary conditions, with the free-surface replaced by a half-space. This results in pseudo-Rayleigh and pseudo-Love FZ waves that are similar to the surface waves (Ben-Zion & Aki 1990; Igel *et al.* 1997; Lou *et al.* 1997; Wu *et al.* in preparation). Pseudo-Rayleigh FZGWs are coupled P and SN waves, where N is normal (perpendicular) to the waveguide. Particle motion is in an ellipse oriented perpendicular to the waveguide and parallel to the direction of wave propagation (Figure 3.3). Pseudo-Love FZGWs are shear waves with particle displacement parallel to the waveguide and perpendicular to the direction of wave propagation (Figure 3.3).

An explosive source was used in the numerical simulation, which produces strong pseudo-Rayleigh FZGWs and weak pseudo-Love waves. Due to the velocity gradient, the refracted FZGWs observed at the surface arrive at an angle between vertical and horizontal. Pseudo-Love waves therefore appear in both the y and z (fault-strike and

vertical) component synthetic seismograms, while pseudo-Rayleigh motions exist in all three components (Figure 3.3). Consequently, the x-component (fault-perpendicular) seismograms record only the pseudo-Rayleigh waves. The remainder of this paper will focus on analyzing the pseudo-Rayleigh waves.

3.4.2 Dispersive Velocities and Travel Times

Analytic equations exist to compute the dispersive phase and group velocities of pseudo-Rayleigh and pseudo-Love FZGWs in a homogeneous fault (Ben-Zion & Aki 1990; Lou *et al.* 1997; Wu *et al.* in preparation). GW velocity depends primarily on the S-wave velocities inside and outside the fault and the fault width, with weaker dependence on the P-wave velocities and densities. At high frequency, the phase and group velocities approach the S-wave velocity of the FZ. At very low frequency, the wavelengths are much larger than the fault width and the phase and group velocities approach the velocity of the crust outside the fault. A minimum in group velocity, producing a strong Airy phase, corresponds to wavelengths on the order to the fault width.

An increase in seismic velocities with depth causes the dominant frequency of the GWs to increase with depth (Wu *et al.* 2008). Higher-frequency GWs are more efficiently trapped at greater depth while lower-frequency GWs are efficiently trapped near the surface. Assuming the fault is locally homogenous at each depth, the group velocity dispersion curves can be computed at each local depth in the fault model (Figure 3.4a). Wu *et al.* (2008) showed that for straight paths, the group travel time at each frequency can be computed by integrating this local group velocity along the path.

At each frequency, the GW group velocity can be plotted as a function of depth (Figure 3.4b). This one-dimensional group velocity model can be used to compute refraction or turning of the GW at that frequency. Similar to body waves, ray paths can be computed at each frequency, such as those for 4 Hz shown in Figure 3.1. Travel times for different frequencies can be computed by integration along the ray paths (Figure 3.4c). Lower-frequency GWs (2 Hz) arrive earlier than higher-frequency GWs (4 & 8 Hz).

However, this pattern is not perfect, because of the local minimum in the group velocity dispersion that occurs at a different depth and a different source-receiver distance for different frequencies. This concept of using single-frequency rays to predict group travel times is tested with the synthetic data.

3.5 Travel-Time Analysis of Observed Guided Waves

Group travel times at each frequency can be measured from seismograms using the frequency-time analysis of Snoke and James (1997). GWs from the along-fault x-component seismic array (Figure 3.2) are filtered by a narrow-band-pass zero-phase Gaussian filter at a range of center frequencies. The envelope of each trace is computed at each frequency (Figure 3.5). The maximum of the trace envelope is automatically picked to determine the group arrival time of the GWs at that frequency.

The maxima of the narrow-band trace envelopes (circles on Figure 3.5; symbols with error bars on Figure 3.4c) match the analytic travel times of Figure 3.4 (lines, Figures 3.4c and 3.5). The GW travel times obtained from the synthetic seismograms are consistent with 2-D ray-tracing in the single-frequency velocity model built from the analytic local group velocities. For each frequency, the analysis needs to be treated separately.

Group travel times were systematically obtained as a function of frequency from the x-component seismograms on the along-fault array (Figure 3.6a). At each selected frequency, the time-distance curve (horizontal slice through Figure 3.6b) was inverted for a 1-D group velocity model as a function of depth. Frequencies were selected based on the logarithm scale. The travel times were first smoothed in distance and in frequency by applying a 3×3 (1200 m by 1.8 db) 2-D moving average filter to Figure 3.6b. The 1-D inversion for group velocity assumes that the model consists of many thin layers of constant group velocity. Each travel time pick, working from short shot-receiver distance outward, was inverted for the velocity and thickness of the next deeper layer. Repeating the 1-D inversion at each frequency produced the group velocity dispersion at every depth (Figure 3.6c).

The group velocity derived from the synthetic data (Figure 3.6c) matches the analytic local group velocity calculated directly from the velocity model (Figure 3.6d). Local group velocity dispersion at any depth can be extracted from Figure 3.6c and modeled to derive local FZ structure. As an example, the observed GW group dispersion curve at 3 km depth (dots, Figure 3.6e) matches well the analytic dispersion curve for the true 200-m wide fault with an S velocity of 1.43 km/s at 3 km depth (black line). Forward modeling of analytic dispersion curves for similar faults (red and blue lines) indicates that the fault width and velocity are well constrained by the data to within 10% of their true values.

3.6 Conclusions and Discussion

The spatially varying internal structure and physical properties of FZs play a crucial role in the dynamic behavior of faults. Body-wave tomography is not capable of resolving FZ structure at seismogenic depth at the 10's to few 100 m scale. Seismic FZGWs are one of the best tools for imaging internal FZ structure. However, GW studies to date have only modeled very simple depth and along-strike variation of the FZ, and these models have been the subject of debate about non-uniqueness.

Unlike traditional GW surveys that deploy a receiver array across the fault, we propose a receiver array along the fault inside the FZ, analogous to a body-wave refraction survey. The synthetic seismic data of Figures 3.2, 3.5, and 3.6 verify that FZGWs are refracted by an increase in velocity with depth. Such an increase in velocity is ubiquitous in the upper crust. Refraction causes waves to sample the fault below a seismic source and be recorded at the surface. The synthetic data from a surface seismic survey were successfully used to derive subsurface properties of the FZ to several km depth.

The depth of penetration of refracted FZGWs will be similar to that of body waves in the local crust. In continental crust, seismic refraction methods with 10-100 km source-receiver distances record refracted or turning body waves (Pg and Sg phases) that sample the crust to a maximum depth of 5-15 km, depending on local geology. A stronger

velocity gradient with depth produces deeper ray coverage. The body-wave velocity in the FZ should increase with depth similar to that in the surrounding crust due to the pressure-induced closure of fractures and pores. Figure 3.4b shows that the vertical gradient of the GW group velocity mimics that of the FZ and crust. GWs have a slightly higher velocity gradient at the depth that each frequency transitions from guided (slow) at shallow depth to near-body wave at greater depth. Variations in FZ thickness or percent velocity contrast will also affect the GW velocity. The proposed method should produce guided rays that turn deep enough to illuminate FZ structure at seismogenic depth.

Combining the method of body wave tomography with GW dispersion, a new methodology of inverting FZGWs for FZ structures is proposed. This method requires deploying a GW refraction survey with a source or sources and a receiver array within and along the waveguide (Figure 3.1a). The work flow is demonstrated in Figure 3.7 for a simple 2-D FZ model.

1) At each receiver, determine the GW group travel time as a function of frequency.
2) Sort these travel times to obtain times as a function of source-receiver distance at selected frequencies.
3) At each frequency, apply 1-D travel-time inversion to obtain the GW group velocity as a function of depth. If multiple shots were recorded, perform 2-D travel-time tomography at each frequency to obtain group velocity as a function of depth and strike.
4) Sort these group velocities to obtain the local dispersion curve at each point in depth on the fault plane (or in depth and along strike).
5) For surface waves, the local dispersion curve is commonly used to invert for the local S-wave velocity structure as a function of depth (Woods & Okal 1996; Snoke & James 1997; Friederich 1998). A similar inversion could be performed for the local across-fault structure using GW dispersion curve at each point on the fault plane. For a single-layer fault model, inversion can easily be performed by grid searching (e.g., Figure 3.6e), allowing investigation of the trade-off between parameters. Inversion for multi-layer fault parameters is probably more non-unique than for surface waves due to the two-sided nature of the FZ

waveguide. Velocities on two sides of the fault will be constrained by 3-D body-wave tomography at the same location.

6) Finally, sort these model parameters to obtain the 2-D or 3-D FZ structure.

The proposed new methodology using the refraction of dispersive FZGWs provides constraints on FZ structure as a function of depth and distance along strike. The resulting fault-plane map of FZ velocity and thickness can be correlated with other observations, such as seismicity or geodetic slip in the fault plane, to better understand dynamic fault behavior and earthquakes.

Acknowledgments

We thank the Advanced Research Computing (ARC) center at Virginia Tech for providing computational facilities.

References

Ben-Zion, Y. & Aki, K., 1990. Seismic Radiation from an Sh Line Source in a Laterally Heterogeneous Planar Fault Zone. Bulletin of the Seismological Society of America, 80, 971-994.

Ben-Zion, Y., 1998. Properties of seismic fault zone waves and their utility for imaging low-velocity structures. Journal of Geophysical Research-Solid Earth, 103, 12567-12585.

Ben-Zion, Y., Peng, Z. G., Okaya, D., Seeber, L., Armbruster, J. G., Ozer, N., Michael, A. J., Baris, S., Aktar, M., Kuwahara, Y. & Ito, H., 2003. A shallow fault-zone structure illuminated by trapped waves in the Karadere-Duzce branch of the North Anatolian Fault, western Turkey. Geophysical Journal International, 152, 699-717.

Ben-Zion, Y. & Sammis, C. G., 2003. Characterization of fault zones. Pure and Applied Geophysics, 160, 677-715.

Chew, W. C. & Liu, Q. H., 1996. Perfectly matched layers for elastodynamics: A new absorbing boundary condition. Journal of Computational Acoustics, 4, 341-359.

Christensen, M. I. & Mooney, W. D., 1995. Seismic Velocity Structure and Composition of the Continental-Crust - a Global View. Journal of Geophysical Research-Solid Earth, 100, 9761-9788.

Fohrmann, M., Igel, H., Jahnke, G. & Ben-Zion, Y., 2004. Guided waves from sources

outside faults: An indication for shallow fault zone structure? Pure and Applied Geophysics, 161, 2125-2137.

Forsyth, D. W., Webb, S. C., Dorman, L. M. & Shen, Y., 1998. Phase velocities of Rayleigh waves in the MELT experiment on the East Pacific Rise. Science, 280, 1235-1238.

Friederich, W., 1998. Wave-theoretical inversion of teleseismic surface waves in a regional network: phase-velocity maps and a three-dimensional upper-mantle shear-wave-velocity model for southern Germany. Geophysical Journal International, 132, 203-225.

Gettemy, G. L., Tobin, H. J., Hole, J. A. & Sayed, A. Y., 2004. Multi-scale compressional wave velocity structure of the San Gregorio Fault zone. Geophysical Research Letters, 31, doi:10.1029/2003GL018826.

Igel, H., Ben-Zion, Y. & Leary, P. C., 1997. Simulation of SH- and P-SV-wave propagation in fault zones. Geophysical Journal International, 128, 533-546.

Igel, H., Jahnke, G. & Ben-Zion, Y., 2002. Numerical simulation of fault zone guided waves: Accuracy and 3-D effects. Pure and Applied Geophysics, 159, 2067-2083.

Jahnke, G., Igel, H. & Ben-Zion, Y., 2002. Three-dimensional calculations of fault-zone-guided waves in various irregular structures. Geophysical Journal International, 151, 416-426.

Kelly, K. R., Ward, R. W., Treitel, S. & Alford, R. M., 1976. Synthetic Seismograms - Finite-Difference Approach. Geophysics, 41, 2-27.

Korneev, V. A., Nadeau, R. M. & McEvilly, T. V., 2003. Seismological studies at Parkfield IX: Fault-zone imaging using guided wave attenuation. Bulletin of the Seismological Society of America, 93, 1415-1426.

Leary, P. C., Li, Y. G. & Aki, K., 1985. Borehole observations of fault zone trapped waves,Oroville, CA. EOS, Trans. Am. Geophys. Un., 66, 976.

Lebedev, S. & van der Hilst, R. D., 2008. Global upper-mantle tomography with the automated multimode inversion of surface and S-wave forms. Geophysical Journal International, 173, 505-518.

Lewis, M. A., Peng, Z., Ben-Zion, Y. & Vernon, F. L., 2005. Shallow seismic trapping structure in the San Jacinto fault zone near Anza, California. Geophysical Journal International, 162, 867-881.

Li, A. B., Forsyth, D. W. & Fischer, K. M., 2003. Shear velocity structure and azimuthal anisotropy beneath eastern North America from Rayleigh wave inversion. Journal of

Geophysical Research-Solid Earth, 108, doi:10.1029/2002JB002259.

Li, Y. G., Leary, P. C., Aki, K. & Malin, P. E., 1990. Seismic trapped modes in the Oroville and San Andears fault zones. Science, 249, 763-766.

Li, Y. G. & Vidale, J. E., 1996. Low-velocity fault-zone guided waves: Numerical investigations of trapping efficiency. Bulletin of the Seismological Society of America, 86, 371-378.

Li, Y. G., Chester, F. M. & Vidale, J. E., 2001. Shallow seismic profiling of the exhumed Punchbowl fault zone, southern California. Bulletin of the Seismological Society of America, 91, 1820-1830.

Li, Y. G., Vidale, J. E. & Cochran, E. S., 2004. Low-velocity damaged structure of the San Andreas Fault at Parkfield from fault zone trapped waves. Geophysical Research Letters, 31, 2165, doi:10.1029/2001JB001456.

Li, Y. G. & Malin, P. E., 2008. San Andreas Fault damage at SAFOD viewed with fault-guided waves. Geophysical Research Letters, 35, doi:10.1029/2007GL032924.

Lou, M., Rial, J. A. & Malin, P. E., 1997. Modeling fault-zone guided waves of microearthquakes in a geothermal reservoir. Geophysics, 62, 1278-1284.

Pollitz, F. F., 1999. Regional velocity structure in northern California from inversion of scattered seismic surface waves. Journal of Geophysical Research-Solid Earth, 104, 15043-15072.

Snoke, J. A. & James, D. E., 1997. Lithospheric structure of the Chaco and Parana Basins of South America from surface-wave inversion. Journal of Geophysical Research-Solid Earth, 102, 2939-2951.

Vidale, J. E. & Li, Y. G., 2003. Damage to the shallow Landers fault from the nearby Hector Mine earthquake. Nature, 421, 524-526.

Woods, M. T. & Okal, E. A., 1996. Rayleigh-wave dispersion along the Hawaiian Swell: A test of lithospheric thinning by thermal rejuvenation at a hotspot. Geophysical Journal International, 125, 325-339.

Wu, J., Hole, J. A., Snoke, J. A. & Imhof, M. G., 2008. Depth extent of the fault-zone seismic waveguide: effects of increasing velocity with depth. Geophys. J. Int., 173, 611-622.

Wu, J., Hole, J.A. & Snoke, J. A., in preparation. Structure of San Andreas Fault zone at depth from differential dispersion of seismic guided waves.

Yoshizawa, K. & Kennett, B. L. N., 2005. Sensitivity kernels for finite-frequency surface

waves. Geophysical Journal International, 162, 910-926.

Zhou, Y., Dahlen, F. A. & Nolet, G., 2004. Three-dimensional sensitivity kernels for surface wave observables. Geophysical Journal International, 158, 142-168.

Table 3.1: Parameters for 3-D finite-difference simulations

Model Size		15000 m × 2000 m × 5000 m	
Grid Spacing		8 m	
Time Step		0.5 ms	
Source Type		explosive	
Frequency filter		high cut starting at 15 Hz	
Fault Zone Width		200 m	
Parameters 0 - 5 km depth	P-wave Velocity (km/s)	S-wave Velocity (km/s)	Density (g/cm^3)
Host rock	2.4 – 5.5	1.0 - 2.5	2.54 - 2.71
Fault Zone	1.5 - 4.0	0.65 – 1.94	1.96 - 2.13

Figure 3.1: Three-dimensional seismic velocity model and survey design.

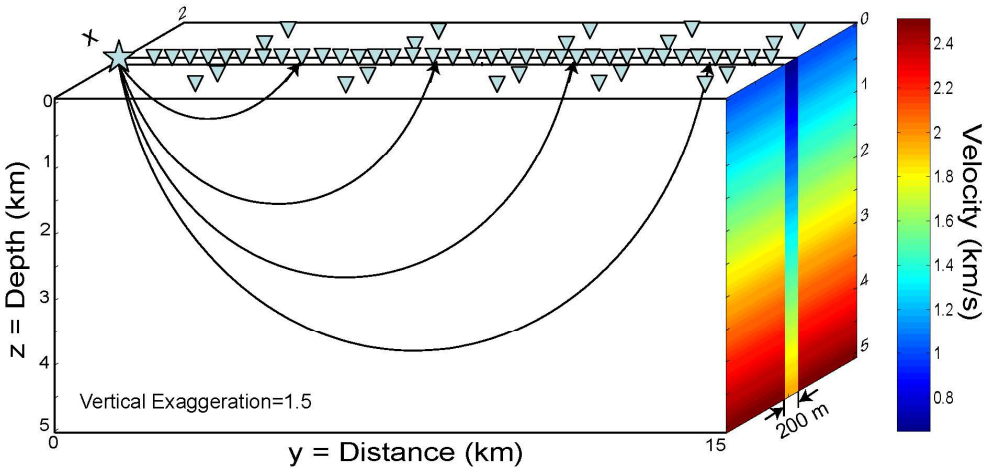

(a) 3-D FZ velocity model with source (star) and receiver arrays (triangles). S-wave velocities are shown at right and the P-wave velocity and density are proportional to the S-wave velocity; the model is homogeneous along strike. The GW ray paths shown were calculated from the 4 Hz group velocity as a function of depth (Figure 3.4b).

Figure 3.2: Three-component synthetic seismograms.

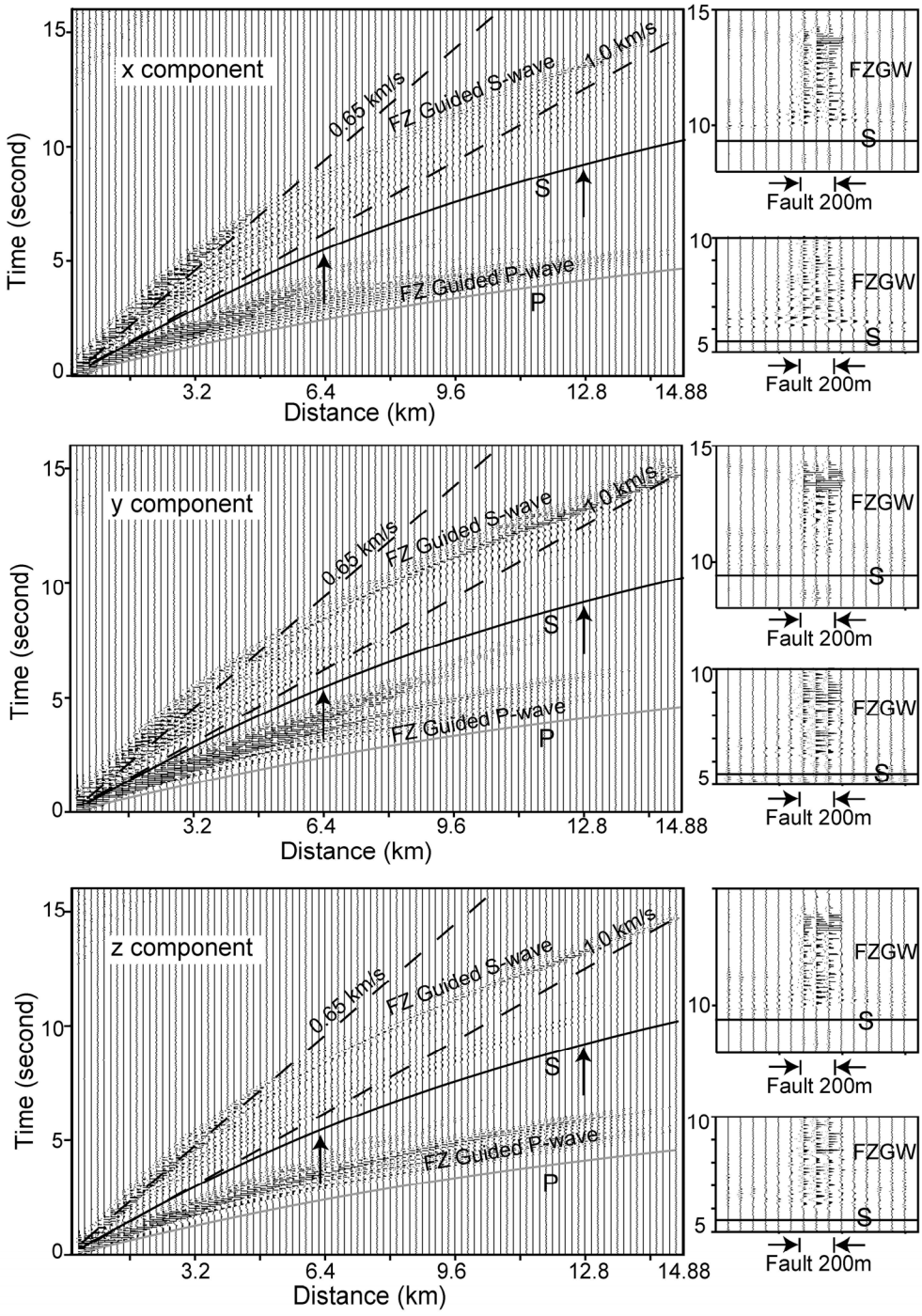

Three-component synthetic seismograms in the FZ model of Figure 3.1. At left for each component is the along-fault array within the FZ. Across-fault arrays are shown at y=6.4km (bottom right for each component) and y=12.8km (top right); arrows in the

seismic sections at left denote the locations of these arrays. Each section is separately scaled to true relative amplitude. P and S arrival times (lines) were computed in the 1-D velocity models outside the fault. Straight dashed lines indicate arrivals with velocities of 0.65 and 1.0 km/s, the S-wave velocities inside and outside the fault at the surface. FZGWs arrive later than S arrival times labeled as FZ guided S-waves. FZ guided P-waves arrive between P and S arrival times.

Figure 3.3: Pseudo-Rayleigh and Pseudo-Love FZGW particle motions for an inclined incident ray.

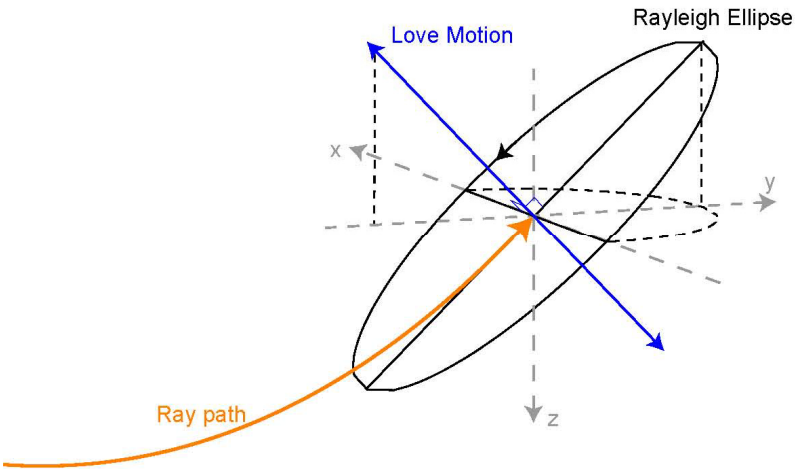

The fault and ray are parallel to the y-z plane, as in Figure 3.1. Pseudo-Rayleigh wave motion is in an ellipse with axes in the x-direction and direction that is parallel to the ray. The linear particle motion of Pseudo-Love waves is parallel to the fault and perpendicular to the ray.

Figure 3.4: Analytic group velocity dispersion and refracted travel times.

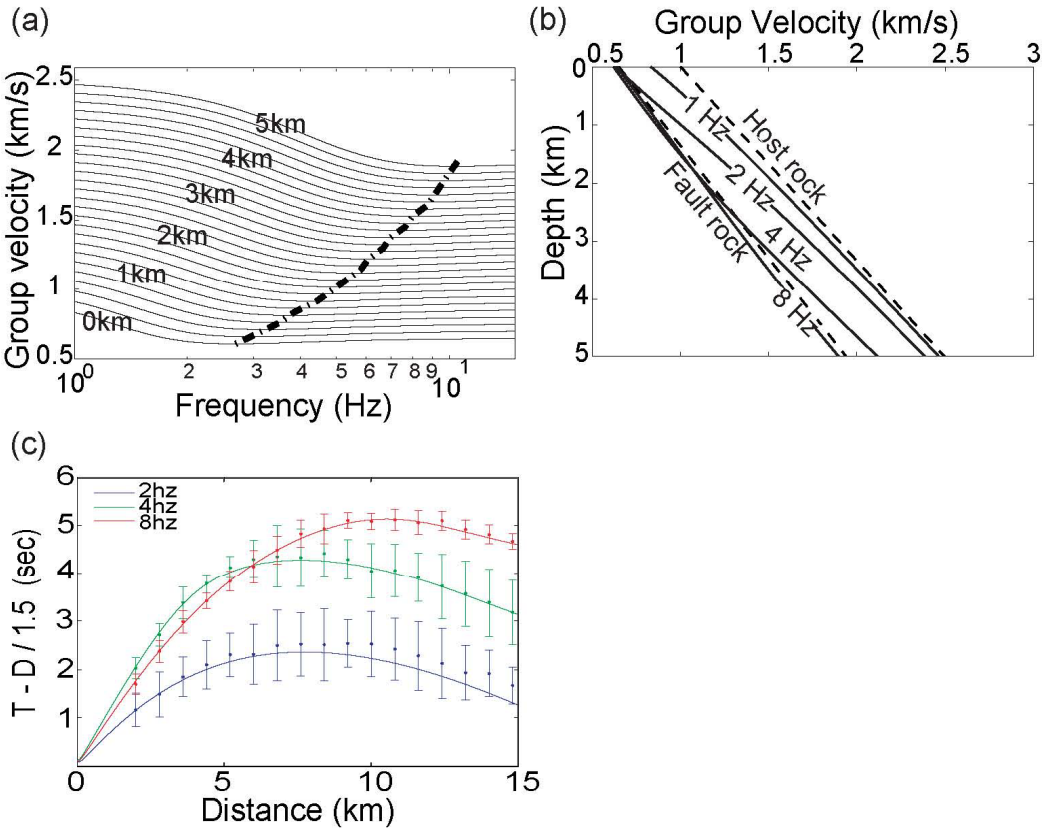

(a) Analytic pseudo-Rayleigh GW group velocity dispersion curves at different depths for the model in Figure 3.1. The dashed line connects the minimum for each dispersion curve, showing the dominant frequency increasing with depth. (b) GW group velocities at 1, 2, 4 and 8 Hz as a function of depth. Dashed lines are the S-wave velocities of the host rock and FZ. (c) Refracted travel times as a function of distance computed in the 1-D group velocity of (b) at 2, 4 and 8 Hz (lines). Travel times are reduced by a linear moveout velocity of 1.5 km/s. Dots with error bars are the observed GW travel times from the y-component along-fault synthetic seismic array (Figure 3.2). Errors were measured from the points on the envelope that are 1dB below the maximum.

Figure 3.5: GW envelopes at different frequency.

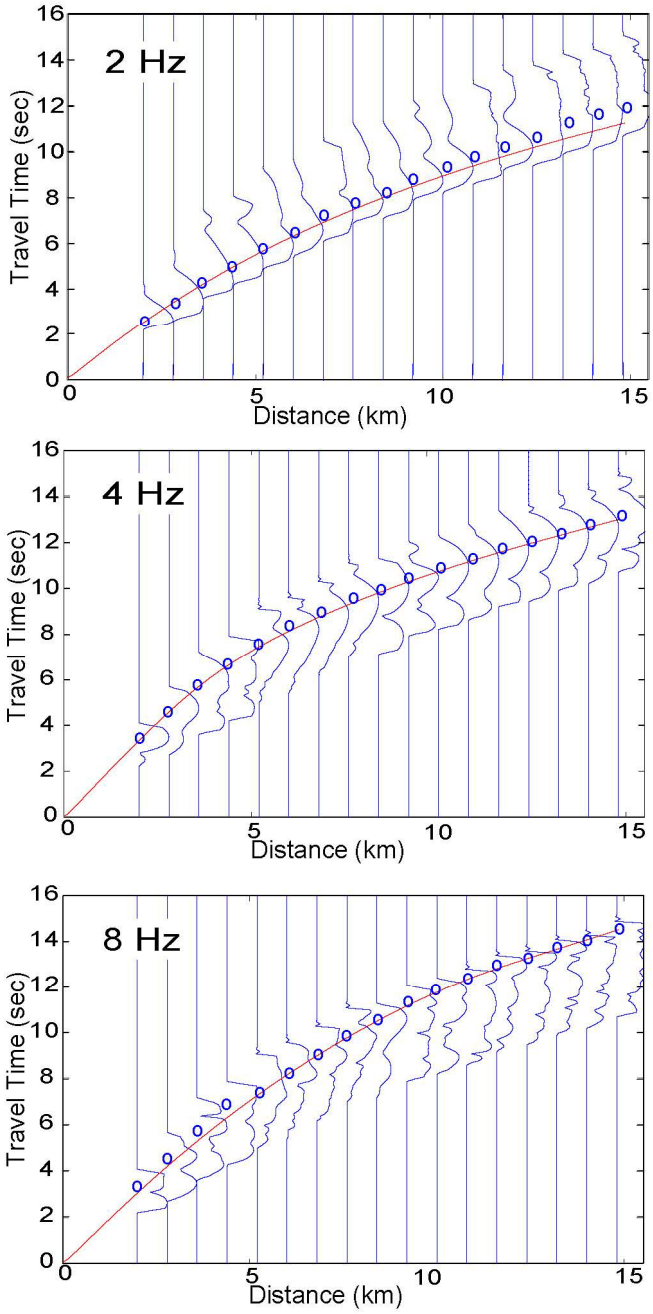

Windowed FZGW envelopes of narrow-band filtered y-component seismograms for the along-fault array (Figure 3.2). Each trace is individually scaled. Circles indicate the travel- time picks at the maximum of each envelope trace. Red solid lines are the analytic travel times from Figure 3.4c.

Figure 3.6: Analysis of synthetic seismograms.

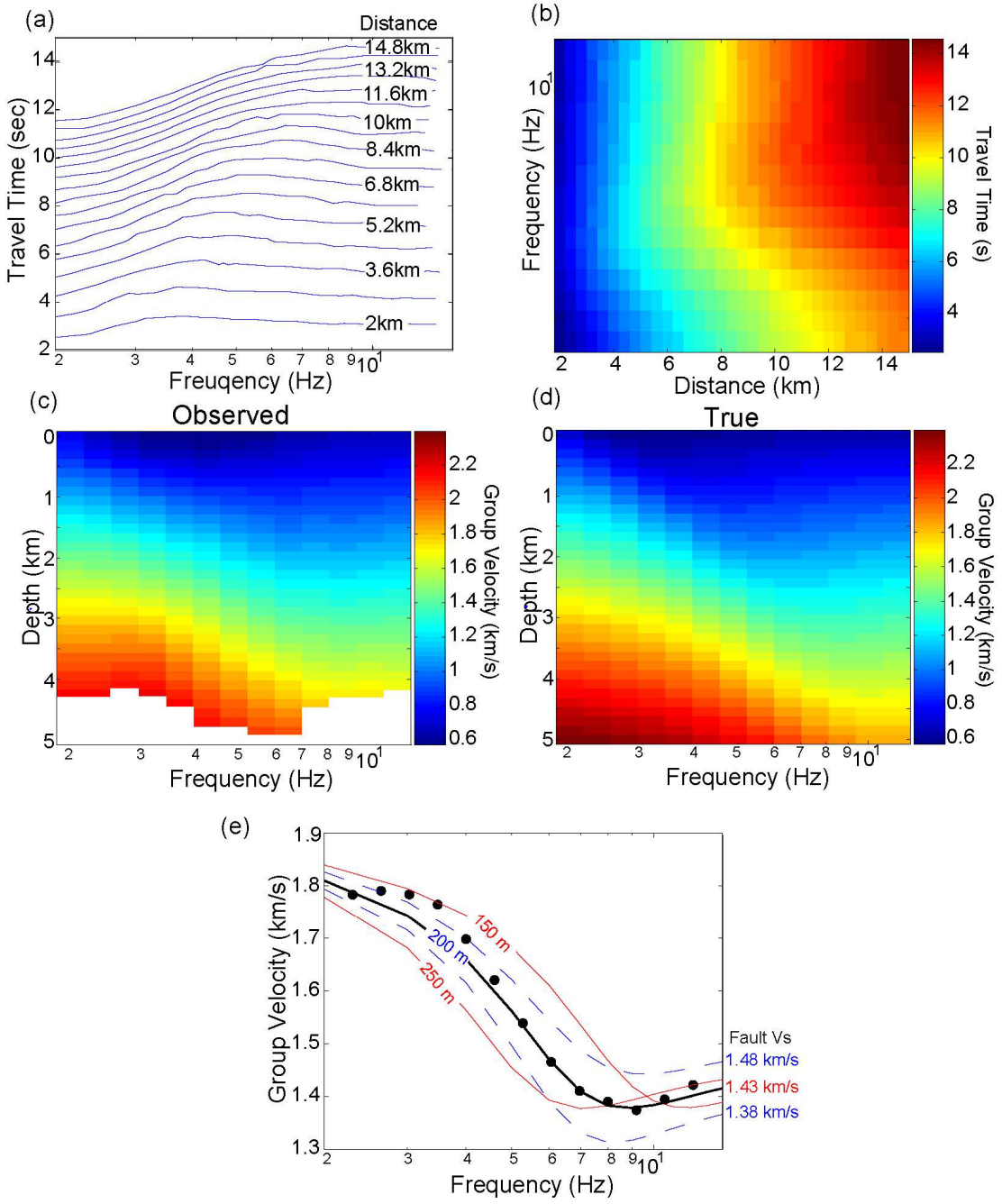

(a) Measured GW travel times versus frequency for the y-component seismograms of Figure 3.2 for seismometers at different source-receiver distances along the fault. (b) Travel times from (a) plotted versus distance and frequency. (c) Group velocity as a function of depth, derived by smoothing (b) with a 3×3-point moving averaging filter,

then 1-D inversion of the refracted travel times at each frequency. White indicates the base of ray coverage at each frequency. (d) Analytic pseudo-Rayleigh group velocity at each depth computed from the velocity model of Figure 3.1. (e) Modeling the observed group velocity dispersion curve at 3 km depth. Dots are measured group velocities from (c). The analytic dispersion curve from (d) is the black line. Blue lines are analytic dispersion curves for a 200-m wide FZ at different S-wave velocities. Red lines are analytic dispersion curves for a 1.43 km/s fault with different widths. The velocity outside the fault is assumed to be known.

Figure 3.7: Work flow for analysis of refracted guided waves.

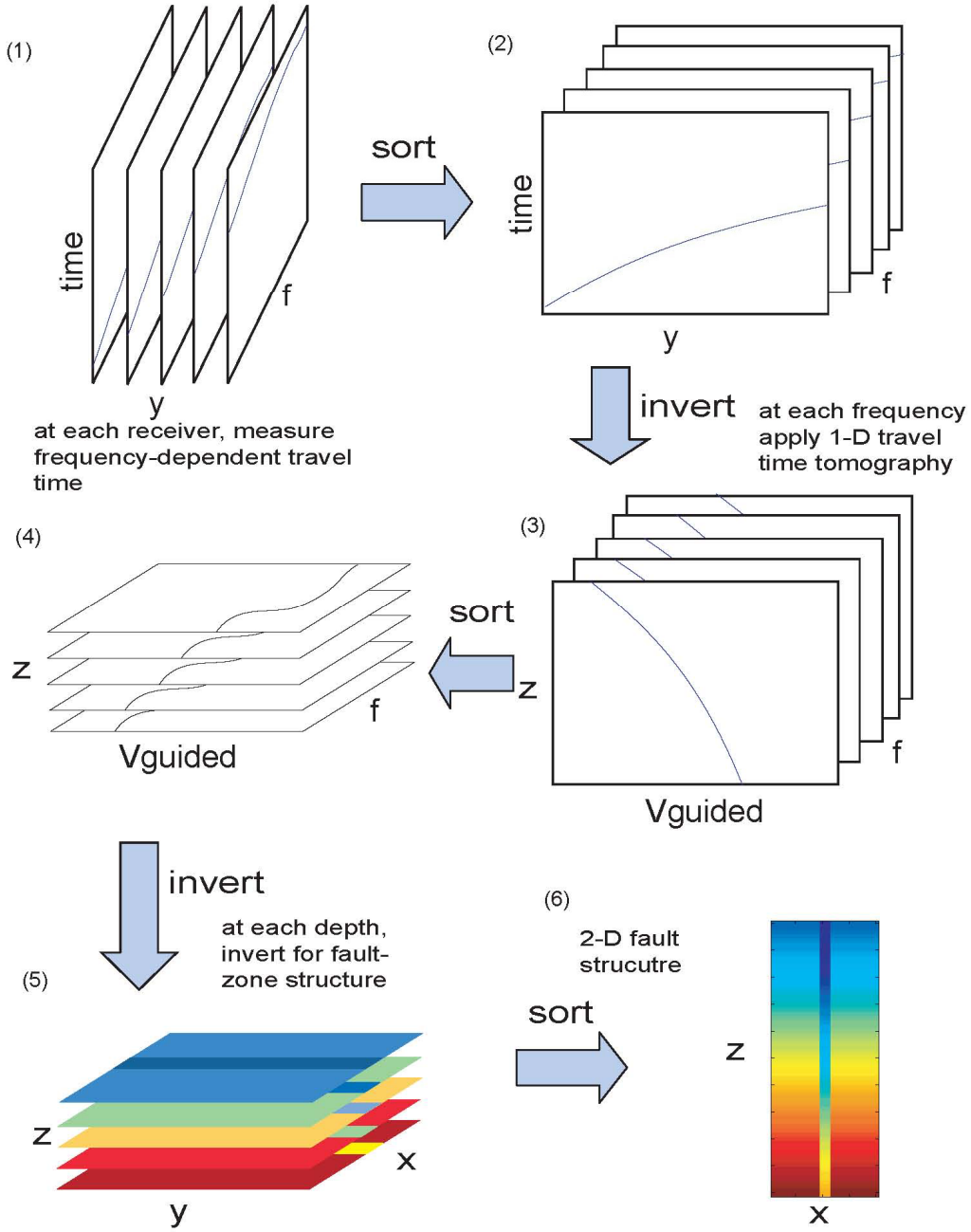

Schematic plots showing a proposed work flow for the inversion of 2-D FZ structure. Refer to the text for details.